Turbine Layout for and Optimization of Solar Chimney Power Conversion Units

by

Thomas Peter Fluri

Dissertation presented for the degree of Doctor of Mechanical Engineering at the University of Stellenbosch

Department of Mechanical and Mechatronic Engineering
University of Stellenbosch
Private Bag X1, Matieland 7602 , South Africa.

Promoter: Prof. T.W. Von Backström

2008

Declaration

I, the undersigned, hereby declare that the work contained in this dissertation is my own original work and that I have not previously in its entirety or in part submitted it at any university for a degree.

Signature: ....
T.P. Fluri

Date: ....

Abstract

Turbine Layout for and Optimization of Solar Chimney Power Conversion Units

T.P. Fluri

Department of Mechanical and Mechatronic Engineering
University of Stellenbosch
Private Bag X1, Matieland 7602 , South Africa.

Dissertation: PhDEng (Mech)
2008

The power conversion unit of a large solar chimney power plant converts the fluid power, first into mechanical power, and then into electrical power. In this dissertation a tool is developed to determine the layout and the number of turbines of the solar chimney power conversion unit providing the lowest cost of electricity.

First, the history of the solar chimney concept and the related fields of research are presented. Potential features and configurations of the power conversion unit are introduced, and it is shown how the solar chimney power conversion unit compares to those of other applications. An outline of the dissertation is given, and its potential impact is discussed.

An analytical turbine model is developed. Several modelling approaches and the performance of single rotor and counter rotating turbine layouts are compared. Preliminary turbine designs are investigated, experimentally and numerically. The main aim of the experimental investigation is to verify the applicability of the loss model used in the analytical turbine model. The aim of the numerical investigation is to evaluate a commercial software package as a tool in context with solar chimney turbines.

For each component of the power conversion unit an analytical performance model is introduced. Using these models, the single vertical axis, multiple vertical axis and multiple horizontal axis turbine configurations are compared from an efficiency and energy yield point of view, and the impact of the various losses on the overall performance is highlighted. A detailed cost model for the power conversion unit is also presented. To optimize for cost of electricity this cost model is then linked to the performance models, and the resulting optimization scheme is applied to several plant configurations.

It is shown that for a large solar chimney power plant the power conversion unit providing minimal cost of electricity consists of multiple horizontal axis turbines using a single rotor layout including inlet guide vanes.

Uittreksel

Turbine-Uitleg vir en Optimering van Sonskoorsteen-Drywingsomsettingseenhede

T.P. Fluri

Departement Meganiese en Megatroniese Ingenieurswese
Universiteit van Stellenbosch
Privaat Sak X1, Matieland 7602, Suid-Afrika

Proefskrif: PhDIng (Meg)
2008

Die drywingsomsettingseenheid van ’n groot sonskoorsteenaanleg sit die vloeidrywing om, eers in meganiese drywing en dan in elektriese drywing. In hierdie proefskrif word ’n gereedskapstuk ontwikkel om die uitleg en aantal turbines van die sonskoorsteen-drywingsomsettingseenheid te bepaal wat die laagste koste van elektrisiteit lewer.

Eerstens word die geskiedenis van die sonskoorsteen en verwante navorsingsvelde behandel. Moontlike eienskappe en konfigurasies vir die drywingsomsettingseenheid word voorgestel, en daar word aangetoon hoe die sonskoorsteen-drywingsomsettings-eenheid vergelyk met ander toepassings. ’n Raamwerk van die proefskrif word gegee, en die potensiële trefkrag daarvan word bespreek.

’n Analitiese turbine-model word ontwikkel. Verskeie nabootsingsbenaderings en die vertoning van ’n enkelrotor en teenroterende turbine-uitlegte word vergelyk. Voorlopige turbine-ontwerpe word ondersoek, eksperimenteel en numeries. Die hoofdoel van die eksperimentele ondersoek is om die toepaslikheid van die verliesmodel in die analitiese turbine-model te bevestig. Die doel van die numeriese ondersoek is om kommersiële sagteware op te weeg as ’n gereedskapstuk in die konteks van sonskoorsteenturbines.

Vir elke onderdeel van die drywingsomsettingseenheid word ’n analitiese model voorgestel. Met gebruik van hierdie modelle word die enkele vertikale-as, die veelvoudige vertikale-as an die veelvoudige horisontale-as turbinekonfigurasies vergelyk vanuit ’n benuttingsgraad- en energie-opbrengsoogpunt, en die uitwerking van die verkillende verliese op die algehele gedrag word uitgewys. ’n Kostemodel in besonderhede word vir die drywingsomsettingseenheid aangebied. Om vir die koste van elektrisiteit te optimeer word hierdie kostemodel dan gekoppel aan die vertoningsmodelle, en die gevolglike optimeringskema word toegepas op verskeie aanlegkonfigurasies.

Daar word aangetoon dat vir ’n groot sonskoorsteenaanleg die drywingsomsettingsenheid wat die minimum koste van elektrisiteit gee, bestaan uit veelvoudige horisontale-as turbines met enkelrotoruitleg en inlaatleilemme.

Acknowledgments

The present dissertation was only possible with the contribution of mainly the following people:

Professor Theo Von Backström, my mentor and promoter, gave the initial outline for this work and always had an open ear and useful advice ready. Hannes Pretorius and Cobus Van Dyk, my fellow solar chimney PhD students, and their promoters, Professors Detlev Kröger and Gideon Van Zijl, offered plenty of inspiration and insight from their areas of expertise. Hannes Pretorius also provided the plant performance data.

Andrew Gill helped setting up and operating the experimental rig. Emile Coetzer designed and manufactured the turbine used for the experimental work. Cobus Zietsman and his team in the mechanical workshop made manufacturing of parts and setting up the experiment a smooth process. Thomas Hildebrandt of NUMECA supplied a free license and gave excellent support for their software package. Volker Wittwer of the Fraunhofer-Institute for Solar Energy Systems provided valuable information on glass used in solar engineering. Danie Els gave expert LaTeX support and helped with the layout of this document. Marco Bernardes proof read the dissertation and gave useful feedback.

Nicola Cencelli, Keegan Thomas, Giovanni Milandri, Carl Kirstein, Sandisiwe Mvimbi and Andrew Gill (in order of appearance) made the office I shared with them a friendly and motivating work environment. My friends in South Africa, of whom some have already been mentioned, made Stellenbosch a home away from home; my friends and family in Switzerland and in other parts of the world never tired of giving moral support.

The work presented in this dissertation was funded by the German Volkswagen-Stiftung and the South African National Research Foundation.

Thank you.

Contents

List of Tables

List of Figures

Nomenclature

Latin Symbols

A	area
b	surface area specific chimney cost
b_x	blade-row axial chord
c	nondimensional absolute flow velocity
c_h	blade chord
c_p	specific heat at constant pressure
C	absolute fluid velocity, cost
C_L	lift coefficient
C_p	static pressure recovery coefficient
d	diameter
d_x	stator-rotor axial gap
g	gravitational acceleration, growth
h	enthalpy per unit mass flow, height
H	height
i	interest rate
k	thermal conductivity
l	length
$\dot{m}$	mass flow rate
M	Mach number
N	number of years
o	opening or throat width
p	pressure
P	power; present value of total cost
Pr	Prandtl number
q	heat per unit mass transferred
Q	heat transferred; volume flow rate
$\dot{Q}$	rate of heat transfer
r	radius
R	specific gas constant
R_{asp}	blade aspect ratio
R_d	diffuser area ratio
Re	Reynolds number
R_{HT}	hub to tip radius ratio
R_n	degree of reaction
T	temperature

T_q	torque
u	dimensionless peripheral blade speed
U	peripheral blade speed
u_b	dimensionless blade speed of the second rotor
w	dimensionless relative fluid velocity
W	relative fluid velocity
Z	number of blades
Z_t	number of turbines

Greek Symbols

α	absolute flow angle
β	rotor relative flow angle
γ	ratio of specific heats
δ	absolute error
Δ	difference
ϵ	flow deflection
ζ	loss coefficient
η	efficiency
θ	blade camber angle
ρ	density
σ	solidity
Φ	flow coefficient
Ψ	load coefficient
ω	rotational speed

Subscripts

a	first rotor row
b	blade, second rotor row
BM	bell mouth
c	chimney, construction
col	collector
d	diffuser
DT	drive train
ex	exit
h	hydraulic
hv	horizontal vertical transition
in	inlet
id	ideal
m	mixing
opt	optimum
p	probe
r	rotor
rel	relative

s	static
t	turbine, total
u	circumferential direction
x	axial
0	upstream of inlet guide vanes
1	upstream of first rotor
2	downstream of first rotor
3	downstream of second rotor
4	downstream of diffuser

Abbreviations

AGS	Abu-Ghannam and Shaw
AR	anti reflective
BOS	balance of station
CC	capital cost
CFD	computational fluid dynamics
CR	counter rotating
DDPM	direct drive permanent magnet generator
DG	double glazing
EAC	equivalent annual cost
F.S.O.	full scale output
HAT	horizontal axis turbine
IGBT	insulated gate bipolar transformer
IGV	inlet guide vane
OC	operating and maintenance cost
O&M	operating and maintenance
PCC	present value of capital cost
PCU	power conversion unit
POC	present value of operating cost
PS	pressure side
ref	reference
rpm	rotations per minute
SA	Spalart-Allmaras
SCPCU	solar chimney power conversion unit
SCPP	solar chimney power plant
SS	suction side
SST	shear stress transport
SR	single rotor
VAT	vertical axis turbine

Chapter 1

Introduction

This is one of three PhD dissertations resulting from a research collaboration on the solar chimney power plant concept between the University of Stellenbosch and the Bergische Universität Wuppertal, Germany. Plant optimization and control and the solar chimney technology development process are the focal points of the two concurrent dissertations[1]. The present study investigates solar chimney turbine layouts and power conversion unit optimization.

In this chapter a brief introduction to the solar chimney power plant concept is given; its history as well as the fields of research associated with the concept are presented. Further, a comparison to other power schemes is provided. Then, various possible layouts for the power conversion unit are introduced. It is shown how the power conversion unit of a solar chimney power plant compares to those of other applications like wind turbines or gas turbines. A reference plant is defined. Cost and performance data for this specific plant is presented. Finally, a dissertation outline is given, the remaining chapters are summarized and the potential impact of the dissertation is discussed.

1.1 The Solar Chimney Power Plant (SCPP)

The main features of a solar chimney power plant are a solar collector and a tall chimney (Fig. 1.1). The collector consists of a circular transparent roof and the ground under the collector floor surface. Solar radiation heats the ground, which in turn heats the air under the collector roof like in a greenhouse. The hot air rises and escapes through the chimney. The resulting airflow is used to generate electricity via one or several turbogenerators.

---

[1] (Pretorius, 2006; Van Dyk, 2008)

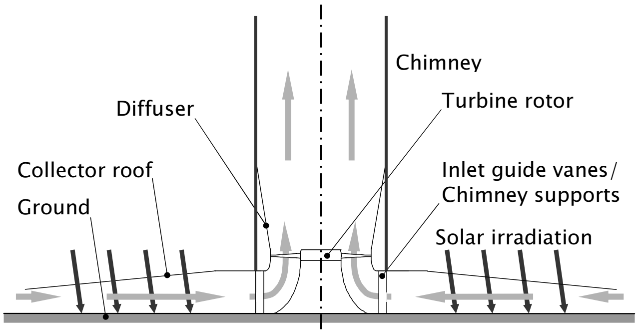

Figure 1.1 Schematic drawing of a solar chimney power plant with a single vertical axis turbine.

1.1.1 A Solar Chimney Timeline

1500 As with so many other inventions, it was Leonardo da Vinci (1452-1519) who created the earliest system, which uses hot air rising in a chimney to drive an apparatus; one of his sketches depicts a roasting spit driven by a turbine located in the chimney above a fireplace (Calder, 1970).

1903 Isidoro Cabanyes, a Spanish colonel, was the first to propose to use a solar chimney to generate electricity (Cabanyes, 1903).

1956 A similar concept to that of the modern solar chimney power plant can be found in a patent of Ridley (1956). The inventor suggests to create a large vortex by adding swirl to the air flow in the collector and injecting a stream of cold air in the center of the chimney. It is hoped that, with the help of coriolis forces, the created vortex can be sustained even far beyond the chimney exhaust and that this will lead to a good system performance without the necessity of a very tall chimney.

1980-1989 The major player in recent SCPP development, the German structural engineering company Schlaich Bergermann and Partners (SBP), designed, built and tested a solar chimney pilot plant in Manzanares, Spain. With its 195 m tall chimney and a 240 m diameter collector this is the largest SCPP to date. After an experimental phase it fed the Spanish grid in fully automated operation from July 1986 to February 1989 during a total of 8611 hours (Schlaich, 1995). Even though the nominal power output of an economically viable plant is three to four orders of magnitude higher, the results from Manzanares show that this concept is a possible alternative to conventional power plants and warrant further investigation.

Today there are plans for large-scale SCPPs in Australia[2], Southern Africa[3], Bra-

---

[2] www.enviromission.co.au

[3] www.greentower.net

zil[4] and many other places in the sunny areas of our planet. None however have yet been built.

1.1.2 Main Fields of Research

The main fields of research in context with solar chimney power plants are the chimney structure, collector performance, the power conversion unit and system performance. They are discussed here. Other fields of research are briefly mentioned in the following section.

Chimney Structure: According to Schlaich (1995) the chimney of an economically viable SCPP is 950 m high and has a diameter of 115 m. The tallest free-standing structure on land to date is the CN Tower in Toronto and is 553 m high[5]. This makes it clear that the chimney structure alone is an engineering challenge. Schlaich (1995) discusses several ways of building the chimney and proposes to use a steel reinforced concrete tube for large-scale plants. For the pilot plant in Manzanares a guyed sheet metal tube was used.

Goldack (2004) introduces several wind load cases and investigates the influence of different stiffeners and wall thickness distributions on the structural behavior of large solar chimneys of 1000 m height. He points out that more work is necessary to establish the appropriate wind load cases and to evaluate the influence of the temperature variation on cracking, and he suggests to do empirical studies, e.g. on large cooling towers, to assess the influence of geometrical imperfections on local loads.

A preliminary study on the support struts of a 1500 m high solar chimney is presented by Van Dyk (2004*a*). Rousseau (2005) looks at wind loads on a chimney of the same height located in the Northern Cape province of South Africa. He proposes a revision of the static wind load profile and predicts that resonance will occur at yearly recurring gusting speeds. Alberti (2006) investigates the stabilizing effect of vertical ribs on a solar chimney structure. For the present dissertation it is assumed that chimneys of up to 1500 m height are feasible.

Collector Performance: Significant research effort has been put into mathematically modelling the collector performance. An analytical model has been presented by Schlaich (1995). Early numerical models have been presented by Kröger and Buys (1999), Gannon and Von Backström (2000), Hedderwick (2001) and Beyers *et al.* (2002).

More recent numerical models are available from Bernardes (2004) and Pretorius and Kröger (2006a). According to Bernardes (2004) the collector

---

[4] (Bernardes, 2004)

[5] see http://en.wikipedia.org/wiki/List_of_tallest_buildings_and_structures_in_the_world

accounts for more than 50 % of the investment cost and about 50 % of the overall system losses. Improving its performance offers a big potential to make the SCPP cost competitive. Pretorius and Kröger (2006a) investigate a variety of glass qualities and various types of soil and the impact of using a convective heat transfer equation, which was recently developed by Kröger and Burger (2004).

Bonnelle (2003) suggests to use a collector with a nervelike structure, leading to a partial separation of the main functions of the collector, which are (1) collecting heat and (2) transporting hot air to the tower. But, it is still to be proven if such a departure from the standard configuration with a simple glass roof would really improve the collector performance.

Power Conversion Unit (PCU): The power conversion unit of a large solar chimney power plant is the part in which the fluid power gets converted, first into mechanical power and then into electrical power, ready to be fed into a larger regional or national grid. It consists of one or several turbogenerators, power electronics, a grid interface and the flow passage from collector exit to chimney inlet. The PCU with its turbogenerators is the main topic of this dissertation and will be discussed in detail in Section 1.2 (pp. 8). A general literature review on the solar chimney power conversion unit and on solar chimney turbines will be given there and in the Chapters 2 and 5.

System Performance: In order to predict SCPP performance various mathematical models have been developed since the early 1980s. As much as they may vary concerning modelling approach and computational implementation, they share some important trends: With all models the power output increases with the size of the chimney and the collector area, and they all show a large daily and seasonal fluctuation in power output. Unfortunately, the amount of experimental data available for validation of these models is very limited, and in most cases data from the Manzanares plant have been used. Haaf *et al.* (1983) present a simple model, which they used for the design of the pilot plant in Manzanares. Pasumarthi and Sherif (1998a) show a more detailed model, which they verify against their own experimental results and results of the Manzanares pilot plant (Pasumarthi and Sherif, 1998b). Gannon and Von Backström (2000) adapt the standard gas turbine cycle to define a standard solar chimney cycle. They also compare the results from that simple model to experimental results of the Manzanares plant.

A recent comprehensive model has been developed by Bernardes (2004). He investigates the possibility of using waterfilled bags on the collector floor as heat storage device and finds that its implementation smoothes out the daily fluctuation in power output and, hence, strongly increases the power output after sunset. But, as can be expected, the peak power output is reduced. The overall energy gain is not significantly affected. Further, Bernardes (2004) does not recommend the use of double glazing for the collector roof, as his model predicts an increase in annual power output of only 5.6 %. He also finds that the impact of changes in humidity of the air and properties of the collector ground is small.

Pastohr *et al.* (2003) model the Manzanares plant using a commercial computational fluid dynamics (CFD) software package. They also derive an analytical model for the collector and compare it to the CFD results. Using simple analytical models Von Backström and Fluri (2006) point out the importance of finding the turbine pressure drop for maximum power output.

The most comprehensive SCPP performance model is presented by Pretorius and Kröger (2006b). It is based on the model of Hedderwick (2001). As mentioned earlier, various types of soil for the collector ground and a variety of glass qualities for the collector roof can be simulated (Pretorius and Kröger, 2006a). For the dissertation of Pretorius (2006) the model has been modified to allow for ambient wind, various temperature lapse rates, nocturnal temperature inversions and the use of the collector as a greenhouse. The impact of these parameters on the performance of the plant has been investigated. Modifications to enable peak or base load operation of the plant are also proposed and implemented in the model. In contrast to Bernardes (2004), Pretorius (2006) finds that the properties of the collector ground have a significant impact on the daily power distribution, and that the use of double glazing for the collector roof increases the annual power output by at least 32.3 %. Pretorius *et al.* (2004) present an earlier version of their model and find that the SCPP performance deteriorates with the presence of ambient winds but is not significantly affected by the shadow of the chimney.

1.1.3 Other Fields of Research

Cost Modelling: The fact that no large scale SCPP has been built yet, makes cost modeling in particular, difficult, as it is difficult to get realistic quotes for materials and components. According to Bernardes (2004) an early approximate cost model was presented by Haaf *et al.* (1986). More comprehensive models have been presented by Schlaich *et al.* (1995), Bernardes (2004) and Fluri *et al.* (2006).

Fluri *et al.* (2006) report an approximately 2 1/2 times higher initial cost for the collector and the chimney than Bernardes (2004). However, according to Weinrebe (2006), the material cost assumed in the paper of Fluri *et al.* (2006) is much too high. In the remainder of this dissertation the initial cost for the chimney and the collector are therefore evaluated according to the model of Bernardes (2004), and the higher values presented by Fluri *et al.* (2006) are merely regarded as a cautionary note. When using older cost data, inflation and other cost fluctuations have not been taken into account in the present dissertation.

Fluri *et al.* (2006) also present a detailed cost model for the PCU and find the initial PCU cost to be much lower than predicted by Bernardes (2004). This model is the basis of the cost model, which will be presented in Chapter 6. Pretorius (2006) also presents a simple cost model for the SCPP; it will be discussed in more detail in Chapter 7.

Interaction with the Atmosphere: What the flow field around and above this huge structure will look like is difficult to predict. This prediction and the interaction with the atmosphere have not been thoroughly investigated. Thiart (2002) shows the results of a first attempt to model the flow in and around a solar chimney with a commercial CFD package. Harris (2004) presents an attempt to model the air flow above the collector numerically. Pastohr (2004) shows an unsteady axisymmetric solution of the flow field in and around a very small solar chimney (chimney diameter = 0.05 m) using a commercial CFD package. None of the mentioned studies is able to provide a realistic representation of the interaction between the solar chimney power plant and the surrounding atmosphere. But understanding this interaction is important to make accurate performance predictions. Hence, this research area needs more attention.

Ecology: Life cycle assessments of solar chimney power plants are available in the literature, where their macro-ecological impact is shown (Bernardes, 2004). The micro-ecological impact of a large-scale SCPP on a site in the Northern Cape of South Africa has also been assessed and no significant negative environmental impact has been detected (Van Dyk, 2004*b*).

Agriculture: The idea of using the cooler parts of the collector as a greenhouse is interesting and has a large potential for increasing the return on investment of the complete system. Pretorius (2006) shows, however, that using the outer part of the collector as a greenhouse significantly reduces the electrical power output of the plant[6]. Another problem with placing a huge greenhouse in a dry area is its potentially immense water consumption. Westdyk (2007) presents an experimental study on grass growing under a solar chimney roof and measures the rate of evapotranspiration. Pretorius (2006) uses her data and finds that up to 4000 kg/s of water would have to be supplied to the greenhouse to keep it from drying up, i.e. the crop needs to be selected carefully, and a system to recirculate the water should be developed.

Socio-Economics: Solar chimney power plants are highly suited for developing countries and have a big potential for local manufacture and poverty alle-

---

[6] Pretorius (2006) uses rather large portions of the collector as a greenhouse (36 and 64 % of the area) and the power output is reduced by 30 to 45 %.

viation. Friedel (2005) presents a socio-economic study on the SCPP in a South African context.

Material Science: There are various potential areas for research in material science in context with solar chimney power plants, e.g. developing a low-cost collector roof cover material with high transmissivity or a building material with low density but high stiffness for the chimney structure.

Alterations to the basic concept: Several ideas for alterations on the basic concept of the solar chimney power plant can be found in the literature; e.g. Bilgen and Rheault (2005) suggest to build the collector on a sloped surface at high latitudes.

Technology Development: As the dimensions of a large-scale SCPP are clearly beyond the limits of common practice, a technology development methodology is introduced by Van Dyk (2006).

1.1.4 Comparison to Other Power Schemes

Trieb *et al.* (1997) compare performance, cost and environmental impact of the six most developed solar power technologies, which are parabolic troughs, central receiver, dish-Stirling, solar chimney, solar pond and photovoltaic cells. As reference system for the solar chimney power plant a 30 MW plant defined by Schlaich (1995) is used. For the parabolic trough concept, which is the most mature concept for solar thermal power generation, a 80 MW hybrid plant with a solar share of 49.4 % is chosen. Compared to the SCPP its power-specific land use is about 8 times lower, it has a 36.5 % lower specific investment cost (5421 DM/kW) and generates electricity at a 30.7 % lower cost (0.205 DM/kWh).

These numbers could tempt to conclude that the solar trough concept should be favored over the solar chimney concept. But one has to keep in mind that solar troughs have been tested extensively and have produced many giga-Watt hours of electricity, whereas solar chimney power plant technology is still in its very childhood, and because of various features, e.g. its built-in energy storage capacity, its capability of using diffuse radiation and the fact that it does not need cooling water, it has the potential to become a competitive alternative. Also, a 30 MW solar chimney is a rather small plant, and effects of scale are very important with this concept. Moreover, comparing a hybrid plant to a purely solar one is problematic; the fuel cost may have a strong influence on the result and should at least be given when mentioning hybrid power plant cost of electricity.

More recently, Mills (2004) reviews various advanced solar thermal electricity technologies, e.g. solar trough and linear fresnel. He quotes a study, which takes a US$25 per tonne carbon credit into account and predicts a very low cost of electricity of between US$0.032 and $0.043/kWh for the solar trough technology.

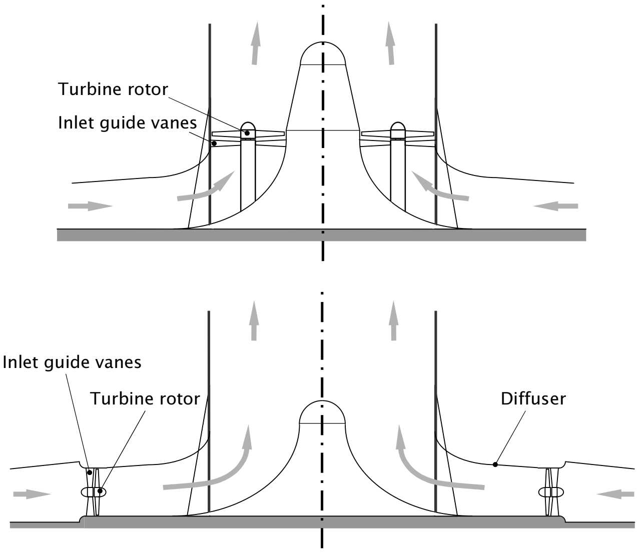

Figure 1.2 Schematic drawing of a solar chimney power plant with six vertical axis turbines (2 represented, top) and 32 horizontal axis turbines (2 represented, bottom).

1.2 The Solar Chimney Power Conversion Unit (SCPCU)

In 1884 Sir Charles Algernon Parsons patents the steam turbine and introduces the turbogenerator in the engineering world (Wilson and Korakianitis, 1998). Today, this kind of energy-conversion device, a turbine connected to an electric generator, is found in almost all large-scale power plants (> 30 MW), no matter whether their primary energy source is coal, oil, gas, water, nuclear, or one of the new renewables. Adapting to the wide variety in requirements in those various applications the power conversion unit and its components have assumed all kinds of shapes and sizes. How the solar chimney power conversion unit, as defined on page 4, fits into this big family is discussed in Section 1.2.2. Before that, the various features and configurations of a SCPCU, which have been proposed in the literature, are introduced.

1.2.1 Various Features and Configurations of SCPCUs

Besides the solution shown in Figure 1.1 (p. 2), where a single vertical axis turbine is used, PCU configurations with multiple vertical axis turbines or multiple horizontal axis turbines (Fig. 1.2) have also been proposed (e.g. by Schlaich (1995)). Their main characteristics are presented here.

- *Vertical vs. horizontal shaft*: In a vertical shaft configuration the turbines are integrated in the chimney. In a horizontal shaft configuration the turbines are located around the chimney circumference with their axes perpendicular to the chimney axis. A vertical shaft configuration reduces cyclical stress on the components due to gravity but requires a thrust bearing to carry the weight of the whole rotor. For a horizontal shaft configuration the pressure after the turbine section is sub-atmospheric, which makes sealing of the horizontal to vertical flow transition section necessary.

- *Single vs. multiple turbines*: A single turbine with a vertical shaft was used for the Manzanares plant. The design of the PCU was made by Schwarz and Knauss (1981). Gannon (2002) also analyzed such a configuration but for a large-scale SCPP. Its advantages are (1) the simplicity of the flow passage and (2) the small number of parts. Its disadvantages are (1) huge torque, which, in the case of a large-scale SCPP, necessitates a huge generator (2) huge size, which makes manufacturing, handling and transport difficult and (3) lack of redundance.

- *Inlet guide vanes (IGVs)*: In the Manzanares plant the turbine pressure drop was small and it was not deemed necessary to reduce the exit swirl, e.g. by means of inlet guide vanes (Schwarz and Knauss, 1981)[7]. In the case of a large-scale SCPP the impact of the exit swirl is much bigger. If the pitch of the IGVs is variable, they can also serve to control the plant output and to close off the turbine flow passage(s) for emergency or maintenance. Inlet guide vanes will be discussed in more detail later.

- *Counter rotating turbines*: Another way of reducing the exit swirl of a turbine is to introduce a second blade row, which rotates in the opposite direction. This approach was used for the low speed low pressure turbine in the experimental aircraft engine General Electric GE36[8]. In commercial wind turbines counter rotating rotors have not been implemented, because the theoretical maximum power coefficient of two counter rotating rotors is only little higher than that of a single rotor (Spera *et al.*, 1994). Nonetheless, several companies are currently developing wind turbines with counter rotating rotors with the aim of reducing the cost of electricity[9]. Counter rotating turbines have also been proposed for the SCPP (Denantes and Bilgen, 2006). This turbine layout will be discussed in more detail in Chapter 2.

- *Diffuser after the turbine*: To reduce the exit kinetic energy losses while keeping the size of the turbine small, an exhaust diffuser has been proposed by various authors, e.g. by Gannon (2002). In a configuration with multiple horizontal axis turbines a diffuser could be placed directly after the turbines or in the chimney. A diffuser model will be introduced in Chapter 5.

---

[7] Schwarz and Knauss (1981) estimated a potential increase in power output of 2.5 kW; the expected power output at design point was 100 kW.

[8] http://en.wikipedia.org/wiki/General_Electric_GE36

[9] See for example www.kowintec.com or http://eotheme.com (August 2007).

1.2.2 Comparison to other Applications

Wind Turbines

The specifications for a power conversion unit for solar chimney power plants are in many aspects similar to the ones for large wind turbines (Gannon, 2002). The task of both, the large wind turbines and the SCPCU, is to convert large amounts of energy in the air flow to electrical energy and feed this into a grid. But there are various important differences. The following characteristics are typical for wind turbines but not for solar chimney turbines:
Wind turbines

- are unducted or free turbines. This reduces the maximum power, which may be extracted from the fluid, to 59.3 % of the power available in the fluid[10].
- They have to direct themselves into the oncoming wind,[11]
- can only produce electricity when the speed of the oncoming wind is within certain limits,
- are exposed to weather,
- have to be designed to withstand gusts and
- are visible from far.

In solar chimney power plants, however,

- the turbines are ducted, and their maximum theoretically achievable total-to-total efficiency is therefore 100 %, and tip losses are comparably small[12],
- the direction of the oncoming air flow is known and remains constant,
- the turbines are protected from harsh weather conditions but have to cope with higher temperatures,
- the large volumes of collector and chimney act as a buffer preventing large fluctuations in air flow speed, i.e. dynamic loads on the turbine blades and all the other rotating components are comparably low,
- the visual impact of the power conversion unit is small compared to that of the chimney and the collector and

---

[10] This fact is called the Betz limit (Burton *et al.*, 2001)

[11] This is only true for horizontal axis wind turbines, but vertical axis wind turbines have almost no importance in today's market and are disregarded here.

[12] The aforementioned Betz limit is not applicable to ducted turbines. Unfortunately it has been implemented into various codes written for the SCPP (see e.g. Pastohr *et al.* (2003))

- the power output is mainly dependent on solar irradiation, which is much more predictable than wind, improving the power quality.

Furthermore, the turbine pressure drop in SCPPs is about 10 times bigger than with wind turbines (Gannon, 2002).

Many of the recent advances in wind turbine technology will potentially be adapted to solar chimney technology and will have an impact on the design and the cost of the solar chimney power conversion unit. As an example, many modern wind turbines use a direct drive variable speed generator (Bywaters *et al.*, 2004). In most of the solar chimney literature it is assumed that a constant speed drive train would be used. A change to a variable speed drive train holds the potential for improved off-design performance and will be discussed further (e.g. on page 14).

Gas Turbines

Gas turbines on the other hand are smaller in diameter than solar chimney turbines, have much higher stage loads and are designed for higher blade speeds. Thermal stresses are much more important in gas turbine design as well. They also have a higher blade count and a higher solidity (Gannon, 2002).

1.3 Dissertation Outline

Results from pilot plant testing in Manzanares and from various mathematical models found in the literature make large-scale solar chimney power plants a promising option for sustainable power generation. Integrated design of the various components and optimization of overall system performance are however necessary.

Various layouts have been proposed for the power conversion unit of this power plant concept, but no method is available to make an informed decision on which layout to choose. The main thesis of this dissertation is therefore the following:

> *"For a large solar chimney power plant the power conversion unit providing minimal cost of electricity consists of multiple horizontal axis turbines using a single rotor layout including inlet guide vanes."*

The goal of the present work is to test this hypothesis and to develop a tool, with which one can quickly find the optimal power conversion unit for a certain plant configuration and with which the impact of the various design parameters can be assessed. While the focus of this dissertation rests on the fluid mechanics side of solar chimney turbomachinery, other aspects, for example control, electrical aspects, structure and cost are to be included.

The following questions are underlying to the present dissertation and are investigated: What are feasible layouts for power conversion units to be used in large solar chimney power plants? What are the adequate criteria to judge their quality? Which layout is the best? What is the optimum number of turbines? Are the standard gas turbine loss correlations and design guidelines applicable to solar chimney turbines? Are the losses due to the mixing of the various turbine exhausts critical? Should there be a nozzle or a diffuser behind the turbines?

1.3.1 Method

The structure of the tool to be developed to optimize the solar chimney power conversion unit is summarized in the flow chart in Figure 1.3. The plant performance data and the cost of collector and chimney are taken from models presented in the literature. A performance model and a cost model for the power conversion unit and a procedure to evaluate the cost of electricity are introduced in this dissertation. They are linked to each other to find the optimal power conversion unit for a given solar chimney power plant configuration. This work is divided into the remaining chapters as follows:

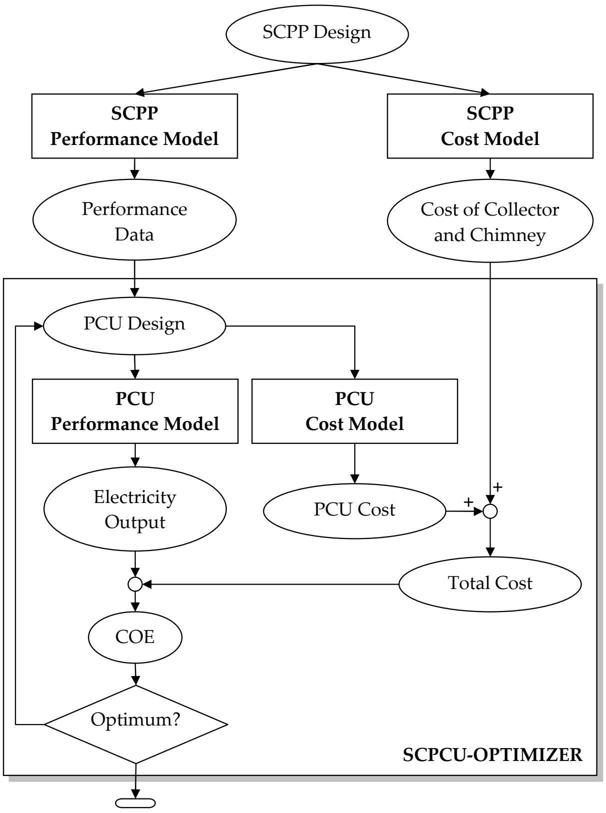

Figure 1.3 Flow chart summarizing the structure of the solar chimney power conversion unit optimization tool developed in this dissertation.

Chapter 2: An analytical model for solar chimney turbines is presented. The performance of several layouts is compared, and the important design parameters are discussed. The turbine layouts under consideration are single rotor and counter rotating turbines, both with and without inlet guide vanes.

Chapters 3 and 4: The solar chimney turbine designs developed at the University of Stellenbosch for the single vertical axis turbine configuration and the multiple horizontal axis turbine configuration are investigated experimentally and with a commercial CFD package. The main aim of this investigation is to assess the applicability of simple loss correlations used in the design of steam and gas turbines to solar chimney turbines.

Chapter 5: The turbine model presented in Chapter 2 is integrated into a performance model for the whole solar chimney power conversion unit. With this model a comparison of three configurations from an efficiency and energy yield point of view is made, and the impact of the various losses on the overall performance is highlighted. The three configurations are the single vertical axis, the multiple vertical axis and the multiple horizontal axis turbine configuration. The potential use of diffusers at the turbine exit is also discussed.

Chapter 6: To minimize the cost of electricity a detailed cost model for the PCU is introduced in this chapter, and it is linked to the performance models presented in the earlier chapters. Optimal solutions are presented for the various layouts and configurations of the PCU.

Chapter 7: The developed tool to optimize the power conversion unit of solar chimney power plants is applied to several plant configurations.

Chapter 8: Finally, the conclusions of this dissertation are drawn and an outlook on future research is given.

1.4 Potential Impact of this Dissertation

In order to give the numbers stated in the coming chapters more meaning and the reader an idea of how big an impact of the dissertation results may be expected, a pre-assessment is presented in this section. The reference plant used here is defined as in the work of Pretorius and Kröger (2005). The main features of the plant are summarized in Table 1.1.

In the following sections performance data for such a plant are presented, simple cost models and an evaluation procedure for cost of electricity are introduced, and by varying certain key-parameters their potential impact is shown.

1.4.1 Plant Performance Data and Yield Evaluation

The performance data used in this work has been generated with a numerical model described by Pretorius and Kröger (2006b), which is a revised version of the one described in their earlier publications and includes novel convective heat transfer and momentum equations. In Figure 1.4 the turbine pressure ratio, p_{tI}/p_{tII}, extracted from the simulation results, representing operation over a period of one year, is plotted against the inlet mass flow coefficient or "swallowing capacity" $\dot{m}\sqrt{T_{tI}}/p_{tI}$. The resulting curve can be fitted well using the ellipse law introduced by Stodola (1945), which according to Dixon (1998) reads

$$\dot{m}\frac{\sqrt{T_{tI}}}{p_{tI}} = k\left[1-\left(\frac{p_{tII}}{p_{tI}}\right)^2\right]^{1/2} \tag{1.1}$$

where T_{tI} is the total temperature at the turbine inlet, p_{tI} and p_{tII} are the total pressures at inlet and outlet and k is a constant. The ellipse law has been used for many years to model the off-design behavior of multistage steam turbines. Dixon (1998) gives a derivation of that law employing the assumption that the blade speed is changed in direct proportion to the axial velocity. Adjusting the blade speed in such a manner ensures that the velocity triangles remain similar and so does the turbine efficiency. Hence, the fact that the operating curve extracted from the simulations can be fitted well using the ellipse law indicates that a well designed turbine can be run at high efficiency over the entire operating range, especially if a variable speed drive train is used, i.e. the blade speed may be adjusted.

The lowest value for the mass flow is equal to 42 % of the maximum. This means that the mass flow range to be covered by the solar chimney turbine is much smaller than for turbines in some other applications. Another important parameter for the design of the PCU is the temperature at the turbine inlet. In the reference data set it ranges from 15 to 63 °C.

A widely used approach in wind turbine engineering to get a yield estimate for a specific location is to combine its wind speed distribution—how many hours per year does the wind blow at a certain wind speed—with the power curve of a potential wind turbine—how much power is produced at a certain wind speed

Table 1.1 Main features of the reference plant.

Collector diameter	7.0 km
Chimney height	1.5 km
Chimney diameter	160 m
Collector glazing	single
Heat storage device	none
Ambient wind effects	not included
Chimney shadow effects	included

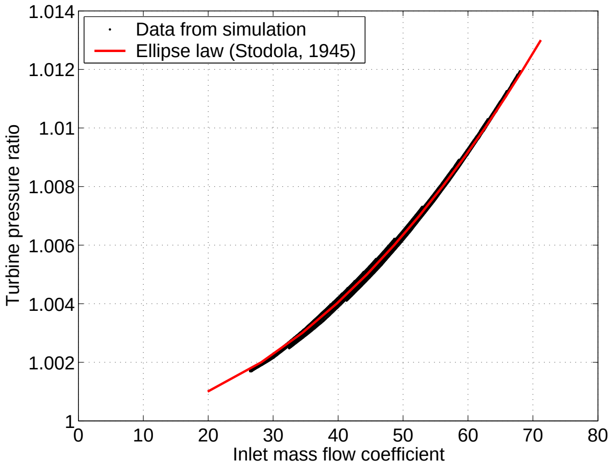

Figure 1.4 Turbine pressure ratio vs. mass flow coefficient from simulations compared to a curve following the ellipse law of Stodola (1945).

(Gasch *et al.*, 2002). Similarly we can extract the number of hours per year for each mass flow from the SCPP performance data and multiply it with the average power produced at this mass flow to get a yield estimate (Fig. 1.5, p. 16). Here, and in many publications found in the literature, a conversion efficiency from fluid power to electrical power of 80 % is assumed for the solar chimney power conversion unit, independent of operating condition. This value is reached, for example, if both, the drive train and the turbine (total-to-total), achieve an efficiency of a little less than 90 %. Looking at the literature, for example the work of Gannon (2002) and Von Backström and Gannon (2004) for the turbine and the work of Poore and Lettenmaier (2003) and Bywaters *et al.* (2004) for the drive train, the 80 % value seems like a reasonable assumption. This assumption will be discussed further in this dissertation, e.g. in Section 5.3 (p. 60).

1.4.2 Models for Plant Cost and O&M Cost

In this section the cost for collector and chimney of the reference plant is determined with a cost model used by Bernardes (2004). According to Bernardes (2004) a chimney of 1500 m height and 160 m diameter has an initial cost of 272 M€. For the PCU he assumes a cost of 767 € per kW rated power.

To evaluate the cost of the collector he assumes that the collector is built from steel, glass, concrete and corrugated iron and sums up the products of specific material price and amount of material required to build one meter squared of collector. With this method he gets a very low specific collector cost of 9.85 €/m^2, which is less than half of the specific cost of the collector built in Manzanares in the early eighties of the previous century (23 €/m^2). Using this specific collector cost and the geometrical data for the collector given above we get a total collector cost of 379 M€. The cost assumptions for the materials used in the construction

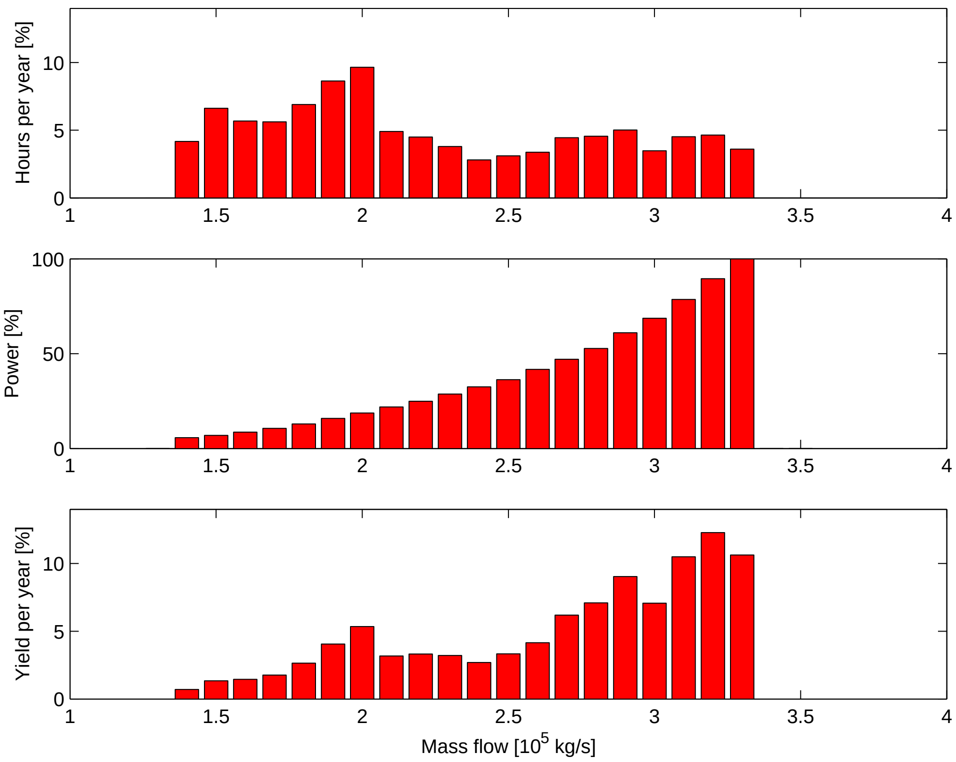

Figure 1.5 Calculation of the yearly yield

Table 1.2 Material cost for the collector.

	Steel	Glass	Concrete
Amount/m^2	5.089 kg	1.0 m^2	1.86E-03 m^3
Cost per unit	1.02 €/kg	3.72 €/m^2	503.64 €/m^3
Cost €/m^2	5.19	3.72	0.94

of the collector are summarized in Table 1.2.

From the data of Schlaich (1995) and assuming a conversion rate from DM to € of 0.5, it can be shown that the operating cost in € for the first year is linearly proportional to the collector area in m^2 with the following trend:

$$OC_1 = 0.1364 A_c + 604481 \tag{1.2}$$

1.4.3 Cost of Electricity Evaluation

In this section it is shown how the cost of electricity is evaluated, what assumptions have been made and how results of this method compare to results found in the literature. With the values from the previous sections and the equations below, which have been taken from Riggs *et al.* (1996), the cost of electricity can be assessed.

In comparative studies of investment opportunities it is common to assume that the project has been built and is ready to go into operation. It is further assumed that the credit for the initial investment has been received at the beginning of the construction period and interest for this period has to be allowed for. The present value of the capital cost, PCC, can then be derived from the following two equations, where CC_0 is the capital cost according to today's prices and CC_{N_c} is the capital cost according to the prices at the beginning of the construction period.

$$CC_{N_c} = CC_0 \frac{1}{(1+g)^{N_c}} \tag{1.3}$$

$$PCC = CC_{N_c}(1+i)^{N_c} \tag{1.4}$$

The operating and maintenance cost is growing over the years due to inflation and its present value can be assessed from the operating and maintenance cost for the first year (sec. 1.4.2) and the following equation:

$$POC = OC_1 \frac{1-(1+g)^N(1+i)^{-N}}{(1-g)} \tag{1.5}$$

Neglecting the impact of insurance cost and tax incentives the present value of the total cost P is equal to the sum of the present value of the operating cost POC and the present value of the capital cost PCC. The equivalent annual cost is

$$EAC = P\frac{i(1+i)^N}{(1+i)^N-1} \tag{1.6}$$

The levelized cost of electricity is equal to the fraction of the equivalent annual cost and the annual energy yield E:

$$COE = \frac{EAC}{E} \tag{1.7}$$

For the present study the following parameters have been set:

i	interest rate = 8 %
g	inflation rate = 3.5 %
N	depreciation period = 30 years
N_c	construction period = 2 years

1.4.4 Results

Figure 1.6 shows how the cost of electricity changes with PCU efficiency and cost of PCU per kW installed power. The cost of PCU per kW installed power is given relative to the value quoted by Bernardes (2004), which is 767 € per kW. The cost of electricity is rather sensitive to the efficiency of the PCU and rather insensitive

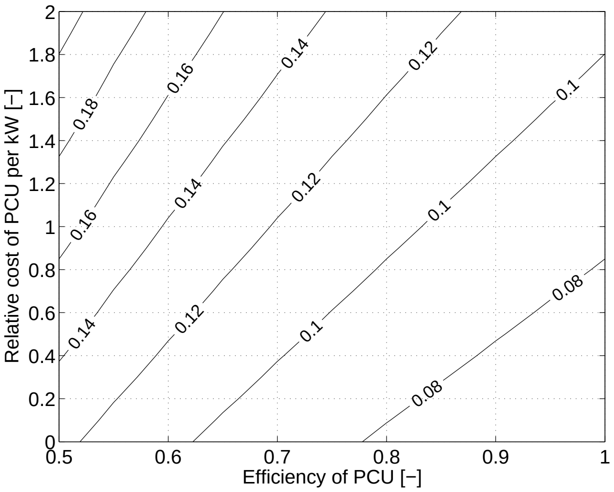

Figure 1.6 Cost of electricity in € for various values of PCU efficiency and relative cost of PCU per kW installed power.

to its cost. Let us for example assume we could build a PCU with a constant efficiency of 80 % and a cost of 767 € per kW nominal power. From Figure 1.6 we find a resulting COE of around 0.104 €/kWh. Discovering that another layout would only provide an efficiency of 70 % we can read from Figure 1.6 that it would have to cost about half the previous one in order to provide the same COE.

Another interesting piece of information from this figure is that, even when moving into the unrealistic but favourable right bottom corner of the figure, where the efficiency of the PCU is high and its cost is low, the cost of electricity remains far above the values achievable with gas or coal fired or nuclear power plants (Sims *et al.*, 2003).

Schlaich (1995) also calculates the cost of electricity; using the above equations, the data of Schlaich (1995) for capital cost, operating cost and yield, and assuming, as Schlaich, zero years of construction, one can exactly reproduce his results. E.g. with an interest rate of 8 %, a growth rate of 3.5 % and a depreciation period of 20 years, a 100 MW plant delivers electricity at 0.209 DM/kWh, which is equivalent to 0.105 €/kWh.

Surprisingly Bernardes (2004) quotes much lower values for a similar 100 MW plant; with an interest rate of 8 %, a growth rate of 3.25 %, a depreciation period of 30 years, a construction period of 2 years, higher capital cost and lower yield than Schlaich he gets a very low cost of electricity of 0.037 €/kWh. Using the above equations the cost of electricity is 0.127 €/kWh, which is 3.4 times higher than the value obtained by Bernardes (2004). This discrepancy is due to an error in the procedure for evaluating the cost of electricity used by Bernardes (2004).

Chapter

2

Turbine Modelling and Layouts

For the turbogenerators several layouts have been proposed in the solar chimney literature. The objective of this chapter, which is an extended version of the paper by Fluri and Von Backström (2007), is to compare these layouts using various modelling approaches. The basis of the model used here is taken from the work of Denantes and Bilgen (2006), however, the evaluation of the turbine efficiency is modified (radial averaging is implemented, and secondary losses are taken into account), a limit to the degree of reaction of the turbine is introduced to avoid diffusion at the hub, and the single rotor layout without inlet guide vanes is also considered.

A review on solar chimney turbine literature is presented in the first section. Then, a description of the various layouts is given and the structure of the computer program set up for the comparison is described. The analytical models of the four layouts are presented in the section after. Then, the various layouts and the various modelling approaches are compared and the conclusions are presented.

2.1 Literature Review

As mentioned in Section 1.2.1, Schwarz and Knauss (1981) designed the turbogenerator for the pilot plant in Manzanares. For the turbine they chose a single rotor layout without guide vanes. Gannon and Von Backström (2002) proposed a single rotor layout for a large-scale solar chimney, in which they made use of the chimney support structure as inlet guide vanes (as shown in Fig. 1.1 on page 2). They present an analytical model, which is adapted from gas turbine literature, for this layout and show that the inlet guide vanes improve the performance (Von Backström and Gannon, 2004). They also point out that the values for specific speed and diameter for a solar chimney turbine lie between the ones of gas turbines and wind turbines.

More recently, Denantes and Bilgen (2006) introduced an alternative layout consisting of one pair of counter rotating rotors, either with or without inlet guide vanes. They modified the analytical model of Von Backström and Gannon (2004) to accommodate layouts with counter rotating rotors and to compare their performance to the one of the single rotor layout with inlet guide vanes. They find that the single rotor layout has a higher efficiency at the design point but a lower efficiency at off-design conditions.

Denantes and Bilgen (2006) base their work on counter rotating turbines on earlier gas turbine and water turbine publications (Ozgur and Nathan, 1971; Louis, 1985; Cai *et al.*, 1990). Ozgur and Nathan (1971) compare an axial flow counter rotating water turbine consisting of one rotor pair without inlet guide vanes to a single rotor turbine with inlet guide vanes. Louis (1985) compares two counter rotating layouts, both with one rotor pair but one with and one without inlet guide vanes, to single rotor layouts with inlet guide vanes.

Cai *et al.* (1990) also look at axial counter rotating turbine layouts with or without guide vanes. In the earlier publications (Ozgur and Nathan, 1971; Louis, 1985) the rotational speed was assumed to be of equal magnitude for the two rotors and the flow was assumed to leave the turbine without swirl. In the study of Cai *et al.* (1990) a difference in rotor speed has been allowed for, and, as an alternative to the zero exit swirl condition, layouts were studied where the exit swirl component is not zero but equal to the swirl component at the inlet.

In the study of Denantes and Bilgen (2006) the speeds of the two rotors are also independent from each other and the exit swirl component is not limited to a certain value.

2.2 Description of Layouts

A multiple horizontal axis turbine configuration, as shown at the bottom in Figure 1.2 (p. 8), is chosen here, and, following the trends in the technology of large wind turbines, it is assumed that a variable speed drive train is used in all layouts (Bywaters *et al.*, 2004; Poore and Lettenmaier, 2003). The turbine layouts considered in this chapter are shown in Figure 2.1. A brief description of each layout is provided here:

Single rotor turbine without IGVs: With only one blade row the single rotor turbine without IGVs is the simplest layout. Its biggest disadvantage is that the swirl induced by the rotor cannot be recovered (Schwarz and Knauss, 1981).

Single rotor turbine with IGVs: This layout is a single rotor axial flow turbine stage with inlet guide vanes. The swirl is induced by guide vanes, which are located upstream of the rotor. The rotor turns the flow back to a close to axial direction.

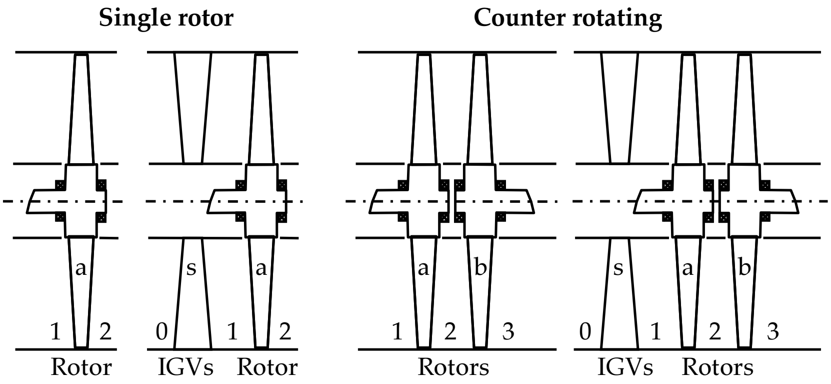

Figure 2.1 Schematic drawing of turbine layouts.

Counter rotating turbine without IGVs: This layout consists of two counter rotating rotors; the first rotor induces the swirl and the second rotor turns the flow back to a close to axial direction.

Counter rotating turbine with IGVs: With three blade rows, two counter rotating rotor rows and a row of inlet guide vanes, this is the most complex layout. The inlet guide vanes induce swirl in one direction. The first rotor turns the flow and induces swirl in the opposite direction. The second rotor finally turns the flow back to a close to axial direction.

Exit guide vanes are not considered in this study. They are generally not used in turbines due to their inferior efficiency compared to inlet guide vanes; in an exit guide vane row the flow is decelerating, which induces greater blade row losses (Hill and Peterson, 1992).

2.3 Turbine Modelling

2.3.1 Structure of the Program

The program to enable the comparison of the layouts is structured as follows (Fig. 2.2):

1. *Geometry definition.* The geometry of the flow passage and the turbine is defined. It is assumed that the diameter of the chimney is given and hence the chimney inlet area is known. The diffuser area ratio is defined as $R_d = A_c/A_{tt}$, where A_c is the chimney area and A_{tt} is the total turbine area. It may be used as a design variable in order to investigate whether including a nozzle ($R_d < 1$) or a diffuser ($R_d > 1$) after the turbine improves the plant performance. The number of turbines is specified. The blade aspect ratio, R_{asp}, and the hub-to-tip radius ratio, R_{HT}, are set.

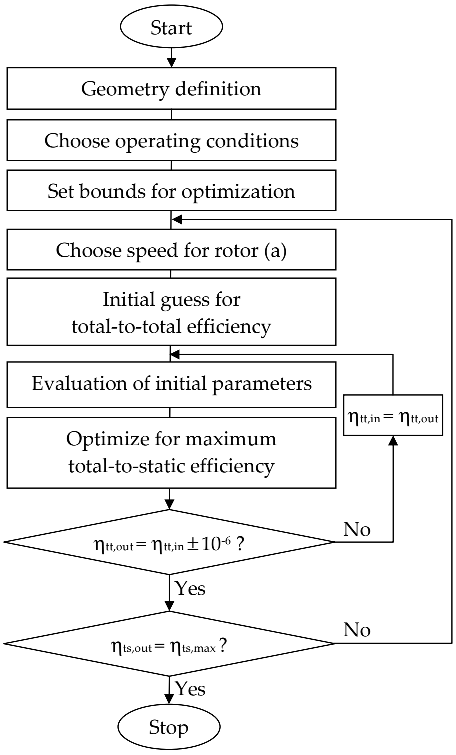

Figure 2.2 Flow chart of the algorithm.

2. *Choose operating conditions.* The operating point and the working fluid are specified. The operating point is given with inlet total temperature, T_{t0}, inlet total pressure, p_{t0}, exit total pressure, p_{t4}, which is also the chimney inlet pressure, and mass flow, $\dot{m}$. The working fluid is assumed to be dry air. We assume incompressibility and the density is taken as $\rho = p_{t4}/(R\,T_{t0})$. Which positions the numbers in the subscripts refer to is clarified in Figure 2.1.

3. *Set bounds for optimization.*

4. *Choose speed for rotor (a) (Fig. 2.1).*

5. *Initial guess.* An initial guess for the total-to-total turbine efficiency and the design variables, which will be defined in Section 2.3.2, is made.

6. *Evaluation of initial parameters.* The axial components of the chimney inlet and the turbine exit flow velocities are

$$C_{x4} = \frac{\dot{m}}{A_c\,\rho} \tag{2.1}$$

$$C_{x3} = C_{x4}\,R_d \tag{2.2}$$

The static pressure at the exit and the temperature and enthalpy difference over the turbine are evaluated from

$$p_4 = p_{t4} - 0.5\,\rho\,{C_{x4}}^2 \tag{2.3}$$

$$\Delta T = \eta_{tt} T_{t0} \left(1 - \left(\frac{p_{t1}}{p_{t4}}\right)^{\frac{\gamma}{\gamma-1}}\right) \tag{2.4}$$

$$\Delta h = c_p\,\Delta T \tag{2.5}$$

The stage load coefficient Ψ and flow coefficient Φ can be evaluated from

$$\Psi = \frac{\Delta h}{{U_a}^2} \tag{2.6}$$

where U_a is the absolute blade speed of the first rotor, and

$$\Phi = \frac{C_x}{U_a} \tag{2.7}$$

7. *Optimize for total-to-static efficiency.* Utilizing the specific turbine model, which will be described in detail below, an optimization algorithm is run to get the maximum total-to-static efficiency at this particular speed of the first rotor. As long as the total-to-total efficiency value has not converged we iterate. At each iteration the efficiency result is taken as the new initial guess. The optimization algorithm used here is the function "fmincon", which is the Sequential Quadratic Programming implementation for constrained optimization in Matlab.

8. *Detect optimal speed of rotor (a).* The above iteration is executed with new values for the speed of rotor (a), until the speed providing the maximum total-to-static efficiency has been detected.

2.3.2 Mathematical Turbine Models

The model for the counter rotating layout with inlet guide vanes is described in detail here. It serves as a basis for all the other models. Having three blade rows, it is the most complex one, and the others can be derived from it by simply deleting one or two blade rows and their impact on the flow (Fig. 2.1). Therefore the model for the first layout is described in detail. The model has been adapted from the work of Denantes and Bilgen (2006).

Some assumptions:

- The mass flow is equally shared by the various turbines.
- No turbine flare.
- Constant axial velocity through turbine: $C_x = C_{x1} = C_{x2} = C_{x3}$

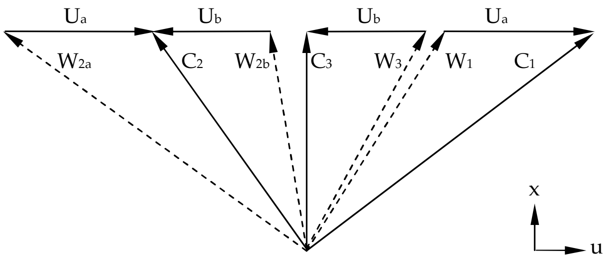

Figure 2.3 Velocity triangles of a counter rotating turbine stage with inlet guide vanes.

- Zero swirl at turbine inlet: $C_{u0} = 0$
- Free vortex design

The design variables for the optimization are the dimensionless blade speed of the second rotor (Fig. 2.3), the degree of reaction of the first rotor and the degree of reaction of the second rotor.

The dimensionless blade speed of the second rotor is defined as

$$u_b = \frac{U_b}{U_a} \tag{2.8}$$

the degree of reaction of the first rotor as

$$R_{n,a} = 1 - (c_{u2} + c_{u1})/2 = -(w_{u2a} + w_{u1})/2 \tag{2.9}$$

and the degree of reaction of the second rotor as

$$R_{n,b} = 1 - \frac{c_{u3} + c_{u2}}{2u_b} = -\frac{w_{u3} + w_{u2b}}{2u_b} \tag{2.10}$$

The small letters c and w denote dimensionless absolute and relative flow velocities respectively and the subscript u indicates the circumferential direction.

The degree of reaction, represents the ratio of the static pressure drop to the stagnation pressure drop over a turbine rotor (Wilson and Korakianitis, 1998). The above equations can be derived using the Euler turbine equation, the velocity diagram (see Fig. 2.3) and assuming the axial component of the flow velocity to be equal at rotor inlet and outlet. For a derivation of equation 2.9 refer to Von Backström and Gannon (2004). Denantes and Bilgen (2006) use a slightly different parameter for the second rotor, which is equal to the actual degree of reaction multiplied by u_b. The load coefficients are defined as follows:
Stage load coefficient:

$$\Psi = c_{u1} - c_{u2} + u_b(c_{u2} - c_{u3}) \tag{2.11}$$

Load coefficient of the first rotor:

$$\Psi_a = c_{u1} - c_{u2} \tag{2.12}$$

Load coefficient of the second rotor:

$$\Psi_b = u_b(c_{u2} - c_{u3}) \tag{2.13}$$

Using these definitions and some algebraic manipulations the following dimensionless velocity components are obtained:

$$c_{u1} = 1 - R_{n,a} + \Psi_a/2 \tag{2.14}$$

$$w_{u1} = c_{u1} - 1 = -R_{n,a} + \Psi_a/2 \tag{2.15}$$

$$c_{u2} = 1 - R_{n,a} - \Psi_a/2 \tag{2.16}$$

$$w_{u2,a} = c_{u2} - 1 = -R_{n,a} - \Psi_a/2 \tag{2.17}$$

$$c_{u2} = u_b(1 - R_{n,b}) + \frac{\Psi_b}{2u_b} \tag{2.18}$$

$$w_{u2,b} = c_{u2} - u_b = -u_b R_{n,b} + \frac{\Psi_b}{2u_b} \tag{2.19}$$

$$c_{u3} = u_b(1 - R_{n,b}) - \frac{\Psi_b}{2u_b} \tag{2.20}$$

$$w_{u3} = c_{u3} - u_b = -u_b R_{n,b} - \frac{\Psi_b}{2u_b} \tag{2.21}$$

Using Pythagoras's relations all the flow angles and velocity components can now be evaluated similar to the following two examples, the IGV exit flow angle and the dimensionless IGV exit velocity squared:

$$\alpha_1 = \arctan\frac{c_{u1}}{\Phi} \tag{2.22}$$

$${c_1}^2 = \Phi^2 + {c_{u1}}^2 \tag{2.23}$$

Assuming that the swirl remains constant from the exit of the turbine to the chimney inlet[1], the flow velocity at the chimney inlet is obtained from:

$${c_4}^2 = {c_{x4}}^2 + {c_{u3}}^2 \tag{2.24}$$

Equating 2.16 in 2.18 gives

$$\Psi_b = 2u_b\big(1 - R_{n,a} - \Psi_a/2 - u_b(1 - R_{n,b})\big) \tag{2.25}$$

and with $\Psi = \Psi_a + \Psi_b$

$$\Psi_a = \frac{\Psi - 2u_b(1 - R_{n,a} - u_b(1 - R_{n,b}))}{1 - u_b} \tag{2.26}$$

With this a model has been obtained, which depends only on the three design variables and on the chosen turbine speed and operating conditions.

---

[1] This does not represent the real situation, but whether the swirl component is lost through friction or as exit loss at the chimney top, its effect on the turbine performance is the same.

Losses and Efficiency

For profile losses Hawthorne's simplification of Soderberg's correlation is implemented, where ϵ denotes the flow deflection (Horlock, 1966):

$$\zeta_p = 0.025\left(1+\left(\frac{\epsilon}{90°}\right)^2\right) \tag{2.27}$$

Hawthorne also gives a correlation for secondary loss implying it to be proportional to the profile loss and the blade aspect ratio:

$$\zeta_{sec} = \zeta_p \frac{3.2}{R_{asp}} \tag{2.28}$$

The blade aspect ratio is taken as $R_{asp} = l_b/b_x$, where l_b is the blade length and b_x is the axial chord of the blade. Adding the secondary to the profile loss and neglecting tip leakage and annulus losses the overall loss coefficient for a single blade row becomes:

$$\zeta = 0.025\left(1+\left(\frac{\epsilon}{90°}\right)^2\right)\left(1+\frac{3.2}{R_{asp}}\right) \tag{2.29}$$

This loss model has been employed by many authors, e.g. Gannon and Von Backström (2002); others chose to neglect secondary losses, e.g. Von Backström and Gannon (2004) and Denantes and Bilgen (2006).

The total-to-static efficiency is

$$\eta_{ts} = \frac{1}{1+\frac{\zeta_{IGV}{c_1}^2+\zeta_a{w_{2a}}^2+\zeta_b{w_3}^2+{c_4}^2}{2\Psi}} \tag{2.30}$$

The total-to-total efficiency can be assessed from

$$\eta_{tt} = \frac{1}{1+\frac{\zeta_{IGV}{c_1}^2+\zeta_a{w_{2a}}^2+\zeta_b{w_3}^2}{2\Psi}} \tag{2.31}$$

The loss coefficients and the relative velocities are evaluated at seven equally spaced radial stations along the span of the blades, and the final value of the efficiencies is area-averaged.

Torque Evaluation

The torque on the rotors is assessed from $T_q = P/\omega$, where P is the power and ω is the rotational speed. The power is evaluated from the well-known Euler turbine equation. The rotational speed can be written as $\omega = U/r$. Combining the above gives the following equations for the torque:

$$T_{q,a} = \dot{m}U_a r_m(c_{u1} - c_{u2}) \tag{2.32}$$

$$T_{q,b} = \dot{m}U_a r_m(c_{u2} - c_{u3}) \tag{2.33}$$

Solidity and Number of Blades

Implementing the above loss model it is assumed that the turbine operates near optimum solidity. With the flow angles, the blade aspect ratio, the hub-to-tip radius ratio and the through flow area given, the number of blades is the only free parameter controlling the solidity.

According to Wilson and Korakianitis (1998) minimum-loss solidities are found by setting the tangential lift coefficient, C_L, at a constant value between 0.8 and 1.2. In the following the optimum lift coefficient is assumed to be equal to unity. The optimum axial solidity can be found using their equation 7.5, which is reiterated here for convenience

$$\left(\frac{b_x}{s}\right)_{opt} = \left|\frac{2}{C_{L,op}} cos^2 \alpha_{ex} (\tan \alpha_{in} - \alpha_{ex})\right| \tag{2.34}$$

b_x is the axial blade chord, s is the spacing between the blades and α_{in} and α_{ex} are the flow angles at blade row inlet and outlet. The axial chord of the blade can be approximated with

$$b_x = c_h cos\left(\frac{\alpha_{in} + \alpha_{ex}}{2}\right) \tag{2.35}$$

where c_h is the actual blade chord and the fraction denotes an average flow angle through the blade row. The blade chord is obtained by dividing the blade length, $l_b = r_t(1 - R_{HT})$, by the blade aspect ratio, R_{asp}. The optimum number of blades can then be obtained from

$$Z = 2\pi r_m \frac{(b_x/s)_{opt}}{b_x} \tag{2.36}$$

Constraints

The degree of reaction of a free-vortex turbine stage changes along the blade. The lowest degree of reaction is found at the hub and the highest at the tip. To avoid recompression at the hub, which would most probably lead to flow separation and performance deterioration, the degree of reaction should not be less than that of an impulse stage, which is zero. The effect of this constraint, which has been ignored by other authors, is investigated here. Also, a lower limit for the dimensionless speed of the second rotor has been set to a 10^{th} of the first rotor's speed ($u_{b,min} = -0.1$).

Models for Other Layouts

As mentioned above, the models of the other three layouts can be derived from the one presented above by deleting blade rows and their impact on the flow. To model a turbine without inlet guide vanes, the absolute flow angle at the IGV exit, α_1, and the IGV loss coefficient, ζ_{IGV}, are both simply set to zero (Denantes and Bilgen, 2006). Modelling a single rotor turbine, two design variables, the degree of reaction and the dimensionless speed of the second rotor, $R_{n,b}$ and u_b, fall away. The loss coefficient of the second rotor, ζ_b, is set to zero, and the circumferential component of the turbine exit velocity, c_{u3}, is set equal to c_{u2}, the circumferential component of the exit velocity of the first rotor.

2.3.3 Geometry and Operating Conditions

The geometrical parameters, the operating conditions and the assumed values for the fluid properties are shown in Table 2.1. The operating conditions have been extracted from Von Backström and Gannon (2004). They are equal to the Case 2 discussed in the dissertation of Gannon (2002) from where also the geometrical parameters have been extracted. The blade aspect ratios and the hub-to-tip radius ratio are not optimized in the present dissertation. To optimize these parameters a model for the structural design is required. Developing such a model is beyond the scope of this dissertation, and the conservative values listed in Table 2.1 are used throughout.

Table 2.1 Geometrical parameters and operating conditions.

Chimney height	H_c	[m]	1500
Chimney diameter	d_c	[m]	160
Collector outer diameter	d_{col}	[m]	6000
Number of turbines	Z_t	[-]	32
Diffuser area ratio	R_d	[-]	1.0
IGV aspect ratio	$R_{asp,IGV}$	[-]	4.0
Rotor blade aspect ratio	$R_{asp,r}$	[-]	3.0
Hub-to-tip radius ratio	R_{HT}	[-]	0.4
Inlet total pressure	p_{t0}	[Pa]	90,000
Inlet total temperature	T_{t0}	[K]	333
Exit total pressure	p_{t4}	[Pa]	89,200
Mass flow rate	$\dot{m}$	[ton/s]	250
Specific gas constant	R	[J/kg]	287
Specific heat at constant pressure	c_p	[J/(kg K)]	1008
Ratio of specific heats	γ	[-]	1.4

2.4 Results

2.4.1 Comparison of Layouts

Efficiency

Figure 2.4 shows the efficiency prediction for the various turbine layouts over a range of turbine speeds. Most obviously the single rotor layout without IGVs is

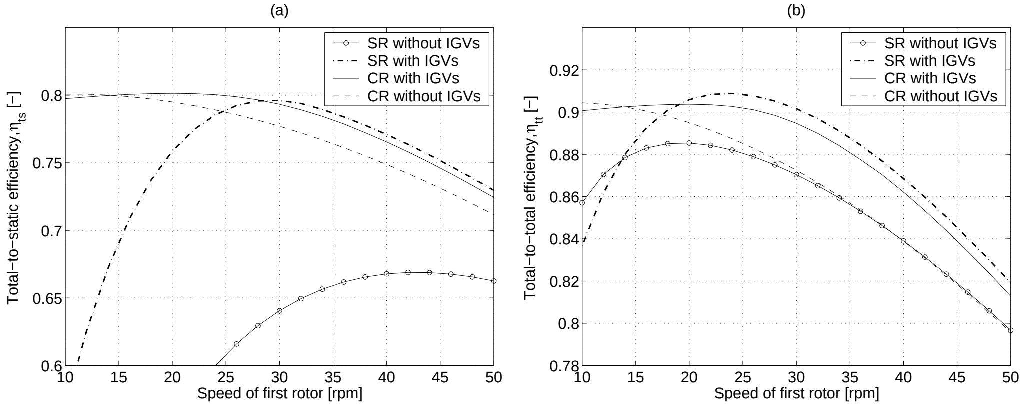

Figure 2.4 (a) Total-to-static and (b) total-to-total turbine efficiency prediction for various layouts.

unable to reach an acceptable total-to-static efficiency at any speed, with its peak lying at a 66.9 %, making either a stator or an additional rotor row inevitable. The peak total-to-static efficiency of the other three layouts lies in a narrow band between 79.6 (SR with IGVs) and 80.1 % (CR with IGVs). But the speed of the first rotor at which these three layouts reach their peak efficiency varies significantly. The single rotor turbine with IGVs performs very poorly, in terms of total-to-static efficiency, at low speeds, mainly due to high exit losses resulting from a high exit swirl, which is necessary to prevent diffusion at the hub. It performs best at 29.2 rpm. Going to higher speeds, the performance deteriorates mainly due to high rotor losses resulting from high relative flow velocities.

The counter rotating turbine with inlet guide vanes suffers from the same effect if the first rotor runs faster than at 20 rpm, which is the optimum speed of this layout for the given geometric parameters and operating conditions. Pushing the first rotor to higher speeds, the optimizer slows down the second rotor significantly (Fig. 2.5). As mentioned above the lower limit of the dimensionless speed of the second rotor has been set to a 10^{th} of the first rotor's speed ($u_{b,min} = -0.1$). This limit is reached at a speed of 34 rpm of the first rotor. For speeds lower than the optimum the performance deteriorates only slightly, since the exit swirl does not increase a lot. The counter rotating turbine without inlet guide vanes follows a similar trend as the previous layout, but its peak is shifted to the low speed side resulting in a high torque for high performance.

Torque

Size and cost of the drive train is proportional to the torque delivered by the turbine (Burton *et al.*, 2001). Since the power is proportional to the product of the rotational speed, ω, and the torque, T_q, speeding up the turbine obviously reduces the torque for the same power output. Since the performance peaks of

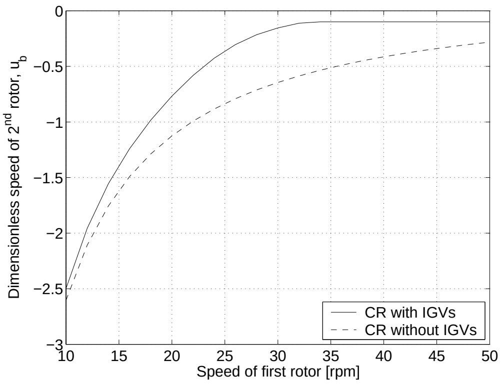

Figure 2.5 Dimensionless speed of the second rotor vs. speed of first rotor.

the counter rotating layouts lie at relatively low speed the torque on the shafts is high, leading to a bigger and more expensive drive train.

This is very pronounced without IGVs with a torque of 1.28 and 1.45 MNm for the two shafts respectively. With IGVs the torque is slightly higher in the first rotor (1.35 MNm) but lower in the second rotor (0.87 MNm). Even though the single rotor solution with IGVs has only one rotor to carry all the load, the torque at peak performance is relatively low (1.74 MNm) thanks to the high speed. The torque for the single rotor layout without IGVs follows a similar trend but on a lower level due to the lower efficiency.

Number of Blades

The required number of blades is dependent on the chosen blade aspect ratio. With the parameters chosen here, results are as follows: Besides the single rotor layout without IGVs, which requires only 6 blades, the layout with the lowest number of blades is the counter rotating turbine without IGVs, requiring 32 blades in its peak performance point (0 IGVs / 16 for the first / 16 for the second rotor). The single rotor layout requires 47 (31/16/0) and the counter rotating turbine with IGVs 66 blades (32/18/16).

Number of Turbines

Once the total turbine through flow area has been chosen, it can be shown that with the presented model the efficiency is independent of the number of turbines; the exit loss obviously remains constant, and the optimizer adjusts the speed in order to get the same optimal combination of flow and load coefficient resulting in the same blade losses. The number of turbines can hence be adjusted to suit the geometrical constraints, to give the desired torque per shaft and to minimize the cost of electricity.

2.4.2 Comparison of Various Modelling Approaches

The main difference between the turbine model presented here and earlier models of other researchers are the implementation of a model for secondary losses, averaging over several radial sections for efficiency evaluation and the constraint on the degree of reaction to prevent diffusion at the hub. In Table 2.2 the results compared to simulations where one or all of the above features of the model have been removed. The efficiency is generally higher for the simpler models—8.5 percentage points for the single rotor layout without IGVs and approximately 6 percentage points for the other three layouts, if all of the above features have been removed—and the optimum rotor speed is significantly shifted. Neglecting the secondary losses has the biggest impact on the efficiency.

Table 2.2 Turbine parameters for various layouts and modelling approaches—Model 1: current model; Model 2: no constraint preventing recompression at the hub; Model 3: no radial averaging; Model 4: no secondary loss model; Model 5: models 2, 3, and 4 combined.

Model			**Single rotor**		**Counter rotating**	
			no IGVs	with IGVs	no IGVs	with IGVs
1	η_{ts}	%	66.9	79.6	80.1	80.1
	N_a	rpm	42.8	29.2	10.9	20.0
	u_b	-	n/a	n/a	-2.35	-0.77
2	η_{ts}	%	66.9	80.2	81.0	80.7
	N_a	rpm	42.8	25.4	11.4	15.6
	u_b	-	n/a	n/a	-1.63	-0.95
3	η_{ts}	%	69.4	82.7	82.8	82.6
	N_a	rpm	45.8	32.1	7.5	26.0
	u_b	-	n/a	n/a	-3.84	-0.31
4	η_{ts}	%	73.3	83.6	84.1	84.2
	N_a	rpm	53.1	31.3	12.9	19.8
	u_b	-	n/a	n/a	-2.09	-0.93
5	η_{ts}	%	75.4	86.0	86.2	86.0
	N_a	rpm	56.8	33.8	7.8	23.1
	u_b	-	n/a	n/a	-3.89	-0.66

Removing the constraint on the degree of reaction has only a slight impact. But it does not affect all layouts in the same way: It has no impact on the single rotor layout without IGVs but increases the peak efficiency estimates of the three other layouts to various extents. This could induce a bias towards certain layouts.

2.5 Summary and Conclusions

In this chapter, a review on solar chimney turbine literature has been presented. A computer program for the comparison of various turbine layouts and the analytical turbine models used in that program have been introduced. The various layouts and modelling approaches have been compared. It has been shown that slight changes in the modelling of solar chimney turbines have a significant impact on the performance prediction. Neglecting secondary losses, for example, may lead to a significant overestimation of the turbine efficiency. Ignoring the constraint of recompression in the blade row, on the other hand, does not affect all layouts in the same way, which could lead to bad choices early in the preliminary phase of a large-scale solar chimney project.

It has also been found that the single rotor layout without IGVs is the simplest and cheapest layout, as it requires comparably few blades and a small drive train. Its total-to-static efficiency is low, however, because the swirl at the turbine exit cannot be recovered. For the three other layouts the maximum total-to-static efficiency is much better and lies in a narrow band, with the counter rotating turbines performing slightly better, however only at low speeds, which leads to a higher torque for the same power output.

Chapter

3

Experiments on Turbine Models

Very little experimental data from solar chimney turbines are available in the literature. Schlaich *et al.* (1995) present the results from the Manzanares plant. They also investigated various configurations with multiple turbines in an experimental model, but instead of having actual turbines in the model, they simulate the pressure drop over the turbine with wire mesh screens. The most in depth experimental study on a solar chimney turbine model is the one of Gannon (2002) who demonstrates a design method on a 1:177 scale turbine model of an inverted Kaplan type layout. The experimental results from this turbine are also presented by Gannon and Von Backström (2003). A schematic drawing of this layout is shown in Figure 1.1 on page 2.

In this chapter the two solar chimney turbine rigs of the University of Stellenbosch are described (Fig. 3.1) and experimental results obtained with those rigs are discussed. The experimental data for the single turbine rig has been extracted

Figure 3.1 Picture of single turbine (left) and multiple turbine rig at Stellenbosch University.

from the work of Gannon (2002) and is analyzed here. His experimental setup and the results are briefly summarized in Section 3.1. For the multiple turbine rig, the actual experimental work was done in the context of this dissertation, and this rig is therefore covered in more detail in Section 3.2.

3.1 Single Turbine Rig

The single turbine rig at Stellenbosch University was designed and built by Gannon (2002). He derived his design parameters from a simulation of a full scale plant located in Sishen, Northern Cape, South Africa, with a chimney height of 1500 m, a chimney diameter of 160 m and a collector outer diameter of 6000 m.

For the model, a turbine diameter of 0.72 m, a diffuser area ratio of 1.47 and a hub-to-tip ratio of 0.4 were selected and the turbine tip speed was set to 44.3 m/s, which is half the proposed full scale tip speed. See Figure 3.2 for a schematic of the rotor of the turbine model. The turbine blade profiles were designed using the Surface Vortex Method (Lewis, 1996) and an algorithm, which minimizes the maximum relative velocity. The aim of this approach was to get profiles with minimal drag.

The objectives of the experiment with this rig were the demonstration of effective turbine operation over the predicted design range, quantification of the design and off-design performance of the turbine, verification of the design performance prediction and investigation of the starting performance. It was found that the capacity of this turbine is slightly lower than predicted and that the design point is reached by reducing the rotor blade stagger angle measured from the axial direction by 2.8 degrees (Gannon, 2002).

A total-to-static turbine efficiency of 82.8 % was measured. This value is much higher than the 74.9 % predicted in the same dissertation using the Soderberg loss model. As one potential reason for that discrepancy Gannon (2002) mentions that the wall static measurements have been used for the total-to-static efficiency evaluation; with the exit swirl being high in this design, the exit static pressure measured at the casing is higher than the average value at the exit. The

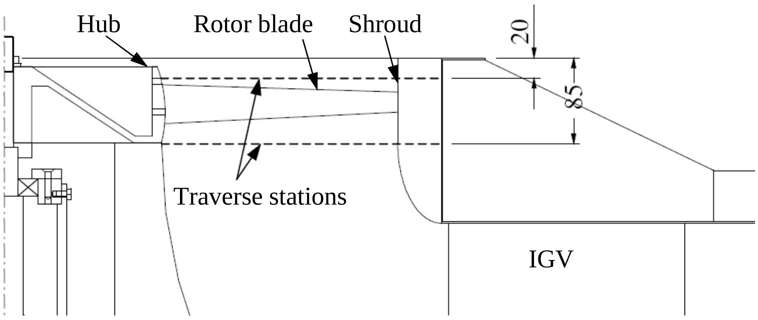

Figure 3.2 Schematic of the rotor of the single turbine rig (Gannon, 2002).

total-to-static efficiency was evaluated from

$$\eta_{ts} = \frac{T_q \omega}{Q(p_{t1} - p_{s3})} \tag{3.1}$$

where T_q denotes the torque, ω the rotational speed of the turbine, Q the volume flow rate, p_{t1} the total pressure at the turbine inlet and p_{s3} the static pressure at the turbine exit. A high value for the exit static pressure will therefore lead to a high value for the total-to-static efficiency.

Another reason for the difference in measured and predicted turbine efficiency is that the windmill anemometer used to measure the volume flow, according to Kirstein (2004), had an offset error of -3.2 %. Gannon (2002) also shows that the volume flow rate values obtained from the anemometer differ from values obtained from integrating the velocity profiles from radial five-hole probe traversing (the location of the probe traverse stations are shown in Fig. 3.2); the traverse results gave up to 8.5 % higher values. Measuring the volume flow too low will not only lead to a high value for the total-to-static efficiency through Equation 3.1 but also give a wrong indication on whether the design point was reached or not. Hence, the above mentioned reduction of the rotor blade stagger angle might have been unnecessary.

A high starting torque was found for this turbine, hence, unaided acceleration to design speed should be possible. The results of the experiments with the single turbine will be discussed further, and they will be compared to the multiple turbine rig results in Section 3.2.4 and to CFD results in Chapter 4.

3.2 Multiple Turbine Rig

The scope of the experiment with the multiple turbine rig was to assess the turbine performance with the nominal rotor and IGV blade angle settings and compare the results to the Soderberg correlation, to investigate the impact of the IGV wakes, to evaluate the blade profile loss coefficients and to quantify the effect of varying the rotor tip gap. The turbine for this rig has been designed and built by Coetzer (2006). Its design and manufacture, the experimental setup and the experimental results are described in the following sections.

3.2.1 Turbine Design and Manufacture

The turbine diameter, the hub-to-tip ratio, the number of rotor blades and the tip speed for the multiple turbine rig were chosen to be the same as in the single turbine rig[1]. This was done to enable the use of the same turbine hub, shaft, coupling, torque transducer and electrical generator. But instead of the inverted

---

[1] Turbine diameter $d_t = 0.72\,\text{m}$; hub-to-tip ratio $R_{HT} = 0.4$; number of rotor blades $Z_a = 12$; tip speed $U_a = 44.99\,\text{m/s}$.

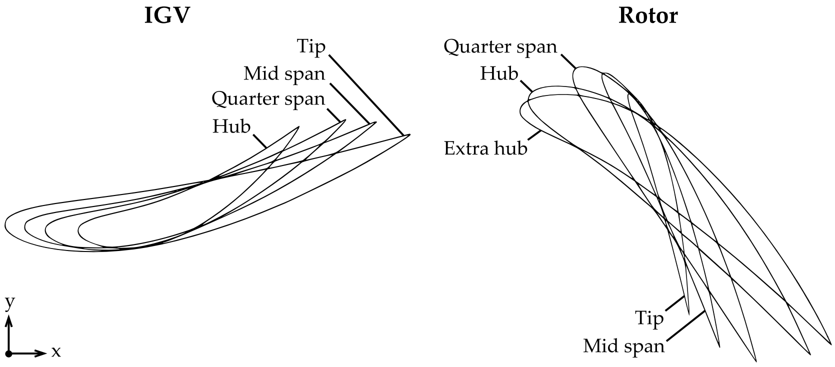

Figure 3.3 Sketch of IGV and rotor blade profiles stacked on center of gravity.

Kaplan type layout an axial turbine is investigated here. A schematic drawing of this plant configuration is shown at the bottom in Figure 1.2 (p. 8).

Assuming 32 turbines in the full scale rig and the same diffuser area ratio as with the single turbine rig ($R_d = 1.47$), this results in a model scale of 1:31. The design point is the same as for Case 2 in the work of Gannon (2002)[2].

Further assumptions for the turbine design were zero exit swirl, a free vortex design and constant axial velocity throughout the turbine. With these assumptions and the Soderberg loss model the flow angles can be found. The number of inlet guide vanes was set to 24. The rotor and IGV blade chord lengths were chosen using the method described on page 27. The IGV casing and the rotor hub have a spherical shape, so that the blade stagger angle can be changed without significant gap enlargement.

The software tool, Cascade, from Lewis (1996) was used to get the blade profile geometry for the rotor blade row and the IGVs. It was decided to use NACA 4-digit profiles and an incidence angle of +5 degrees. The resulting profiles were stacked on their centers of gravity (Fig. 3.3). The profile parameters at the various radial stations of the rotor and IGV blades are summarized in Table 3.1. The rotor blades were machined out of aluminium 6013. The IGVs were cast using a plastic resin[3].

3.2.2 Experimental Setup

The outlet of the multiple turbine rig is attached to the inlet of a wind tunnel (Fig. 3.4 and Fig. 3.1) and the centrifugal fan of the wind tunnel is used to suck air through the rig. To adjust the volume flow the speed of the fan can be controlled. An induction motor is connected to the end of the turbine shaft. It is run as a generator to act as a brake. Its speed can be controlled with a variable speed drive. The generated electrical power is dissipated in a resistor.

---

[2] The turbine total-to-total pressure drop is 285 Pa and the volume flow is 3.89 kg/m^3.

[3] Fastcast Polyurethane F18 with RZ 209/8 filler (aluminium powder).

Table 3.1 List of blade profile parameters for the multiple turbine rig.

		Position [mm]	**Chord** [mm]	**Stagger** [deg]	**Blade profile**
IGV	Hub	0.0	62.8	25.2	NACA 6416
	Quarter span	60.0	82.3	20.2	NACA 5414
	Half span	120.0	94.3	16.6	NACA 4412
	Tip	240.0	106.7	12.2	NACA 2411
Rotor	Extra hub	-13.9	97.5	-36.8	NACA 5416
	Hub	0.0	94.8	-42.7	NACA 4417
	Quarter span	54.0	85.0	-60.0	NACA 2415
	Half span	108.0	74.2	-70.5	NACA 1409
	Tip	216.0	56.8	-79.2	NACA 1408

Figure 3.4 Picture of the multiple turbine rig and the wind tunnel (detached to show the turbine rotor).

The following parameters are measured: turbine torque and speed, static pressure at the shroud in the three positions indicated in Figure 3.5 and at the hub at Position 2, volume flow as well as ambient pressure, which is taken as the total pressure at the inlet, and ambient temperature. Flow angles, the flow velocity as well as total and static pressure are obtained from radial traversing in Position 2 and 3 with the same 5-hole probe as used by Gannon (2002) and Kirstein (2004) who re-calibrated it. To assess the impact of the IGV wakes an area traverse is made in Position 2 using the same 5-hole probe.The measuring grid for that area traverse and the head of the 5-hole probe are shown in Figure 3.6. The 3-hole probe shown in the same figure was used for verification. The probe Reynolds number is $\mathrm{Re}_p = 3000$, which is in the non-critical range (Kupferschmied, 1998).

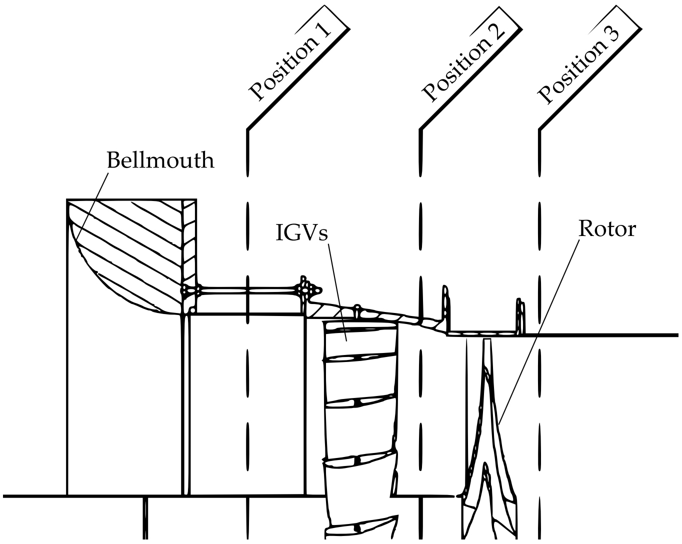

Figure 3.5 Sketch of the flow passage of the multiple turbine rig

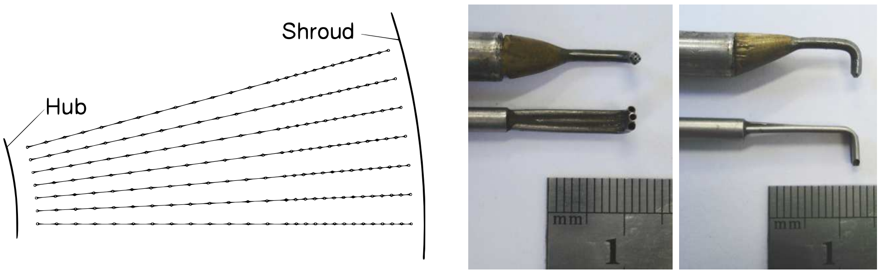

Figure 3.6 Measuring grid of the area traverse after the IGVs (left) and pictures of the heads of the 5-hole probe and the 3-hole probe.

The torque is measured with a torque meter installed on the shaft[4]. To measure the speed of the turbine a digital tachometer is used. The Venturi nozzle of the wind tunnel is used to measure the volume flow rate. The calibration of the torque transducer and the Venturi meter are given in Appendix A. All pressures are measured with pressure transducers of the type AutoTran 860 and AutoTran 750[5]. The experimental data is logged onto a computer with an Eagle Technologies data acquisition card and the software that comes with the card (WaveView)[6]

The rotor blade tips had accidentally been machined down too much, resulting in a rather large tip gap of 3 mm, which is equivalent to 1.5 % of the blade length (Coetzer, 2006). After a few initial test runs the gap was reduced by 2 mm,

---

[4] Specifications of the torque transducer: Type: HBM T5; Range: ±50 Nm; Accuracy: 0.002 % F.S.O.

[5] Accuracy: 2.2 Pa (Kirstein, 2004)

[6] Sample rate: 1 kHz; Number of samples per reading: 2000

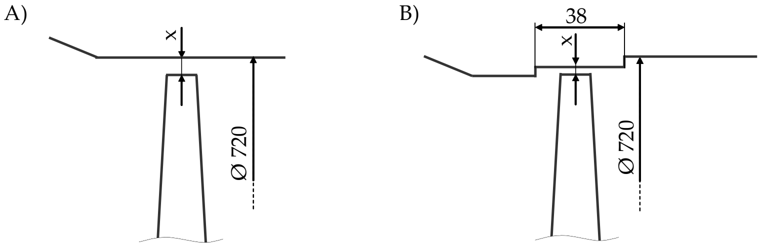

Figure 3.7 Sketch of the two tip gap geometries; Geometry A with a large gap and a straight duct (left) and Geometry B with a small gap and a step upstream of the rotor leading edge (right).

and a 2 mm high step was introduced 20 mm upstream of the rotor leading edge (see Fig 3.7). The geometry with the larger gap was only used in the tests to compare the tip gap geometries. In all other tests the geometry with the smaller gap and the steps was used.

3.2.3 Post Processing

The experimental results from the multiple turbine rig are evaluated in a similar way as presented in the dissertation of Gannon (2002). The exact procedure is shown here.

The total-to-total efficiency is evaluated from

$$\eta_{tt} = \frac{T_q \omega}{Q(p_{t1} - p_{t3})} \tag{3.2}$$

and the total-to-static efficiency from

$$\eta_{ts} = \frac{T_q \omega}{Q(p_{t1} - p_{s3})} \tag{3.3}$$

The torque, T_q, the rotational speed of the turbine, ω, the volume flow rate, Q, and the total pressure at the turbine inlet, p_{t1}, are measured as described in Section 3.2.2. Total and static pressure after the rotor, p_{t3} and p_{s3}, are obtained from the 5-hole probe, which is placed at the area halving radius whenever no radial traverses are made.

The flow coefficient is

$$\Phi = \frac{C_x}{U} \tag{3.4}$$

where C_x is the axial component of the absolute flow velocity, which is taken as the volume flow rate divided by the turbine annulus area, and U is the turbine tip speed.

The load coefficient is

$$\Psi = \frac{P_t}{U^2 \dot{m}} \tag{3.5}$$

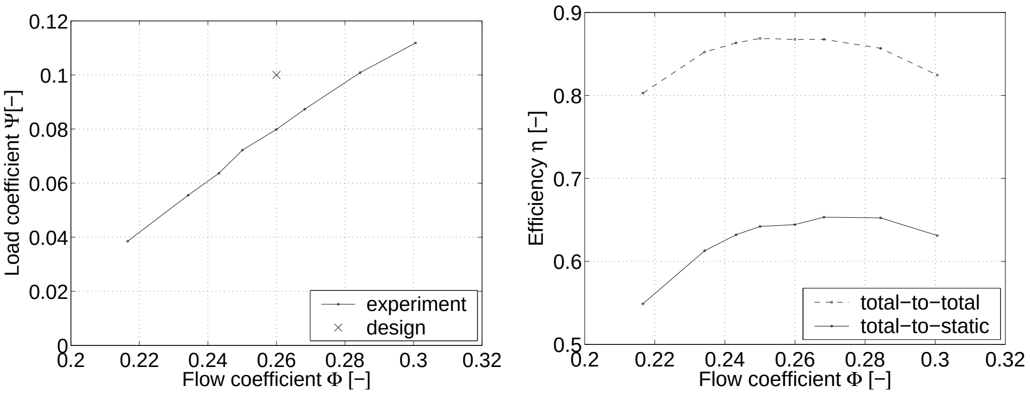

Figure 3.8 Plot of load coefficient vs flow coefficient (left) and efficiency vs flow coefficient (right) for nominal blade angle settings, as tabulated on page 96.

where P_t is the turbine power and $\dot{m}$ is the mass flow.

The profile loss coefficients are evaluated along streamlines from

$$\zeta_p = \frac{p_{t1,rel} - p_{t2,rel}}{\frac{1}{2}\rho w^2} \tag{3.6}$$

where $p_{t1,rel}$ is the relative total pressure at the inlet of the blade row, $p_{t2,rel}$ is the relative total pressure at the exit of the blade row, ρ is the density and w is the relative flow speed at the exit of the blade row.

3.2.4 Experimental Results

The plots representing the experimental results are shown in this section; the actual data are tabulated in Appendix C (pp. 96).

Turbine Characteristic

The experiment shows that the turbine capacity is slightly higher than design (Fig. 3.8). The maximum total-to-total efficiency is 86.5 % (±0.5), which is reasonably close to the result from the Soderberg loss model applied on data on the area halving radius (84.8 %)[7]. The maximum total-to-static efficiency is 65.1 %. The wakes after the IGVs are quite strong (Fig. 3.9). Therefore the data after the IGVs are circumferentially averaged.

Velocity Components

In Figures 3.10 and 3.11 the velocity components from the experiment on the multiple turbine rig and from Gannon (2002) are plotted. As a result of the different design approaches, the tangential velocity components are very different for

---

[7] Details on the error estimation and on how the Soderberg model was applied here are given in the Appendices B (pp. 94) and D (pp. 99).

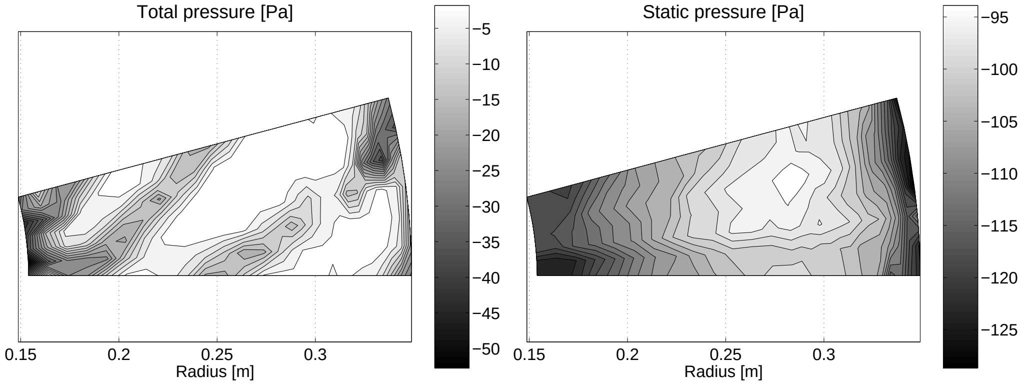

Figure 3.9 Contour plot of total pressure (left) and static pressure (right) after the IGVs.

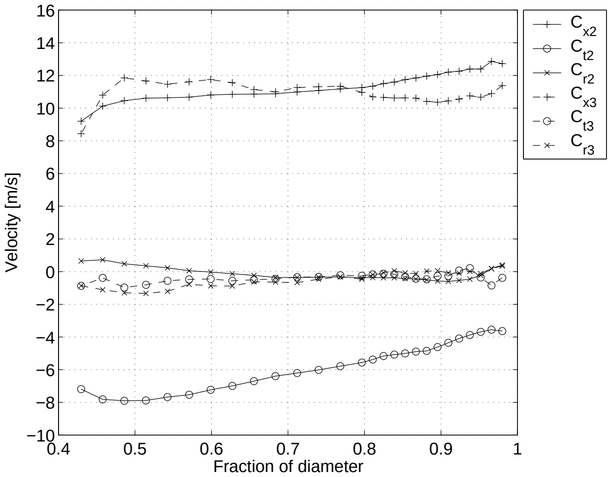

Figure 3.10 Velocity components measured on the multiple turbine rig, as tabulated on pp. 97.

the two cases. The multiple turbine model has a free vortex design and was designed for zero exit swirl. The single turbine model design had a heavy constraint on the maximum deflection in the inlet guide vanes. As a consequence hardly any pre-swirl is induced but a lot of exit swirl is present. In the multiple turbine case a tangential velocity distribution close to a classical free vortex distribution can be observed at the rotor inlet; at the outlet almost no swirl is present, which was the design intent.

Radial components are small in both cases. The average axial velocity component should be the same for both models, because both experiments were run at the same volume flow and the through flow areas are the same. Oddly, the average axial velocity component is higher for the single turbine model. And integrating the velocity profile from this plot with the area to assess the volume

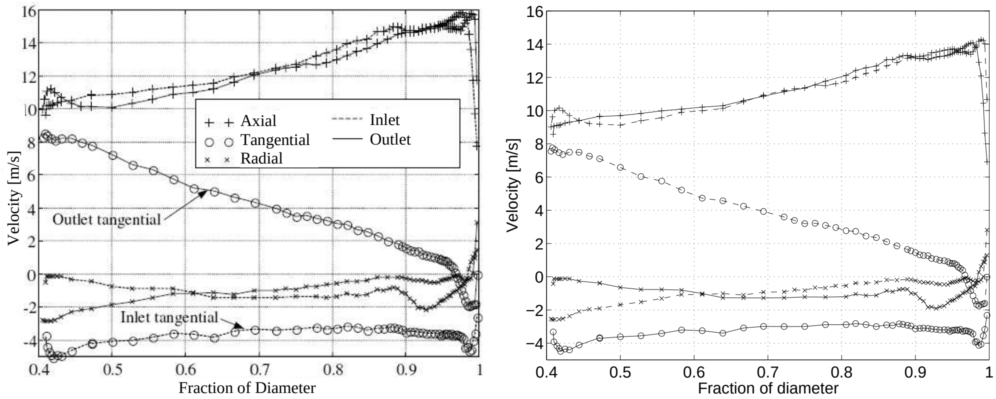

Figure 3.11 Velocity components of the single turbine model; figure from the dissertation of Gannon (2002) (left) and plot made from values taken from the appendix of the same dissertation.

flow we get a value which is 10 % too high. This is, however, not the case if the values given in the appendix of the dissertation of Gannon (2002) are used to do the integration. The velocity profiles derived from these values are also shown in Figure 3.11. This issue will be discussed further in the chapter on CFD.

For the multiple turbine rig the volume flow rate values obtained from integrating the velocity profiles from radial five-hole probe traversing are between 2.8 % (before) and 2.9 % (after the rotor) lower than the values obtained from the Venturi nozzle.

Profile Loss Coefficients

The profile loss coefficients extracted from the experimental data of the single and multiple turbine rigs are compared in Figure 3.12. At the mean area radius values of around 0.045 have been found for the IGVs and 0.067 for the rotor. Close to hub and tip of the IGVs the loss coefficient increases considerably[8].

The loss coefficient distribution is slightly ragged. A possible reason for this is that the wakes from the IGVs persist across the rotor row and are still visible in the exit traverse results. Only one radial traverse was done after the rotor and, hence, no circumferential averaging is possible. In the dissertation of Gannon (2002) the rotor loss coefficient of the single vertical axis turbine rig has the wrong sign for parts of the span[9]. With the evaluation procedure presented here this is not the case any more, and for both blade rows a profile loss coefficient of around 0.04 is found at the mean area radius.

---

[8] Sample calculations for the evaluation of the loss coefficients can be found in Appendix D.2 (pp. 100).

[9] In the work of Gannon (2002) the loss coefficients are defined in a way that they should be negative by default; but they are positive for parts of the span.

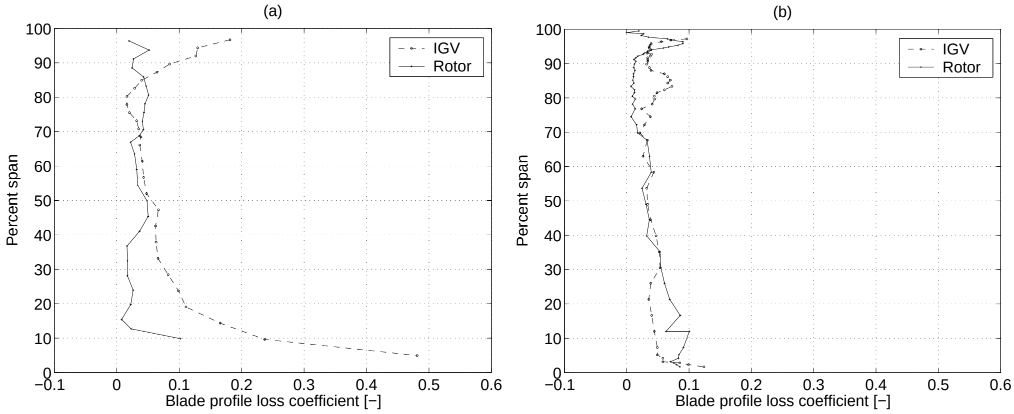

Figure 3.12 Plot of IGV and rotor profile loss coefficient vs percent span from experimental data of the multiple turbine rig (a) and from Gannon (2002) (b).

Cahill (1997) derives an equation to make 3D profile loss coefficients comparable to cascade data. After adaption to the nomenclature of the present dissertation this equation reads

$$\zeta_{3D} = \zeta_{2D} \left[1 + \frac{\gamma - 1}{2} \frac{(\omega r_2)^2}{\gamma R T_{t1}} \left(1 - (r_1/r_2)^2 \right) \right]^{\frac{\gamma}{\gamma-1}} \tag{3.7}$$

where r_1 and r_2 are the distances between a particular streamline and the axis of rotation at the inlet and the exit of the blade row. As the radial component of the flow is small in the experimental results discussed here, the ratio r_1/r_2 is close to unity and the difference between ζ_{3D} and ζ_{2D} is very small and can be neglected[10].

Tip Gap Variation

With the large gap (Geometry A) the tip leakage flow contributes heavily to the overall volume flow (Fig. 3.13); the axial velocity near the tip is significantly increased and the total-to-total efficiency deteriorates from 88 % to 85 %. Note that these experiments have been performed with an increased rotor blade stagger angle of 2 degrees. The rotor blade stagger angle had been increased so that the design point as it is indicated in Figure 3.8 could be reached.

3.3 Summary and Conclusions

In this chapter experimental work on the two solar chimney turbine rigs of the University of Stellenbosch has been presented. Data obtained with the single turbine rig has been analyzed, the design of the turbine and the experimental setup

---

[10] The maximum relative difference is found at 47 % span in the horizontal axis rotor loss coefficient where ζ_{2D} is only 0.05 % bigger than ζ_{3D}.

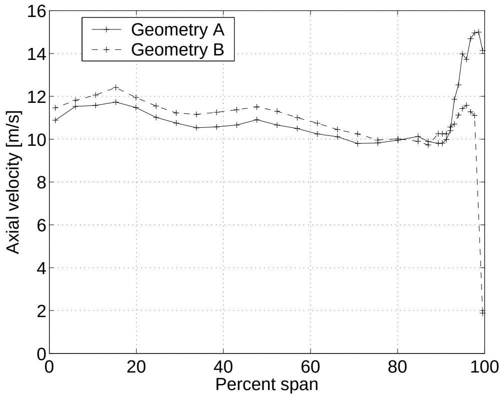

Figure 3.13 Measured profiles of axial velocity at the rotor exit for various rotor tip gap geometries.

for the multiple turbine rig has been discussed and the experimental results have been presented.

From the analysis of the single turbine rig data it has been found that the discrepancy between the experimental results of Gannon (2002) and the predictions from the Soderberg model are most likely due to an offset in the volume flow readings. The experimental results from the multiple turbine rig show that the turbine on that rig runs relatively close to the design intent and with an efficiency close to but slightly higher than the one predicted with the Soderberg model. The relatively simple method, which was used to design this turbine, proves to be adequate for an initial design.

Chapter 4

CFD Analysis of Turbine Models

Over the last decades computational fluid dynamics (CFD) has evolved immensely and today many Navier-Stokes solvers are available. Some of them are capable of solving unsteady three-dimensional multistage turbine flow with leakage and cavity flow included. The primary gas path flow in particular is predicted reasonably well. There are, however, still many areas of ongoing research, for example the modelling of turbulence, transition and secondary flow.

In the design and analysis of gas turbines CFD is used extensively and many publications can be found; e.g. Rosic *et al.* (2006) point out the importance of shroud leakage modelling in turbine flow computations. Praisner and Clark (2007) and Praisner *et al.* (2007) discuss the prediction of transition. Pullan (2006) looks at secondary flows and loss caused by blade row interaction in a turbine stage. Also in other turbine applications CFD becomes increasingly important; e.g. Thakker and Hourigan (2005) use CFD to analyze an impulse turbine for wave energy power conversion and Sezer-Uzol and Long (2006) present a time-accurate three

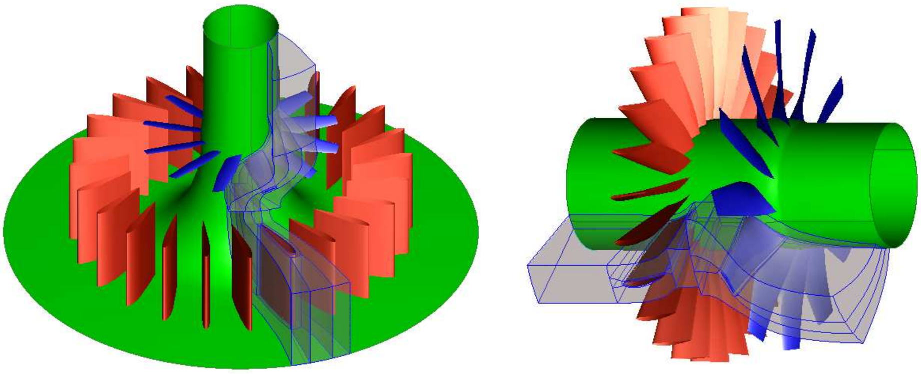

Figure 4.1 Computational domain for the single turbine model (left) and the multiple turbine model.

dimensional simulation of the flow field around a horizontal axis wind turbine rotor.

The role of this tool in context with solar chimney turbines is explored in this chapter. Not much has been published in this research area; Gannon and Von Backström (2002) used the Surface Vortex Method to design the blades of a single horizontal axis model turbine. Kirstein and Von Backström (2006) present a CFD investigation of the inlet guide vanes and the horizontal-to-vertical transition section of a single vertical axis turbine model. They validate their results with experimental data and give a prediction for the full scale plant.

The scope of the present investigation is to do a first evaluation of a commercial CFD package as a tool in context with solar chimney turbines. 3D simulations of both the single vertical axis and the multiple horizontal axis turbine models are presented, and the results are compared to experimental data. The results are also compared to standard turbine correlations to see if they are applicable to this type of turbine.

4.1 Tools

The CFD package FINE/Turbo 7.4-1 of NUMECA has been used to set up and run the simulations on a 1.5 GHz Pentium M processor with 1.5 GB of RAM. FINE/Turbo consists of the grid generator IGG/AutoGrid, the 3D flow solver EURANUS and the post processing tool CFView. Structured grids are used by this package and preconditioning and multigrid acceleration are implemented. This software package has been chosen mainly for its excellent turbomachinery grid generation capabilities, which made it possible to generate high quality grids even for the rotor row, where the blades are highly twisted.

4.2 Method

4.2.1 The Computational Grids

The computational domains for the two turbines are shown in Figure 4.1. Figure 4.2 shows the block boundaries at the shroud of the multiple horizontal axis turbine model geometry. A skin topology was chosen for both blade rows, i.e. each blade is surrounded by an O-mesh block, the skin block, and four H-mesh blocks, which connect the skin block to the periodic boundaries as well as the inlet and outlet boundaries of the blade row. Additional H-blocks extend the flow domain to the upstream and downstream boundaries. The meshes around the trailing and the leading edge of the rotor blade are shown in Figure 4.2. In the rotor blade rows fully non-matching periodic boundaries were used. This makes meshing much easier, particularly for blades with high stagger angles. Shroud leakage flow was not modelled. The grid for the single vertical axis model turbine was set up in a similar fashion.

While the hubs of both model turbines end immediately downstream of the rotor trailing edges (see Fig 3.5), for the simulation the hubs are extended to the outlet boundary. The diffuser after the single turbine is not represented in the computational domain, i.e. a straight shroud is assumed downstream of the turbine in both cases.

4.2.2 Flow Modelling

Various flow modelling approaches have been employed. The results presented in this chapter are from steady state simulations using the one-equation Spalart-Allmaras turbulence model and the transition model of Abu-Ghannam and Shaw on all blade rows. The impact of using another turbulence model and assuming fully laminar or fully turbulent flow is discussed in Appendix E (pp. 104).

4.2.3 Convergence

Convergence on the finest multigrid level is usually achieved after 200 iterations; residuals have diminished by more than 5 orders of magnitude, the mass flow

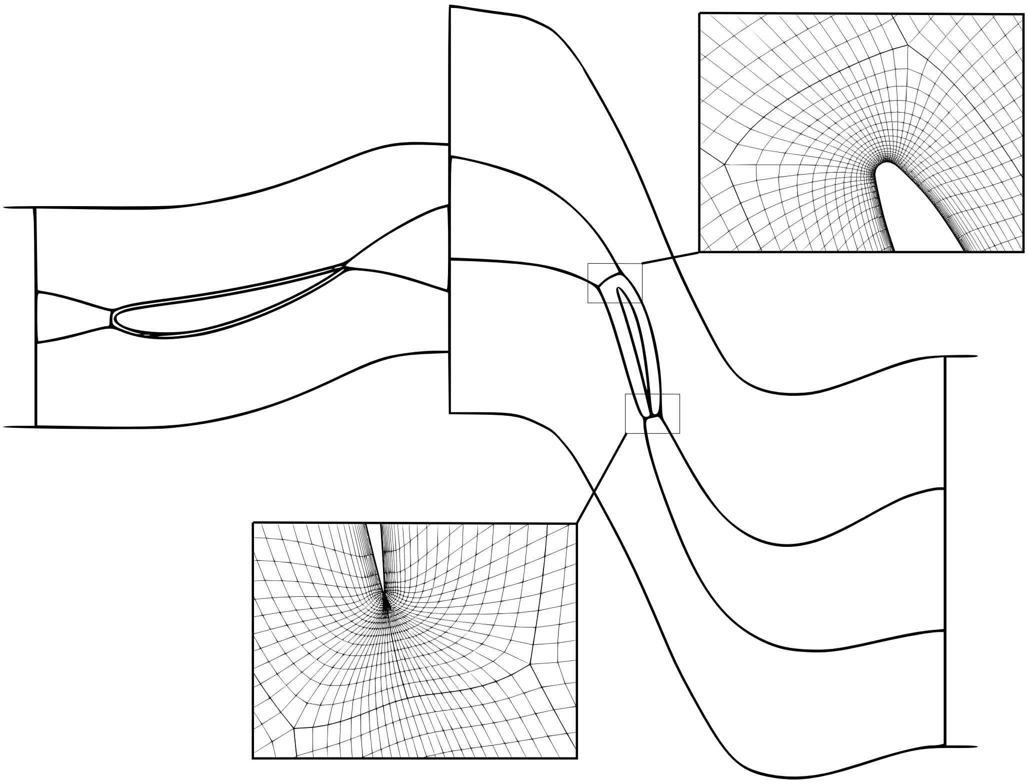

Figure 4.2 Schematic of mesh block boundaries and a typical computational mesh around the rotor leading and trailing edge at the tip of the multiple horizontal axis turbine model geometry.

error is smaller than 0.1 % and the torque, axial thrust and efficiency values have also converged.

4.2.4 Boundary Conditions

For the multiple turbine model the boundary conditions are taken from the experimental results presented in Chapter 3 and are summarized in Table 4.1.

Table 4.1 List of boundary conditions for the CFD analysis of the multiple turbine model.

Inlet total temperature; K	300
Inlet total pressure; Pa	100 000
Exit static pressure; Pa	99 720
Inlet flow angle; °	0
Inlet turbulence viscosity; m^2/s	0.0001
Blade speed at mean radius; m/s	33.74

For the single vertical axis turbine model the experimental results are taken from the dissertation of Gannon (2002). Boundary conditions are summarized in Table 4.2.

Table 4.2 List of boundary conditions for the CFD analysis of the single vertical axis turbine.

Inlet total temperature; K	300
Inlet total pressure; Pa	101 325
Exit static pressure; Pa	100 977
Inlet flow angle; °	0
Inlet turbulence viscosity; m^2/s	0.0001
Blade speed at mean radius; m/s	33.74

4.2.5 Post Processing

The CFD results were evaluated with CFView, which is the flow visualization tool for FINE/Turbo. The grid lines used for the profile data extraction are indicated in Figure 4.3

4.3 Results

For the multiple turbine configuration the volume flow obtained from the CFD is 2 % higher than found from the Venturi readings in the experiment. As mentioned in Chapter 3 on page 42 the profile results even give a 2.8 to 2.9 % lower volume flow. Hence, the axial velocity components, C_{x2} and C_{x3}, from the CFD results are slightly higher than the ones from the experiment (Fig. 4.4). The predicted tangential velocity component at rotor inlet, C_{t2}, compares well to the experiment. The flow deflection in the rotor is under predicted, which leads to a higher exit swirl and a low torque. The radial velocity components of CFD and experiment match well.

For the single turbine configuration the volume flow obtained from the CFD is about 11 % higher than the tabulated experimental results. As discussed in Section 3.1, this could be due to the fact that the volume flow readings taken from the anemometer in the experiment of Gannon (2002) were too low. As with the multiple turbine rotor the deflection in the rotor is under predicted. An additional comparison of one case where the rotor has been removed from the single turbine rig, as presented by Kirstein (2004), shows good agreement between the CFD and the experiment. More detail on this comparison is given in Appendix F (pp. 108).

The profile loss coefficients from the CFD results were also evaluated using Equation 2.27. Most of them compare reasonably well with the experimental results (Fig. 4.5) and with values obtained with the Soderberg loss model. Only the loss coefficient of the IGVs of the single turbine rig is unrealistically low. This is probably due to the very low total pressure drop over that blade row. Even a numerical error in total pressure of a few Pascal changes the resulting loss coefficient immensely (see also Kirstein (2004)).

In the transition model implemented in FINE/Turbo a parameter called intermittency has been introduced, which has a value of zero at locations with fully laminar flow and a value of one at locations with fully turbulent flow. According to this model the flow stays laminar over almost the entire chord of both the pressure and suction side of all blade rows. See Figure 4.6 for a contour plot of intermittency on the rotor blades. As the full size turbines are much bigger, however, the flow would be turbulent over almost the entire chord of their blades.

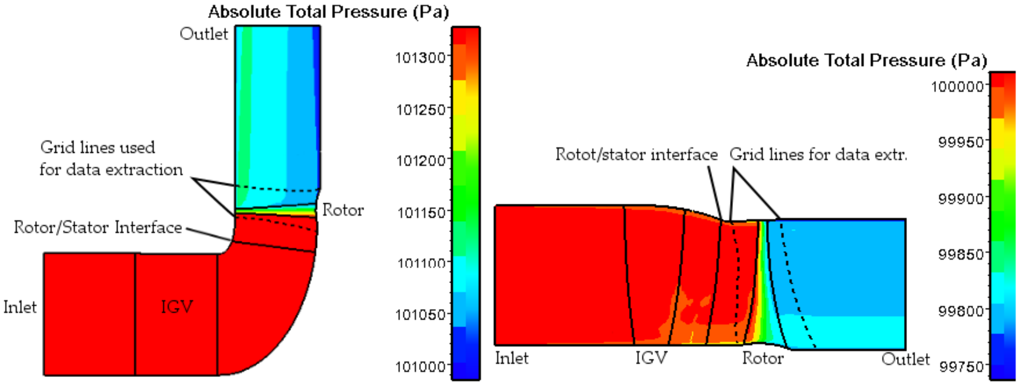

Figure 4.3 Meridional view of flow domains of the multiple turbine (left) and the single turbine geometry, showing a contour plot of absolute total pressure and indicating the grid lines used for the profile data extraction.

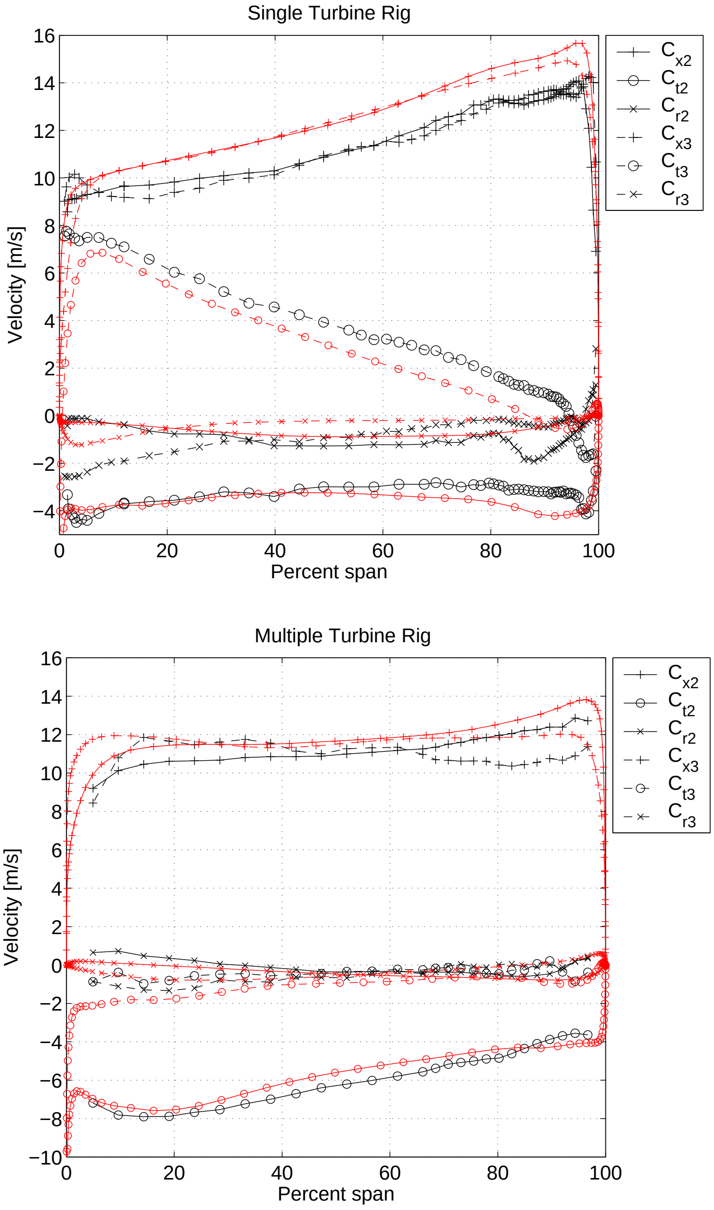

Figure 4.4 Velocity components from CFD simulations (red/small markers) on the single and multiple turbine model compared to experimental data (black/big markers).

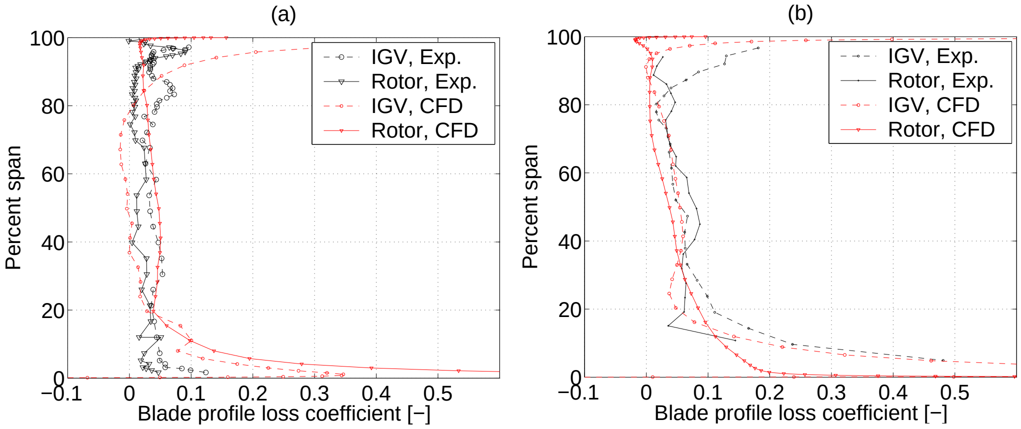

Figure 4.5 Plot of IGV and rotor profile loss coefficient vs percent span from CFD simulations on (a) the single and (b) the multiple turbine model.

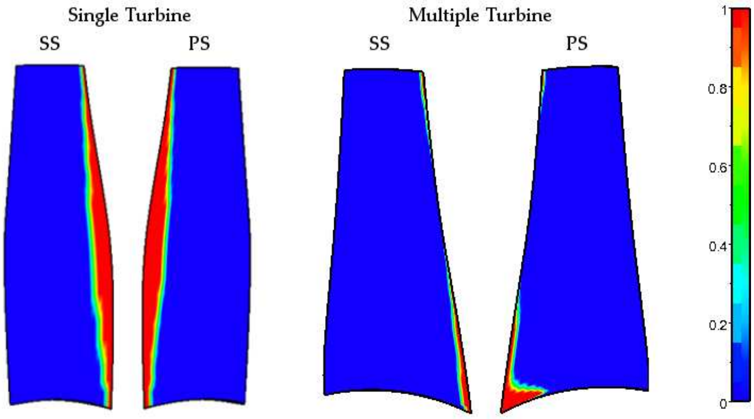

Figure 4.6 Contour plot of intermittency on the turbine rotor blades.

Another possible reason for the discrepancies mentioned in this section is that a steady state simulation has been run; the flow in a real turbine is highly unsteady. For example Pullan (2006) compares results from steady state and unsteady calculations and finds that the steady state calculation under predicts the losses by 10 %. Also, the transition model used here is not able to predict the real situation accurately. Praisner and Clark (2007) present a new transition model and compare it to the one of Abu-Ghannam and Shaw, which was used here. They find that their model gives more accurate predictions for most test cases. It also has to be kept in mind that a number of geometrical features were not present in the CFD model, e.g. the rotor tip gap and the sudden expansion after the turbine rotor.

4.4 Conclusions

A first evaluation of a commercial CFD package as a tool in context with solar chimney turbines has been presented in this chapter. The CFD results have been compared to the experimental results of the two turbine rigs presented in the previous chapter. The agreement is reasonably good for both configurations. The CFD results also confirm the applicability of the Soderberg loss model for solar chimney turbines. CFD will be an important tool for full-scale turbine performance predictions and detailed aerodynamic optimization.

Chapter 5

Performance of the PCU

The losses occurring in the power conversion unit (PCU) of a solar chimney power plant can be divided into three groups, namely aerodynamic, mechanical and electrical losses. While the first group is treated in detail and an analytical model is introduced for each loss component, the latter two groups are summarized as drive train losses.

List of Losses in a Solar Chimney PCU

- Aerodynamic losses
    - Intake losses
    - Turbine losses
        - Profile loss
        - Secondary loss
        - Trailing edge loss
        - Tip leakage loss
        - Annulus loss
        - Other losses
    - Diffuser losses
    - Mixing losses
    - Horizontal to vertical flow transition losses
    - Losses over struts
- Mechanical losses
    - Gearbox losses
    - Bearing losses
- Electrical losses

- Generator losses
- Losses in power electric converter

5.1 Aerodynamic Losses

5.1.1 Intake Losses

For the multiple horizontal shaft configuration Kolb and Helmrich (1996) propose a rather bulky intake geometry with converging sections and a transition from rectangular to circular and analyze it with CFD[1]. In the present dissertation a circular bellmouth type intake is proposed, because consulting Idelchik (1986) it is found that with a bellmouth, which is much shorter than the geometry proposed by Kolb and Helmrich (1996), lower inlet losses can be expected. Furthermore, a bellmouth provides a more uniform velocity profile leading to a smaller dynamic load on the rotor blades. The cost of this alternative solution is not expected to be higher. Idelchik's data for a wall-mounted bellmouth can be approximated by $\zeta_{BM} = 0.5e^{-14.114(r/d_h)}$ where r is the bellmouth radius and d_h is the hydraulic diameter of the duct (see Fig. 5.1). For this investigation r/d_h is assumed to be 0.12, which gives an inlet loss coefficient of 0.09.

For the multiple vertical shaft configuration the same intake loss model is used, and, even though the geometry would look different, it is assumed to be good enough for a first approximation. For the single vertical shaft configuration no special intake is necessary, and the intake losses are accounted for in the horizontal to vertical transition loss model, which will be presented in Section 5.1.5.

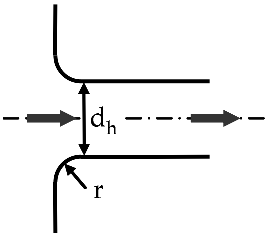

Figure 5.1 Schematic of a wall mounted bellmouth

5.1.2 Turbine Losses

The mathematical model for an axial turbine with inlet guide vanes presented in Chapter 2 is used for all configurations in the investigation presented here. Even

---

[1] They only simulate the actual duct of each turbine. To get more meaningful results they should have extended the grid upstream of the actual inlet. Müller (2002) presents a similar investigation on the same geometry.

though for a single vertical axis turbine the inverted Kaplan concept discussed e.g. by Gannon (2002) would be used, the model for an axial through flow turbine is assumed to be adequate.

5.1.3 Diffusion Losses

There are two areas in the SCPCU where significant diffusion losses can occur; the first is after the turbine rotor(s) where the hub ends, the second is in the actual diffuser. Japikse and Baines (1994) give an overview on how to model a diffuser. Their nomenclature is adopted here; the coefficient of static pressure recovery is defined as:

$$C_p = \frac{p_2 - p_1}{p_{t1} - p_1} \tag{5.1}$$

and the total pressure loss coefficient as:

$$K = \frac{p_{t1} - p_{t2}}{p_{t1} - p_1} \tag{5.2}$$

They assume that the square of the mean velocity across any cross section is equal to the mean square of the velocity distribution and derive the ideal pressure recovery of a diffuser, $C_{p,id}$, as a function of the diffuser area ratio, R_d:

$$C_{p,id} = 1 - {R_d}^{-2} \tag{5.3}$$

The diffuser effectiveness is defined as:

$$\eta_d = C_p / C_{p,id} \tag{5.4}$$

According to Japikse and Baines (1994) common diffuser effectiveness lies between 0.7 and 0.9. A conservative value of 0.7 is assumed in this study.

For the multiple horizontal axis turbine configuration it is assumed that for a small diffuser area ratio, $R_d < 1.3$, the area change is located before the horizontal to vertical transition section. For a higher diffuser area ratio the area change before the horizontal to vertical transition section is set to 1.3 and the remaining area change is assumed to take place in the chimney.

5.1.4 Mixing Losses

With any multiple turbine configuration, losses will be generated where the outflow of the various turbines merge. Idelchik (1986) gives loss coefficients for merging of streams in a converging Y (Fig. 5.2). Obviously the geometry in the SCPCU looks quite different (Fig. 5.3), but due to the lack of more applicable data a loss coefficient is derived from this; for a Y with $\alpha = 15°$ and equal volume flow through the two inlet branches Idelchik gives a loss coefficient of 0.10. This value is employed in the present study.

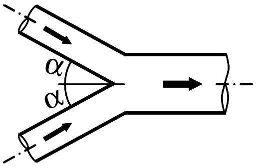

Figure 5.2 Schematic drawing of a converging Y (adapted from Idelchik (1986), Diagram 7-30).

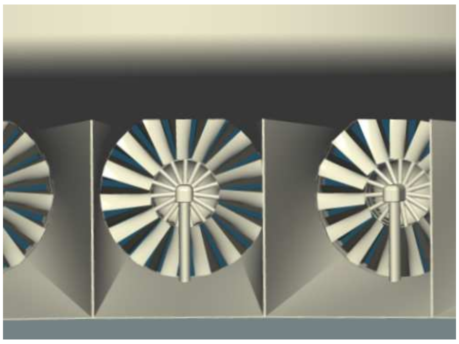

Figure 5.3 CAD model of merging ducts at the exit of multiple turbines.

5.1.5 Horizontal to Vertical Flow Transition Losses

For the single vertical shaft configuration Kirstein and Von Backström (2006) present data for a horizontal to vertical flow transition section designed by Gannon (2002). They investigate various swirl angles. From CFD and for flow with no swirl they give loss coefficients between 0.036 and 0.063 for different inlet heights for a full scale plant. They measured loss coefficients of around 0.03 on a small scale model.

The horizontal to vertical flow transition section could also be modelled as a wall-mounted bell mouth with a facing baffle. Idelchik (1986) gives data for such a component and non-swirling flow for values of h/d_h between 0.1 and 0.8 and r/d_h between 0.2 and 0.5. Taking the geometry from Gannon, which gives an approximate value of $h/d_h = (0.36, 0.44)$ and $r/d_h = 0.056$ and linear inter-/extrapolation from the data of Idelchik loss coefficients of 0.098 and 0.080 are obtained for the two inlet heights.

In Idelchik's case there is no centerpiece in the transition section, however, which would prevent local diffusion and lower the losses (Fig. 5.4). Müller (2002), who works with a geometry for multiple turbines, finds that such a centerpiece can reduce the losses by 43 %. Applying a correction factor of this order to the coefficients derived from Idelchik's data brings them reasonably close to the ones of Kirstein and Von Backström (2006).

Pretorius (2006) compares the annual power output from simulations using

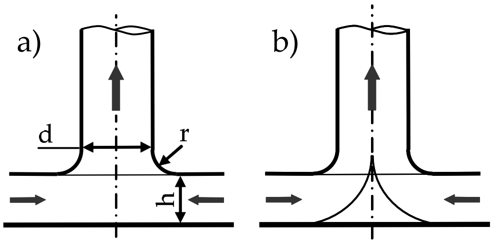

Figure 5.4 Schematic drawing of horizontal to vertical transition section (a) without and (b) with a centerpiece to redirect the flow.

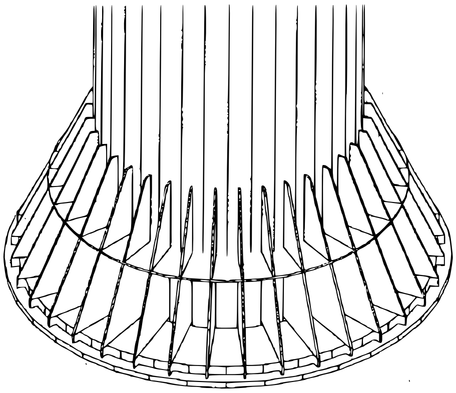

Figure 5.5 Typical representation of the chimney support struts of a 1000 m tall chimney (Goldack, 2004).

a loss coefficient for the horizontal to vertical flow transition section of 0.25 and 0.14. He finds that the higher loss coefficient reduces the annual power output by only 0.4 %. Pretorius and Kröger (2006a) do the same comparison for a different plant configuration and find a reduction of the annual power output of 0.55 %. For the present investigation a loss coefficient of 0.05 is assumed for the horizontal to vertical flow transition section for all configurations.

5.1.6 Losses over the Chimney Support Struts

The struts supporting the chimney should block as little as possible of the chimney inlet passage to keep aerodynamical losses small, but they need to have a certain size to be able to support the chimney. The work of Van Dyk (2004*a*) and pictures in many publications suggest that the chimney can be supported without heavily blocking the inlet passage; the schematic in Figure 5.5, showing rather slender chimney support struts for a 1000 m tall chimney, has been taken from the recent publication of Goldack (2004), for example.

Harte (2007) raised the concern that in order to ensure a safe support of the chimney shell, wider struts might be required, which would block a bigger por-

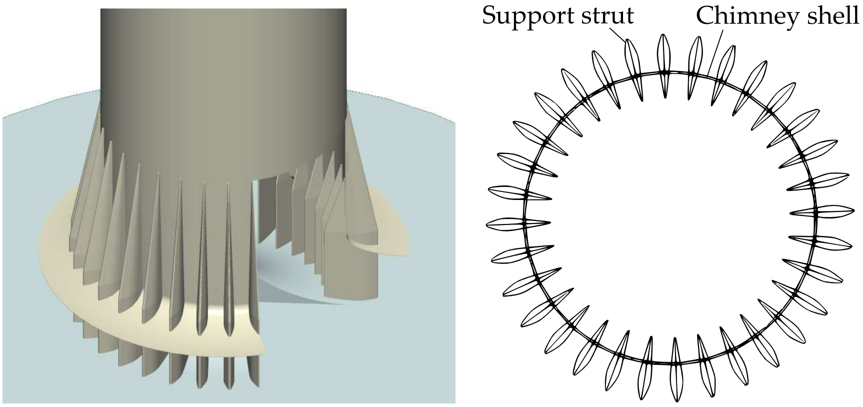

Figure 5.6 Chimney foot with wider support struts; 3D view with a cutout to show the interior of the chimney (left) and top view (as modelled with the software package SolidEdge).

tion of the inlet passage. In Figure 5.6 a chimney foot with wider support struts is shown. The passage between two struts could be mathematically modelled as a converging nozzle. Idelchik (1986) states that, at high Reynolds numbers and for nozzle wall angles within the limits of 10 to 40°, converging nozzles with rectilinear walls give loss coefficients of around 0.05, and that this loss coefficient can be greatly diminished by using curvilinear walls. Assuming that the flow velocity between the struts is similar to the one in the chimney and the loss coefficient of the struts to be 0.05 a loss similar to the one of the horizontal to vertical transition section will result. As this loss is low (see Section 5.3.1 for a comparison of the various losses) and will be similar for all configurations, and as there is a potential to further reduce the loss over the struts by aerodynamically optimizing their shape, in the remainder of this dissertation the loss over the chimney support struts is neglected.

5.1.7 Other Aerodynamic Losses

The friction losses in the straight runs are insignificant compared to the losses due to flow obstructions and components in the PCU and are neglected. The same applies to losses induced by the various struts, which can be shaped in a streamlined manner to keep the losses low. Windage losses are also neglected.

5.2 Drive Train Losses

In the present report the drive train includes all components necessary to convert the mechanical power delivered by the turbine rotor to electrical power ready for grid feeding, i.e. gearbox, electrical generator, power electronics and grid interface systems. For the multiple horizontal axis turbine configuration drive trains similar to the ones of large wind turbines can be used.

As part of the U.S. Department of Energy's Wind Energy Program two reports on drive train design studies have been released: Poore and Lettenmaier (2003) present technical descriptions and economical analysis of several preliminary variable speed 1.5-MW wind turbine drive train designs. Effects of scaling to 3-MW or 750-kW plants are also discussed using scaling laws. Bywaters *et al.* (2004) present a similar study but instead of using scaling laws they make a detailed design for each configuration. While the first recommend a configuration with a single stage gearbox and a single permanent magnet generator for further investigation, the latter give preference to a direct drive permanent magnet generator (DDPM); although the primary evaluation metrics, which are first cost and cost of electricity, are similar for both configurations, Bywaters *et al.* (2004) see a higher potential for further cost reduction for the DDPM taking industry and market trends into consideration. They mention, for example, the steady decline of cost of magnets and power electronics. Following this line of reasoning the DDPM has been chosen for the present study. Also, such a drive train allows for variable speed operation, which is, as discussed in Section 1.4.1 (p. 14), well suited for a SCPCU.

Bywaters *et al.* (2004) give efficiencies of between 90.1 and 92.4 % for loads above 25 % for a DDPM drive train of 1.5-MW wind turbines. The efficiency only drops off at very low loads (80.8 % efficiency at 6 % load). For the same kind of drive train Poore and Lettenmaier (2003) give an almost constant efficiency of about 93 % only dropping off at extremely low speeds. Following the more recent publication of Bywaters *et al.* (2004) a constant drive train efficiency of 91 % is assumed for all configurations in this investigation.

5.3 Results

5.3.1 Impact of Various Loss Components

Using the above loss models the impact of each component on the overall performance of the plant can be assessed. In this section it is assumed that the plant described in Section 1.4.1 on page 14 is operating at peak power, that a multiple horizontal axis turbine configuration is used and that there is no change in flow area from the turbine exit to the chimney inlet. Other configurations will be assessed in later sections. A sample calculation is presented in Section D.3 (pp. 101).

In order to make all the losses comparable the pressure drops over the various components are translated into an efficiency. For the inlet, the mixing and the horizontal to vertical transition loss this is done with the following equation: $\eta_c = (\Delta p_{PCU} - \Delta p_c)/\Delta p_{PCU}$, where Δp_{PCU} is the pressure drop available across the whole PCU and Δp_c is the pressure drop over a specific component. For the exit losses the same equation is used but Δp_c is the exit dynamic head. The evaluation of the drive train and the turbine efficiency is described in the sections 5.2 (p. 58) and 5.1.2 (p. 54).

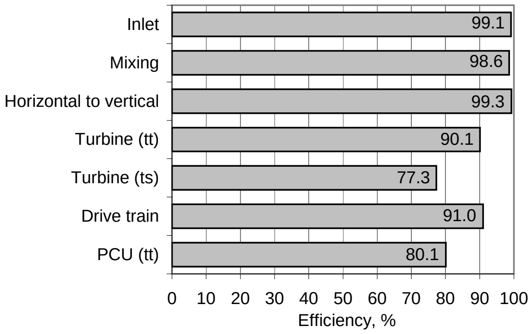

Figure 5.7 Plot of efficiencies of the various components of the PCU for peak power conditions.

The results are presented in Figure 5.7. The inlet, the mixing and the horizontal to vertical transition section have a very small impact on the overall losses, while the exit losses are very important. The overall efficiency of the PCU disregarding the exit losses is 80.1 %; hence, very close to the 80 % chosen by Pretorius and Kröger (2006b) and others before them. The total-to-total turbine efficiency prediction is similar to the values mentioned by Von Backström and Gannon (2004).

5.3.2 Performance of Various Configurations

From the results presented in the previous section it can be predicted that the differences in performance of the various configurations will be small; velocities are similar for all of them since the areas are similar, and only loss components with a low impact on the overall performance vary, e.g. mixing losses are obviously non-existent in a single turbine configuration. This reflects well in Figure 5.8 where the power output of different configurations at various operating conditions is shown; at all operating conditions the power is slightly lower for the multiple turbine configurations. As a consequence, the single turbine configuration generates the highest yearly energy yield (738.5 GWh). Both multiple turbine configurations generate 721.1 GWh, which is 97.6 % of the above value.

As predicted in Section 1.4.1 (pp. 14), the optimal turbine parameters and the PCU efficiency remain close to constant over the entire operating range. For the multiple horizontal axis turbine configuration, for example, the optimal parameters are as follows:

- Flow coefficient $\Phi = 0.321$ (± 0.005)
- Load coefficient $\Psi = 0.322$ (± 0.007)
- Degree of reaction $R_{n,a} = 0.771$
- PCU total-to-total efficiency $\eta_{PCU} = 80.0\,\%$ (± 0.2)

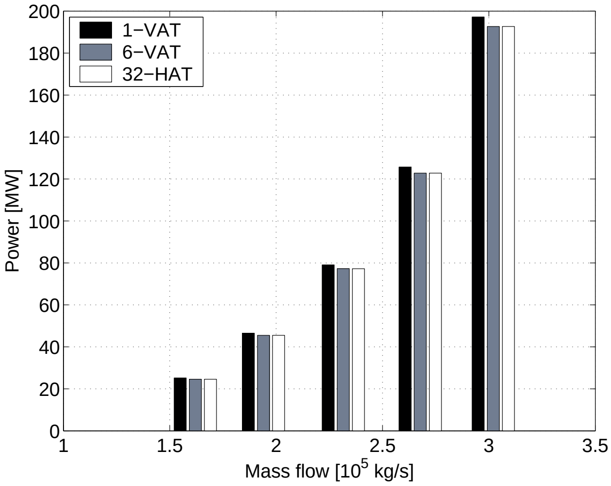

Figure 5.8 Power output of different configurations at various operating conditions.

An important drawback of the configurations with few turbines is the high torque at each turbine; the single vertical turbine operates with a peak torque of 474.3 MNm, each of the six multiple vertical axis turbines at 31.3 MNm and each of the 32 multiple horizontal axis turbines at 2.63 MNm. Thanks to their higher rotational speeds also the overall torque of the multiple turbine configurations is lower (187.7 MNm for the vertical and 84.0 MNm for the horizontal axis configuration), which reduces the cost, especially for the generators, where the cost is proportional to the torque.

5.3.3 Nozzle or Diffuser

In the above investigation it has been assumed that the turbine area is equal to the chimney area, i.e. the diffuser area ratio equals one. In this section the question is addressed whether it is favourable to have a nozzle or a diffuser downstream of the turbines.

Assuming that the chimney diameter is given, there remain two ways to change the diffuser area ratio and get a nozzle or a diffuser after the turbines: one can either change the number of turbines or their individual size. No matter which of these two options we choose, or whether we opt for a combination of the two, the PCU efficiency deteriorates with increasing diffuser area ratio, because the turbine through flow velocity increases and so does the relative velocity, with the square of which the blade losses increase (Fig. 5.9) and because the diffuser losses increase. The same figure shows that reducing the diffuser area ratio below unity to get a nozzle after the turbine increases the efficiency only slightly; e.g. doubling the turbine area gives an efficiency benefit of 1.5 percentage points.

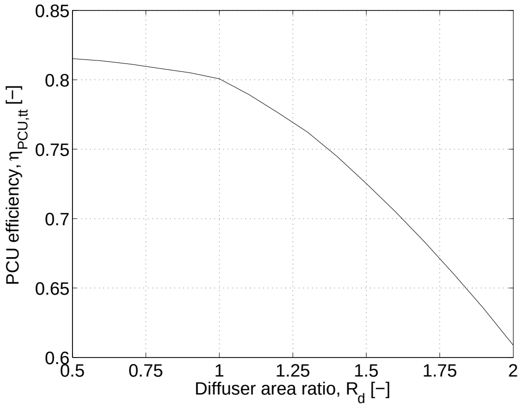

Figure 5.9 PCU total-to-total efficiency vs. diffuser area ratio for multiple horizontal turbine configuration

5.4 Summary and Conclusions

In this chapter, a performance model for the SCPCU has been developed; loss models have been defined for all components of the PCU. For the turbine the model presented in Chapter 2 has been integrated. The performance model has been implemented in Matlab. A comparison of three configurations from an efficiency and energy yield point of view is made, and the impact of the various losses on the overall performance is highlighted.

The results show that, with designing the flow passages in an appropriate manner, the aerodynamic losses over the various components of the PCU can be kept low. The assumption made by many other researchers that total-to-total efficiency of the PCU is 80 % has been confirmed. The single vertical axis turbine has a slight advantage with regards to efficiency and energy yield because certain loss mechanisms are not present. But its peak output torque is tremendous, making its drive train costly and its feasibility questionable. Further, it has been shown that the PCU efficiency deteriorates significantly with increasing diffuser area ratio but improves only slightly with reducing the diffuser area ratio below unity. To get a clearer indication on which configuration is to be preferred, a modified version of the performance model presented here will be linked to a cost model in Chapter 6.

Chapter

6

Minimization of COE

To minimize the cost of electricity (COE) a detailed cost model for the power conversion unit (PCU) is introduced and linked to the performance models presented earlier. The cost model is a refined version of the one presented by Fluri *et al.* (2006). The minimal cost of electricity is evaluated for the various layouts and configurations of the PCU and preliminary design results for the various components at the optimum are presented[1].

6.1 Design and Cost Model of the PCU

6.1.1 Turbine Rotor Blades

Gannon (2002) designed turbine rotor blades for a single turbine configuration. The focus of his work lies on the aerodynamic optimization and his final blade geometry is not optimized from a structural point of view. For the baseline design presented here, Gannon's blade geometry is used nevertheless.

Griffin (2001) presents a scaling study of E-glass/epoxy laminate wind turbine blades with a length of 40 to 60 m. He assumes a mature production cost of 10.45 $/kg blade mass and points out that it takes about 100 pieces of a component to reach a mature production process. Production cost of the first 100 blades is adjusted according to Table 6.1. With a single turbine configuration a mature production process is only reached after the ninth plant has been built assuming 12 blades per turbine. With a 32-turbine configuration for one single plant 384 rotor blades are required.

A blade mass of 11,783 kg is quoted for a 45 m long blade[2]. Because of the longer chord of the solar chimney turbine blade—the maximum chord of Gannon's rotor blade is 14 m compared to 5 m for a 45 m long wind turbine blade

---

[1] The conversion rate between the US Dollar and the Euro was assumed to be US$ 1.2 = €1.0 (March 2006).

[2] 46.6 m minus assumed hub radius of 1.6 m (Griffin, 2001)

Table 6.1 Cost multipliers for non-mature production (Griffin, 2001)

Blade quantity	Multiplier on production cost
1-20	4.00
21-60	1.50
61-100	1.15

Table 6.2 Dimensions, mass and cost of turbine blades used as reference in the cost model.

		Wind turbine (Griffin, 2001)	Solar chimney (Gannon, 2002)
Blade length	m	45	39
Blade chord	m	5	14
Blade mass	kg	11783	32992
Number of rotor blades	-	3	12
Specific blade cost	$/kg	10.45	10.45
Blade cost	k$/pc.	123.1	246.3

(Smith, 2001)—the mass of Griffin's 45 meter long blade is multiplied by 2.8 to get an estimate for the blade mass of the large solar chimney single turbine configuration blade. According to Griffin (2001) the average mass values for wind turbine blades with lengths between 23 m and 40 m scale approximately as $R^{2.4}$, where R represents the turbine tip radius. This relation and the aforementioned values for the large single turbine configuration blades are used here to estimate the mass of the smaller sized blades required by the multiple turbine configurations, but the length of the blade L is used instead of the tip radius R. The turbine blades described above are compared in Table 6.2.

6.1.2 Pitch Bearings

In their Appendix C, Malcolm and Hansen (2002) present wind turbine pitch bearing data for rotor diameters of 46.6 m to 120 m. They give a curve fit through this data to estimate the cost. This curve fit is used here, and the equation is repeated for convenience:

$$\$/bearing = 0.0454 \times D^{2.98} \tag{6.1}$$

As suggested by them, this cost is doubled to account for the rest of the pitch system (motor, speed reducer, controller, etc.).

6.1.3 Rotor Hub

Following the wind turbine notation the rotor hub is the part connecting the blade root to the main shaft. In the work of Malcolm and Hansen (2002), where large three-bladed wind turbines are investigated, the ratio of the mass of the hub to the total blade mass per rotor varies between 0.93 and 1.30. In the case of the solar chimney the hub-to-tip ratio and therefore the hub itself will be much bigger, hence, we assume that the mass of the hub is double that of all blades attached to it. The cost of the hub is set to 4.25 $/kg (Malcolm and Hansen, 2002).

6.1.4 Rotor Shaft

The rotor shaft is assumed to be a hollow cylinder. The flanged end necessary to bolt the shaft to the hub is neglected. The length is fixed at 0.05×(rotor diameter) and the wall thickness is fixed at 0.003×(rotor diameter). Following Malcolm and Hansen (2002) the shaft material is assumed to be high-strength steel with a characteristic yield of 828 MPa and a cost of 7.00 $/kg. The shaft diameter is then determined using the equation for torque on a thinwall shaft according to Beitz and Grote (2001) and a safety factor of 8.0. Mass and cost of the shaft can now be calculated.

6.1.5 Rotor Bearings

Malcolm and Hansen (2002) give the following equations for the main bearing and housing mass:

$$\textit{Bearing mass}\,[kg] = 2.613E-5\times(\textit{Shaft OD}\,[mm])^{2.77} \tag{6.2}$$

$$\textit{Housing mass}\,[kg] = 6.744E-5\times(\textit{Shaft OD}\,[mm])^{2.64} \tag{6.3}$$

They also indicate a cost for the main bearing of 17.60 $/kg. In their work the second bearing is included in the gearbox assembly. Here a factor of 1.5 is added to the above model to account for the second bearing.

6.1.6 Inlet Guide Vanes

The cost of the inlet guide vanes is assessed in the same way as for the rotor blades (see Section 6.1.1). The rest of the IGV cost is assumed to be included in the cost of the vanes. For the 1-VAT configuration it is assumed that the chimney supports act as IGVs and their cost is assumed to be included in the chimney cost.

6.1.7 Generator / Power Electrical Converter

Poore and Lettenmaier (2003) give a cost for a 1.5 MW direct drive permanent magnet generator of $ 365 589. Its nominal torque can be extracted from their data and is 0.7 MNm. This information is used together with the rule of thumb for electric generators, which says that the volume of a generator scales linearly with torque (Voutilainen, 2004). It is further assumed that the aspect ratio of the generator remains the same ($d/l = 4.0$) and that its cost is proportional to its volume.

The power electrical converter adjusts the generator current to the grid current. With a permanent magnet generator this is typically done by first converting the alternating current coming from the generator to direct current and then back to alternating current. The cost for the power electronics is rated 35 $/kW (Poore and Lettenmaier, 2003).

6.1.8 Control System

Also the equation to model the cost of the control system is taken from the work of Malcolm and Hansen (2002) and reiterated here for convenience:

$$\$ = 9500 + 10 \times D$$

It could be argued that the control system of a solar chimney should be cheaper than the one of a wind turbine, because there is neither need for yaw control nor for fast response to gusts. But this potential cost decrease is neglected at this stage.

6.1.9 Turbine Casing and Duct

For the vertical axis turbine configurations it is assumed that the cost for the outer casing of the turbine as well as for the inlet and outlet duct are included in the cost of the chimney and the central flow guiding structure.

For a horizontal axis turbine configuration a special structure has to be built to warrant an even flow profile at the inlet of each turbine and to connect each turbine outlet to the chimney inlet. In this cost model this structure is assumed to consist of circular ducts with the same diameter as the outer diameter of the turbines. The minimum length of these ducts is set to a quarter of the chimney diameter to accommodate the horizontal-to-vertical flow transition section. Note that as the number of turbines increases they have to be located further away from the chimney for them to fit in one row. The minimal distance between the ducts is set to 1 m. Having a circular duct is only realistic close to the turbines, because closer to the chimney the various ducts would intersect and would have to blend into the aforementioned transition section as shown in Figs. 5.6 and 5.3, but this is neglected here. The material for the ducts are 1.8 mm thick ZincAlum plates with a cost of 33.33 $/m^2. To account for the support of these ducts 20 % is added to their cost.

6.1.10 Support Structure

For the support structure of the PCU a thin wall steel tube design similar to that of the towers found in wind turbine power plants is suggested. Steel with a characteristic yield of 300 MPa and a cost of 1.50 $/kg is used. The aspect ratio of the support (height/diameter) is set to 9, the wall thickness to 20 mm and the loads resulting from the torque on the generator and the weight of the PCU have been checked for certain cases.

Table 6.3 Balance of station cost of large wind turbine power plants (Malcolm and Hansen, 2002).

Rating		MW	0.75	1.50	3.00	5.00
Rotor diameter		m	50	70	99	128
Transportation	$\$ = 17296e^{0.0146\times D_t}$	$	26 586	51 004	253 410	1 312 150
Foundations	$\$ = 1749.6e^{0.051\times D_t}$	$	34 919	48513	76765	108 094
Roads and civil works	$\$ = 15929e^{0.0218\times D_t}$	$	44 896	78 931	136 359	255 325
Assembly and installation	$\$ = 6492.6e^{0.0282\times D_t}$	$	24 374	50 713	112 714	224 790
El. interfaces/connections	83.5 $/kW	$	71 304	126 552	224 196	431 500
Permits and engineering	24.5 $/kW	$	15 790	32698	69868	126 385
Balance of station		$	217 869	388411	873 312	2 458 244

6.1.11 Central structure

To redirect the flow smoothly into the chimney a central structure has been suggested by Schlaich (1995) and others. To keep the cost model simple this component is modelled as a cone with a height of 0.6 times the diameter of the chimney and a radius equal to that of the chimney. The cost of the central structure is found by considering 0.9 mm ZincAlum plates as the material of choice at a cost of 17 $\$/\text{m}^2$ and adding 20 % for the support structure.

6.1.12 Balance of Station

The balance of station (BOS) cost includes cost for foundations, transportation, roads and civil works, assembly and installation, electrical interfaces and connections and permits and engineering. It is dependent on the site of the plant as well as the location of the suppliers. The cost category 'electrical interfaces and connections' includes the cost of a pad mount transformer for each turbine, of a medium voltage collection system connecting the transformers to the substation, of equipment to improve the power quality and of the substation connecting the power plant to the transmission system.

To get an estimate for the BOS-cost for the SCPCU, a comparison to the work of Malcolm and Hansen (2002) is made, who look at a 50 MW wind farm located in the Midwest of the USA. Curves have been fitted through their data (Tab. 6.3). These approximations are used in the cost model for the SCPCU presented here. The number of blade rows and blades is larger in a SCPCU compared to a wind turbine; the foundation cost is multiplied by the number of blade rows, and transport as well as assembly and installation cost are assumed to be proportional to the number of blades. Permits and engineering costs are neglected.

6.2 Optimization Tool

All the modules for the tool developed in this dissertation, as shown in Figure 1.3 (p. 12), are now in place and can be linked to each other. The performance model for the PCU was presented in the previous chapter. The cost models for the PCU have been presented in the earlier sections of this chapter, and the procedure for the evaluation of the cost of electricity is described in Section 1.4.3 on page 16. Hence, the configuration and layout of the PCU with minimal COE can now be determined. The operating conditions are the same as presented in Section 1.4.1; the actual data is summarized in Table G.1 on page 110. For the cost of the collector, the cost of the chimney structure and the operating and maintenance cost the model of Bernardes (2004), as described in Section 1.4.2 on page 15, is used. Hence, the chimney cost and the collector cost are assumed to be 272 M€ and 379 M€, respectively.

6.3 Results

6.3.1 Optimal Number of Turbines and Optimal PCU Layout

In Figure 6.1 PCU cost and COE are plotted against number of turbines for a single rotor turbine layout with IGVs, and the corresponding results are summarized in Table 6.4. The cost of electricity decreases with increasing number of turbines, mainly due to two reasons: an improved efficiency of the PCU, which leads to a

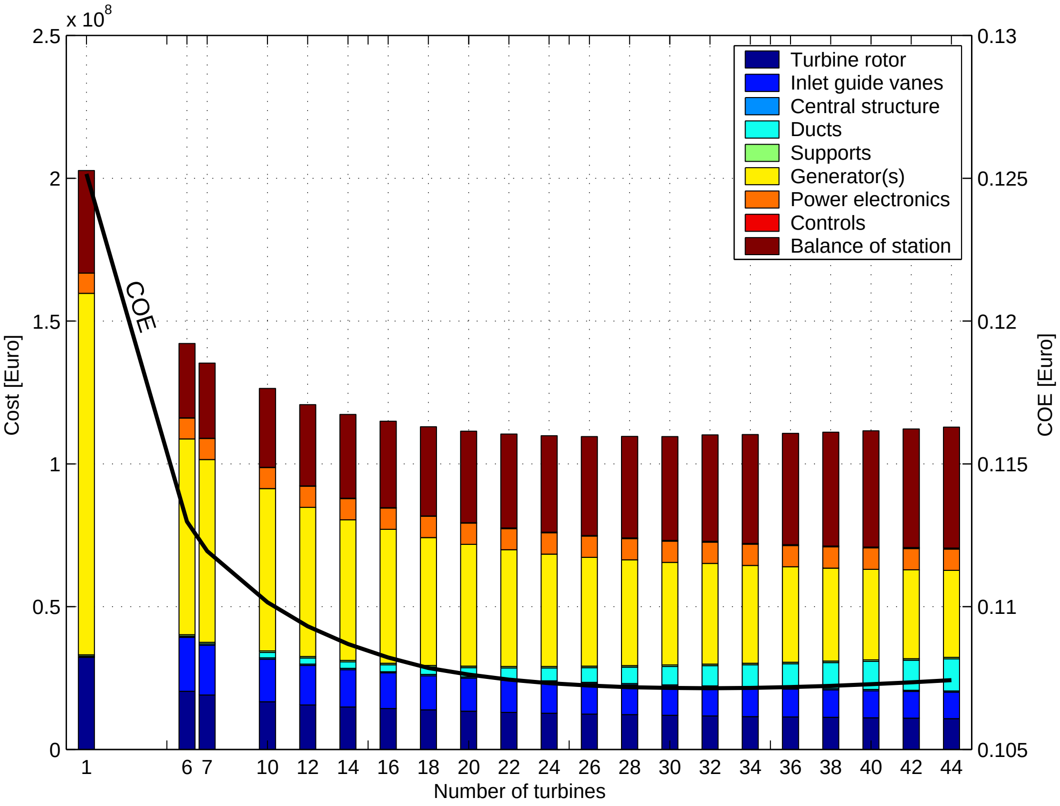

Figure 6.1 PCU cost and COE vs. number of turbines.

Table 6.4 Cost and performance results for various numbers of single rotor turbines with IGVs.

Number of turbines	**1**	**6**	**7**	**10**	**20**	**32**
Turbine rotor, M€	32.24	20.39	19.09	16.73	13.38	11.75
Inlet guide vanes, M€	0.00	18.83	17.44	14.90	11.58	10.08
Central structure, M€	0.44	0.44	0.44	0.44	0.44	0.44
Ducts, M€	0.00	0.00	0.00	1.93	3.23	7.08
Supports, M€	0.44	0.53	0.53	0.53	0.53	0.53
Generators, M€	126.58	68.53	64.02	56.80	42.66	35.28
Power electronics, M€	7.11	7.35	7.36	7.40	7.44	7.46
Controls, M€	0.01	0.05	0.06	0.08	0.16	0.26
Transportation, M€	2.11	3.76	4.07	5.04	8.09	11.59
Foundations, M€	9.55	0.66	0.59	0.49	0.43	0.45
Roads & civil works, M€	0.42	0.38	0.39	0.44	0.62	0.83
Assembly & inst., M€	6.85	3.72	3.74	4.01	5.16	6.62
El. Int./connections, M€	16.97	17.54	17.55	17.65	17.74	17.79
Balance of station, M€	35.89	26.05	26.35	27.62	32.04	37.28
Initial capital cost, M€	202.72	142.17	135.29	126.44	111.46	110.16
Turbine diameter, m	158.70	71.27	65.98	55.21	39.04	30.86
Blade length, m	47.61	21.38	19.79	16.56	11.71	9.26
Turbine speed, rpm	8.80	16.80	18.00	20.40	27.30	33.10
Maximum tip speed, m/s	73.13	62.69	62.19	58.97	55.80	53.48
Turbine load coefficient	0.16	0.22	0.22	0.25	0.28	0.31
Turbine flow coefficient	0.28	0.27	0.27	0.29	0.30	0.31
Degree of reaction (at mid)	0.77	0.77	0.77	0.78	0.77	0.79
Turbine efficiency (tt)	0.86	0.89	0.89	0.89	0.90	0.90
IGVs/turbine	32	32	32	32	32	32
Rotor blades/turbine	12	14	14	15	16	16
Rotor blade mass, ton	53.25	7.80	6.48	4.22	1.84	1.05
Generator length, m	7.46	3.35	3.11	2.65	1.91	1.54
Generator diameter, m	29.85	13.39	12.43	10.61	7.65	6.14
Generator mass, ton	3390.1	494.9	414.3	283.0	129.3	76.3
Torque, MNm	290.83	26.24	21.01	13.05	4.90	2.53
Power/unit, MW	268.01	46.17	39.61	27.88	14.01	8.78
Diffuser area ratio, -	1.21	1.00	1.00	1.00	1.00	1.00
Efficiency of PCU (tt)	0.76	0.79	0.79	0.79	0.80	0.80
Ann. power output, GWh	692.43	715.68	716.37	720.35	723.90	725.97
COE, €/kWh	0.1252	0.1130	0.1119	0.1102	0.1076	0.1071

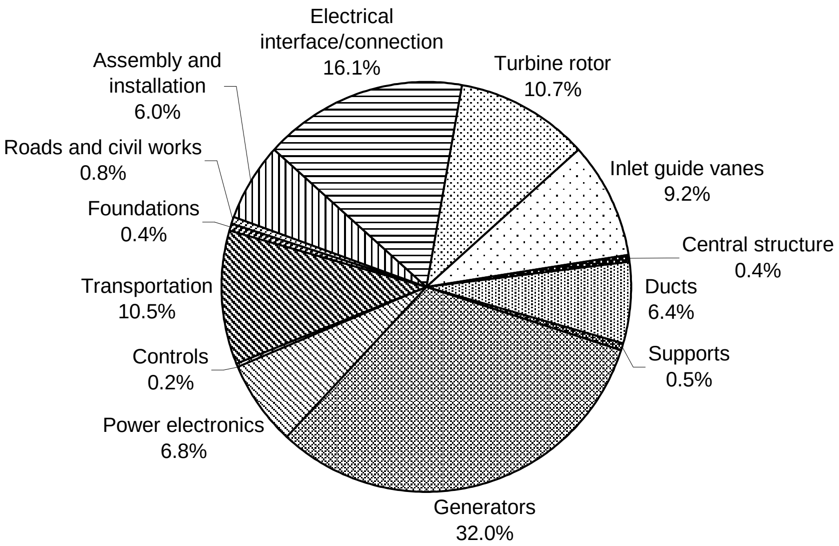

Figure 6.2 Cost components of PCU with 32 turbines.

higher yield, and a reduction in generator cost. The lowest COE is found with 32 turbines at 0.1071 €/kWh and an initial cost of the PCU of 110.16 M€. The most important cost contributors for this layout are the balance of station (33.8 %) and the generators (32.0 %). For an overview of the cost contributors where the balance of station cost is split up into subcategories see Figure 6.2. The electrical interface/connection cost is responsible for almost half of the balance of station cost and contributes 16.1 % to the total initial cost of the PCU.

Increasing the number of turbines beyond 32 does not further reduce the COE, because the reduction in generator cost is compensated by an increase in cost for transportation, for the ducts[3]and for assembly and installation, and the PCU efficiency does not improve anymore. When the number of turbines is reduced, both the COE and the initial PCU cost remain close to constant until the number of turbines is less than twenty. Even with only ten turbines the COE is only 2.8 % higher and the PCU cost is 14.8 % higher than with 32 turbines.

The multiple vertical axis turbine configuration with six or seven turbines gives a 4.5 to 5.5 % higher COE and a 22.8 to 29.1 % higher PCU cost. The highest COE results from the single vertical axis turbine configuration (+16.8 %). This configuration also requires the highest initial investment for the PCU (+84.0 %) mainly due to the high cost of the generator, which accounts for almost two thirds of the PCU cost. The mass of the generator also becomes prohibitively big (Tab. 6.4). To reduce the generator cost the optimization pushes towards higher tip speeds, which, however, increases the relative flow velocity and, therefore, has a negative impact on the efficiency. For any number of turbines the central struc-

---

[3] To fit higher numbers of turbines they have to be located further away from the chimney resulting in longer and more expensive ducts.

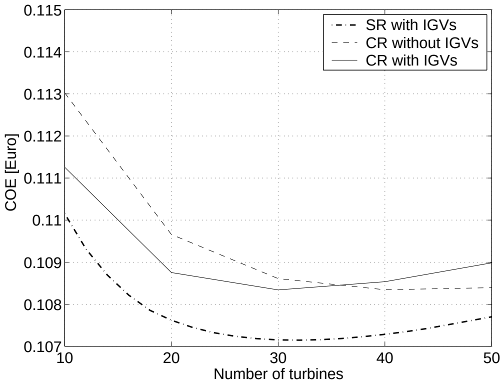

Figure 6.3 COE vs. number of turbines for various turbine layouts.

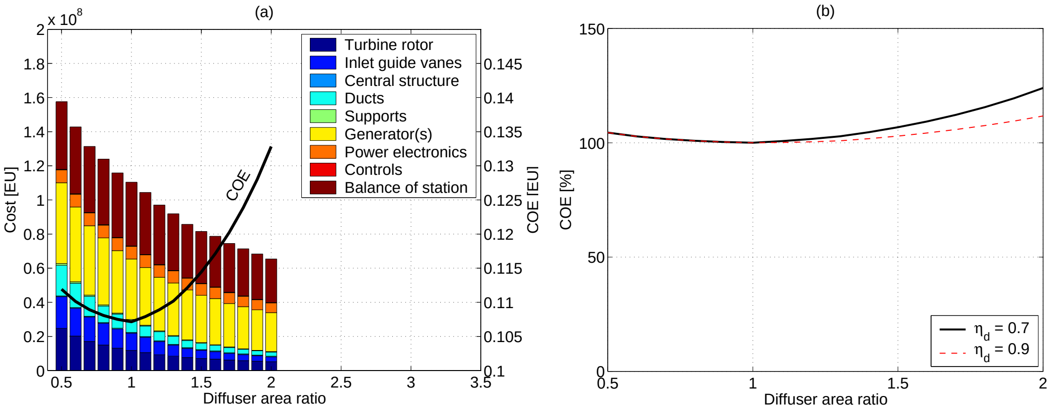

Figure 6.4 PCU cost and COE vs. diffuser area ratio for 32 single rotor turbines with IGVs (a); COE vs. diffuser area ratio for different diffuser effectiveness (b).

ture, the supports, the controls as well as roads and civil works each contribute less than one percent to the PCU cost.

The counter rotating turbine layouts show similar trends as the single rotor layout with IGVs. They provide a COE, which is only about 0.001 €/kWh higher than the one of the single rotor layout with IGVs (Fig. 6.3).

6.3.2 Sensitivity to the Diffuser Area Ratio and Diffuser Effectiveness

Figure 6.4a shows the sensitivity of COE and PCU cost to a change in the diffuser area ratio for 32 single rotor turbines with IGVs. As can also be seen in Table 6.4, the smallest COE is found at a diffuser area ratio of 1.0. Increasing the diffuser area ratio to 2.0, for example, the COE increases by 24.0 % and the PCU cost decreases by 40.7 %.

Other than the diffuser area ratio, the diffuser effectiveness, η_d, was not opti-

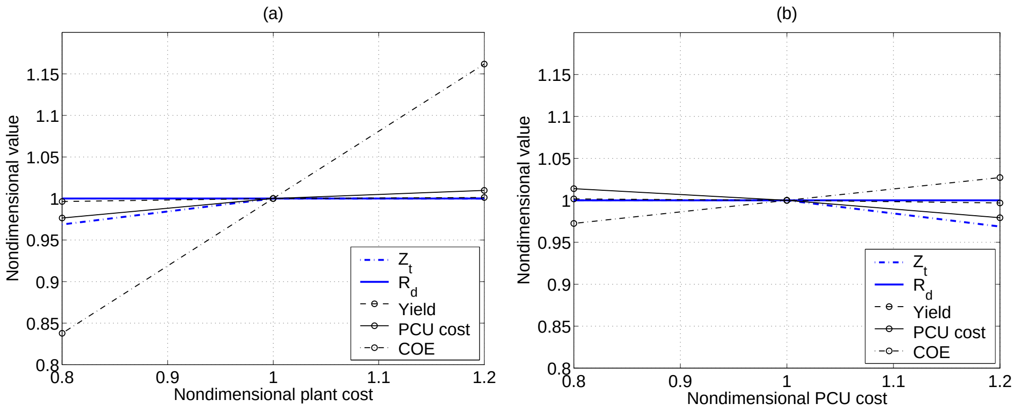

Figure 6.5 Sensitivity of various parameters to a change in plant cost (a) and PCU cost (b).

mized but assumed constant in this study. As mentioned in Section 5.1.3 (pp. 55), common values for diffuser effectiveness lie between 0.7 and 0.9 (Japikse and Baines, 1994), and a conservative value of 0.7 has been assumed in the present study. In Figure 6.4b it is shown that even with a high diffuser effectiveness of 0.9 the optimum diffuser area ratio remains at 1.0. Hence, the optimal layout of the PCU is not affected by the chosen diffuser effectiveness value, and in the remainder of this dissertation the conservative constant value of $\eta_d = 0.7$ is maintained.

6.3.3 Sensitivity to Plant Cost and PCU cost

Figure 6.5 shows the sensitivity of various parameters to a change in plant cost (a), and PCU cost (b) by ±20 %. The plant cost is the sum of chimney and collector cost. As expected, the cost of electricity is very sensitive to a change in plant cost. The PCU cost, the yield, the optimal diffuser area ratio and the optimal number of turbines, on the other hand, are hardly affected by it. And as the PCU cost is responsible for a much smaller portion of the total cost than the plant cost, the impact of a change in PCU cost is also much smaller (Fig. 6.5).

6.4 Summary and Conclusions

In this chapter a detailed cost model for the solar chimney power conversion unit has been introduced and linked to the performance models of the earlier chapters. The PCU providing the lowest cost of electricity has been found. The main conclusion of this chapter is that the multiple horizontal axis turbine configuration using a single rotor layout with IGVs provides the lowest cost of electricity. This confirms the thesis statement, which was presented in the introduction. The lowest COE (0.107 €/kWh) was found with 32 turbines and a diffuser area ratio of 1.0, i.e without nozzle or diffuser after the turbines.

For the counter rotating turbine layouts the cost of electricity is only 1.1 % higher than with a single rotor layout with IGVs. In the current study it was assumed that each of the two rotors in a counter rotating layout has its own generator. Introducing a counter rotating generator could give the counter rotating layouts a cost advantage (Kamper, 2004). However, more research would be necessary to confirm this.

Thus far, only the reference plant as described on page 14 has been considered. In the following Chapter the presented methodology will be applied to various other plant sizes and configurations.

Chapter

7

Evaluation of Various Plants

Various plant configurations are discussed in this chapter. As in the previous chapters the plant performance data are taken from simulation results using the models of Pretorius (2006). A single rotor turbine layout with inlet guide vanes was used for all plant configurations.

Pretorius (2006) links his performance model to a cost model to find the plant with the lowest initial investment cost per annual power output. This cost model is summarized and discussed in the first section of this chapter. In the second section the optimum chimney diameter is discussed using two base configurations with a 1000 m and a 1500 m high chimney.

The question of how big a first large-scale solar chimney power plant should be has been asked many times. The physics of the concept suggest to go for the largest possible plant. The efficiency of the plant increases with chimney height, and, hence, all of the configurations discussed above involve the construction of record size structures. To reduce the risk for a first prototype, building a smaller plant could be an option. The implications on the design of the PCU of building a smaller plant are discussed in the third section. Then, the PCU design for a solar chimney power plant run as a peak or base load plant is discussed. The most promising options to improve the plant performance according to Pretorius (2006) are also investigated. In the last section the findings of this chapter are summarized.

7.1 Approximate Cost Model (Pretorius, 2006)

In his Chapter 4, Pretorius (2006) links his performance model to a simple cost model to find the optimum plant configuration for three different heights of the chimney. The cost model is briefly presented here and the equations are reiterated.

To make the model independent of any currency all its equations are based on a cost unit C, which is equivalent to the volume specific chimney cost, i.e. the cost of the chimney divided by the chimney wall volume. Further, assuming that the average chimney wall thickness is one millimeter for every meter of its height, the chimney cost, including the cost for support struts and chimney foundation, is given by:

$$C_c = 0.001\pi\, d_c {H_c}^2\, \mathrm{C} \tag{7.1}$$

The specific cost of a collector roof with zero inlet height is given as a percentage of the volume specific chimney cost, C. Another percentage is added to this cost for every meter increase in collector inlet height, H_{in}. Assuming that the first percentage is 8 and the second 5, the total cost of the collector can be determined from:

$$C_{col} = \frac{\pi}{4}\, {d_{col}}^2 (0.08\,\mathrm{C})(1 + 0.05 H_{in}) \tag{7.2}$$

Pretorius (2006) used percentages of 2, 5 and 8 in both instances.

All additional costs, including the cost of the PCU, are assumed to be equal to 10 % of the sum of the chimney and collector cost. Hence, the cost of the complete plant is given by:

$$C_{tot} = 1.1\,(C_c + C_{col}) \tag{7.3}$$

The value of 10 % for the additional cost is low. Schlaich (1995) and Bernardes (2004) give values of between 27 and 48 % for the additional cost. Further, it is not evident that it should be a constant percentage of the collector and chimney cost, regardless of the plant dimensions. In Chapter 6 of the present dissertation, for example, the PCU cost varies from 16.9 to 31.1 % of the sum of the collector and chimney cost (Tab. 6.4).

To compare the plant costs presented by Pretorius (2006) to other data found in literature the cost unit C is reverted to a normal currency with a procedure presented here. To revert from the cost unit C to a normal currency, the volume specific chimney cost is needed. Data from Bernardes (2004) are used here. He gives surface area specific chimney costs in Euros for various chimney geometries in his Table 3-1. The product of the surface area specific chimney cost and the surface area equals the total chimney cost. Using the assumption that the average chimney wall thickness is one millimeter for every meter of its height the chimney volume and then the volume specific chimney cost can be determined (Tab. 7.1). The resulting values for the volume specific chimney cost lie between 240.7 and 304.8 €/m^3. The average is 266.0 €/m^3. This value is used in the following sections as the conversion rate from C to €.

7.2 Optimum Chimney Diameter

The optimal plants of Pretorius (2006) have much bigger chimney diameters than the configurations found in other literature. A change in chimney diameter has a big impact on the design of the PCU. The aim of this section is to investigate

Table 7.1 Evaluation of the volume specific chimney cost.

Bernardes, 2004				Calculated		
H_c [m]	d_c [m]	Surface area [10^3 m^2]	Cost per m^2 [€/m^2]	C_c [10^6 €]	V_c [10^3 m^3]	Cost per m^3 [€/m^3]
500	54	84.8	132	11.2	42.4	264.0
570	62	111.0	152	16.9	63.3	266.7
630	70	138.5	192	26.6	87.3	304.8
750	84	197.9	204	40.4	148.4	272.0
1000	130	408.4	248	101.3	408.4	248.0
1500	160	754.0	361	272.2	1131.0	240.7

whether the notion to use chimneys with larger diameters can be supported using the cost models and the performance models for the PCU presented in the previous chapters of this dissertation.

7.2.1 Method

Two plant geometries have been selected. For each of the two the chimney diameter has been varied while all the remaining input parameters have been kept constant:

Chimney height, m	1000	1500
Chimney diameter, m	120, 150, 180, 210, 240	160, 190, 220, 250, 280
Collector diameter, m	5000	7000
Coll. inlet roof height, m	5	6

Sandstone has been used as the ground material. Wind and chimney shadow effects have been included and a dry adiabatic lapse rate has been assumed for the vertical temperature profile inside and outside the chimney in all cases. The operating conditions for the PCU of the various plants are summarized in Tables G.2 to G.11 (pp. 110).

For the cost of electricity evaluation the cost models and procedures presented in Chapter 6 are used. To allow for the variation in chimney geometry, a parametric chimney cost model is employed. According to Bernardes (2004), the surface area specific chimney cost, b, can be approximated as a function of the chimney height, H_c, and the chimney diameter, d_c. His Equation 3-4 is used and reiterated here for convenience[1]:

$$b\ [€/m^2] = 35.39 + 0.2315\, H_c - 0.1223 d_c \tag{7.4}$$

---

[1] As curvature and its positive effect on stability decreases with chimney diameter, it is doubtful that the specific chimney cost decreases with an increase in chimney diameter. Hence, this approximation for area specific chimney cost should be scrutinized in future work.

The initial cost of the chimney, C_c, can then be evaluated from:

$$C_c\ [€] = b \times H_c \times \pi \times d_c \tag{7.5}$$

To facilitate the direct comparison to the results of the approximate cost model of Pretorius (2006) the conversion rate of 266 €/C, as introduced in Section 7.1, is used.

7.2.2 Results

As can be seen from Figure 7.1 the notion to use larger chimney diameters can indeed be supported using the cost models and the performance models for the PCU presented in the previous chapters; for the plant with a 1000 m high chimney the optimum chimney diameter is between 150 and 180 m. For the plant with a 1500 m high chimney, the optimum chimney diameter is 190 m. These values are higher than the ones cited in earlier publications. But they are also significantly lower than the ones suggested by Pretorius (2006) (210 m for the 1000 m high chimney and 280 m for the 1500 m high chimney). This is because the plant cost model and the cost model for the PCU used here are more sensitive to a change in chimney diameter than the ones of Pretorius (2006) as the collector cost is less dominant.

The PCU cost as a percentage of the sum of the collector and chimney cost ranges from 16.6 to 29.7 % (Tab. 7.2 and Tab. 7.3). To do a proper optimization of the plant, the cost model and the performance model of the PCU presented in this dissertation should be included in the plant performance model.

As the plant configuration with a 1500 m high and 160 m wide chimney is the same as the one discussed in the previous chapter, the results could be expected to be the same. Note, however, that the chimney cost differs in the two cases: in Chapter 6 a chimney cost of 272 M€ has been assumed. In the present chapter Equations 7.4 and 7.5 have been employed. They give a slightly higher chimney cost of 273.7 M€. Therefore, the results also differ slightly.

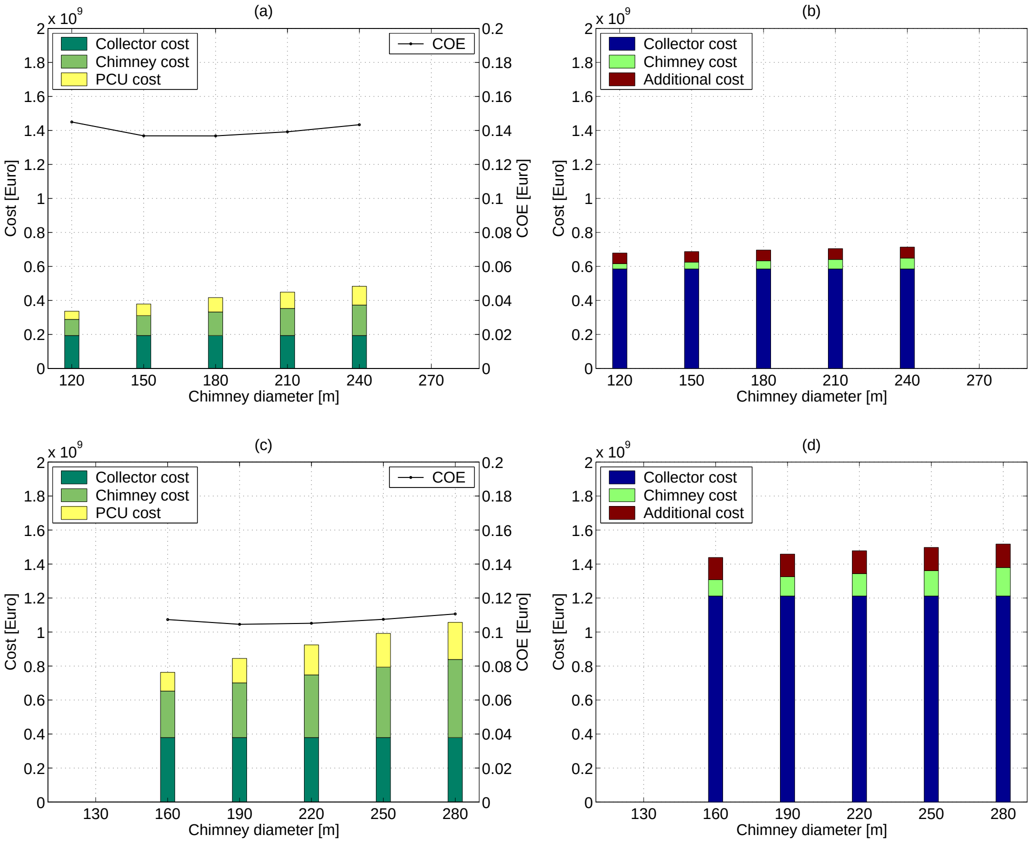

Figure 7.1 Plant cost and COE vs. chimney diameter for the reference plant with (a) a 1000 m and (c) a 1500 m high chimney. Figures (b) and (d) represent the plant cost from the cost model of Pretorius (2006) and an assumed volume specific chimney cost of 266 €/m^3.

Table 7.2 Results for various chimney diameters for the plant with a 1000 m high chimney.

Chimney height, [m]	**1000**				
Chimney diameter, [m]	120	150	180	210	240
Number of turbines, [-]	19	23	26	27	29
Turbine diameter, [m]	30.0	34.1	36.6	38.7	41.0
Turbine speed, [rpm]	28	25	23	21	20
Turbine tip speed, [m/s]	43.9	44.0	43.3	42.6	42.0
Turbine through flow velocity, [m/s]	14.3	12.6	12.3	12.4	11.6
Diffuser area ratio, [-]	1.0	1.0	1.1	1.3	1.4
Efficiency of PCU (tt), [%]	79.8	79.9	79.1	78.0	77.8
Annual power output, [GWh]	240.7	284.7	311.3	328.0	341.8
Cost of collector, [M€]	193.4	193.4	193.4	193.4	193.4
Cost of chimney, [M€]	95.1	117.1	138.5	159.1	179.1
Cost of PCU, [M€]	48.2	68.4	84.8	96.1	111.0
Cost of PCU, [as % of $C_c + C_{col}$]	16.7	22.0	25.5	27.3	29.8
Cost of electricity, [€/kWh]	0.1449	0.1368	0.1368	0.1392	0.1433

Table 7.3 Results for various chimney diameters for the plant with a 1500 m high chimney.

Chimney height, [m]	**1500**				
Chimney diameter, [m]	160	190	220	250	280
Number of turbines, [-]	32	36	39	41	42
Turbine diameter, [m]	30.9	34.6	37.8	39.4	41.3
Turbine speed, [rpm]	33	30	27	25	24
Turbine tip speed, [m/s]	53.6	53.5	53.4	52.4	52.0
Turbine through flow velocity, [m/s]	16.8	15.3	14.2	14.3	14.1
Diffuser area ratio, [-]	1.0	1.0	1.0	1.2	1.3
Efficiency of PCU (tt), [%]	80.1	80.1	80.0	79.2	78.7
Annual power output, [GWh]	725.9	820.8	888.6	930.2	960.3
Cost of collector, [M€]	379.1	379.1	379.1	379.1	379.1
Cost of chimney, [M€]	273.7	321.8	368.8	414.8	459.7
Cost of PCU, [M€]	110.1	144.0	176.2	198.1	217.9
Cost of PCU, [as % of $C_c + C_{col}$]	16.9	20.5	23.6	24.9	26.0
Cost of electricity, [€/kWh]	0.1073	0.1045	0.1052	0.1075	0.1106

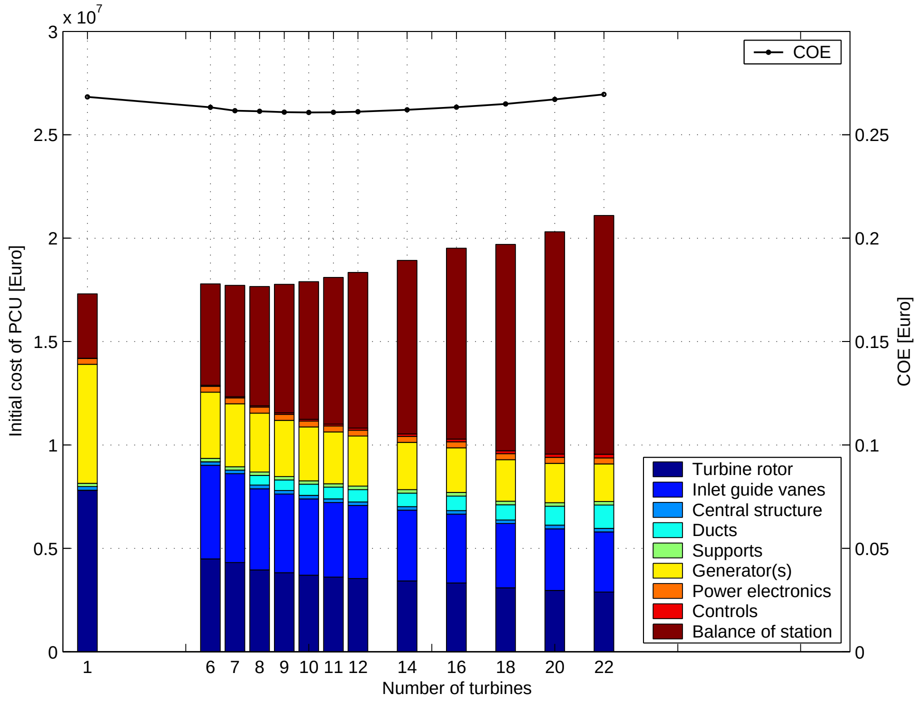

Figure 7.2 Plot of plant cost and COE vs. number of turbines for a plant with a 500 m high chimney. (The configurations with 1, 6 and 7 turbines employ vertical axis turbines.)

7.3 PCU for a Smaller Plant

The smaller reference plant of Pretorius (2006) with a chimney height of 500 m has a chimney diameter of 100 m, a collector diameter of 2000 m and a collector inlet height of 4 m. As in the section above, Sandstone has been used as the ground material for the simulation. Wind and chimney shadow effects have been included and a dry adiabatic lapse rate has been assumed for the vertical temperature profile inside and outside the chimney. For the cost of electricity evaluation the same cost models and procedures as described in Section 7.2 are used. The operating conditions for the PCU of this plant are summarized in Table G.12 (p. 113).

For this plant configuration a PCU with 10 horizontal axis turbines provides the lowest cost of electricity (Fig. 7.2 and Tab. 7.4). Even though the overall plant cost for this small plant is only a fraction of the cost of a large plant (e.g. a tenth of the cost of the reference plant with a 1500 m high chimney) the optimal cost of electricity is 2.5 times higher due to a much lower annual power output.

In comparison to the plant discussed in Chapter 6, for the smaller plant discussed here, the generators, the electrical interface/connection, the power electronics and the ducts contribute a much smaller portion to the PCU cost (compare Fig. 7.3 to Fig. 6.2). In contrast, the inlet guide vanes, the turbine rotors,

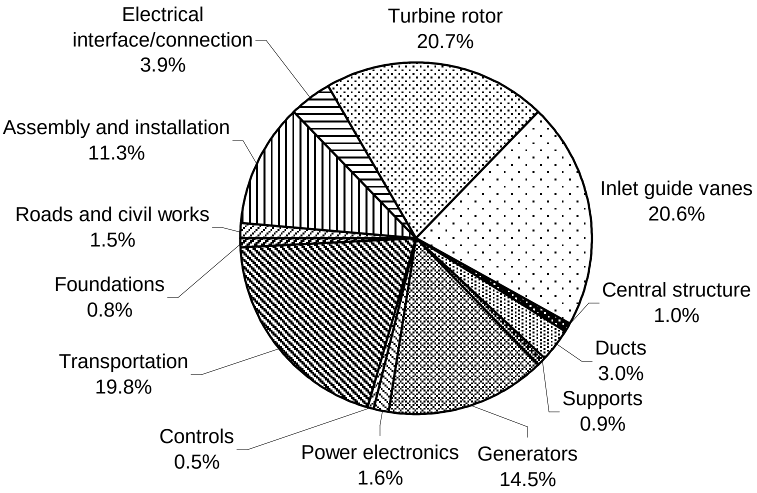

Figure 7.3 Cost components of a PCU with 10 turbines for a plant with a 500 m high chimney.

transportation as well as assembly and installation contribute a much bigger portion.

The cost of the chimney is 21.82 M€, the cost of the collector 30.77 M€. The initial capital cost of the PCU is between 17.30 and 20.31 M€, which is equal to 32.9 to 38.6 % of the sum of the cost of the collector and the chimney. This is a much bigger portion than for the larger plants. As a consequence the optimal diffuser area ratio is higher for the smaller plant and the efficiency of the PCU is reduced.

7.4 Peak and Base Load Operation

One prominent disadvantage of most concepts, which use solar radiation to generate electricity, is that the power output is fluctuating approximately proportional to the amount of momentary radiation. This also applies to the solar chimney concept, but with certain modifications to the plant, originally proposed by Kröger, peak or base load operation is possible as reported by Pretorius (2006).

The aim of this section is to show the impact on the PCU design and on the cost of electricity of such a change in plant control strategy. The plant performance data from the simulations of Pretorius (2006) are used for this investigation. He modelled his reference plant with a 1000 m high chimney as a peak and base load plant. The plant has a chimney diameter of 210 m, a collector diameter of 5000 m and a collector inlet height of 5 m. As in the section above, Sandstone has been used as the ground material for the simulation. Wind and chimney shadow effects have been included, and a dry adiabatic lapse rate has been assumed for the vertical temperature profile inside and outside the chimney.

Table 7.4 Cost and performance results for various numbers of turbines for a smaller plant.

Number of turbines	**1**	**6**	**7**	**8**	**10**	**18**
Turbine rotor, M€	7.81	4.49	4.31	3.96	3.70	2.96
Inlet guide vanes, M€	0.00	4.53	4.30	3.93	3.69	2.99
Central structure, M€	0.17	0.17	0.17	0.17	0.17	0.17
Ducts, M€	0.00	0.00	0.00	0.47	0.54	0.92
Supports, M€	0.16	0.16	0.16	0.16	0.16	0.17
Generators, M€	5.76	3.20	3.04	2.85	2.60	1.90
Power electronics, M€	0.28	0.29	0.29	0.29	0.29	0.29
Controls, M€	0.01	0.05	0.06	0.07	0.08	0.16
Transportation, M€	0.82	2.38	2.69	2.96	3.54	6.27
Foundations, M€	0.38	0.13	0.13	0.13	0.14	0.18
Roads & civil works, M€	0.11	0.19	0.21	0.22	0.26	0.43
Assembly & inst., M€	1.14	1.53	1.67	1.77	2.02	3.18
El. Int./connections, M€	0.66	0.68	0.69	0.69	0.69	0.69
Balance of station, M€	3.11	4.91	5.38	5.77	6.66	10.75
Initial capital cost, M€	17.30	17.79	17.72	17.66	17.89	20.31
Turbine diameter, m	95.69	39.37	36.81	34.03	30.86	22.18
Blade length, m	28.71	11.81	11.04	10.21	9.26	6.65
Turbine speed, rpm	7.58	14.00	14.80	15.80	17.40	24.00
Maximum tip speed, m/s	37.98	28.86	28.53	28.15	28.12	27.87
Turbine load coefficient	0.13	0.24	0.24	0.25	0.25	0.26
Turbine flow coefficient	0.24	0.32	0.31	0.32	0.32	0.31
Degree of reaction (at mid)	0.77	0.77	0.77	0.77	0.77	0.77
Turbine efficiency (tt)	0.85	0.89	0.89	0.89	0.89	0.89
IGVs/turbine	32	32	32	32	32	32
Rotor blades/turbine	11	15	15	15	15	15
Rotor blade mass, ton	15.82	1.88	1.60	1.32	1.05	0.47
Generator length, m	2.66	1.20	1.13	1.05	0.95	0.68
Generator diameter, m	10.65	4.82	4.50	4.21	3.79	2.71
Generator mass, ton	286.11	42.62	36.19	30.88	24.01	10.72
Torque, MNm	13.23	1.22	1.00	0.82	0.60	0.22
Power/unit, MW	10.50	1.80	1.55	1.35	1.09	0.55
Diffuser area ratio, -	1.30	1.28	1.26	1.29	1.25	1.21
Efficiency of PCU (tt)	0.75	0.77	0.77	0.77	0.78	0.78
Ann. power output, GWh	27.93	28.65	28.80	28.81	28.96	29.14
COE, €/kWh	0.2683	0.2633	0.2616	0.2613	0.2608	0.2671

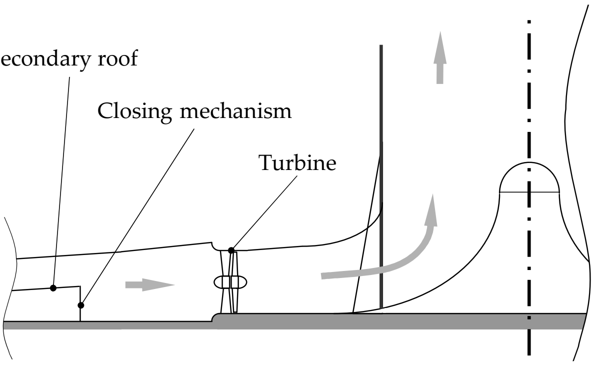

Figure 7.4 Solar chimney power plant with a secondary collector roof and a closing mechanism for peak and base load operation.

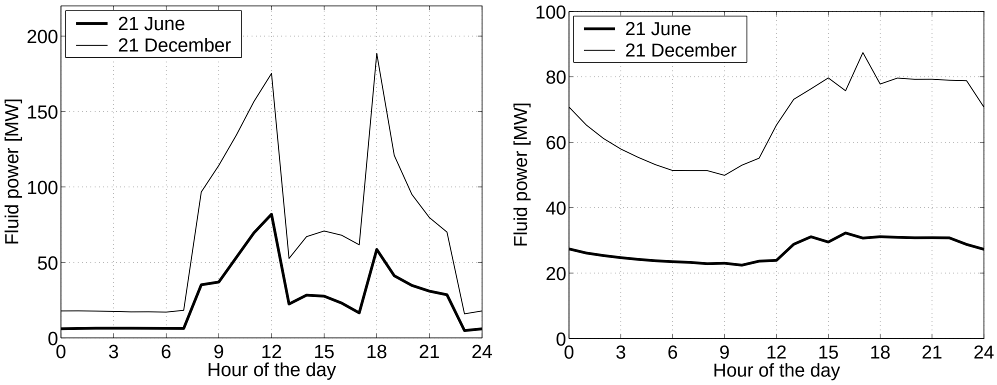

Figure 7.5 Fluid power vs. hour of the day for peak (left) and base load operation.

7.4.1 Modifications to the Plant

To enable a better control of the plant output Pretorius (2006) introduced a secondary collector roof under the main collector roof (see Fig. 7.4). The assumption was made that the bottom section of the collector below this secondary roof can be closed off, completely or partially, with a closing mechanism located close to the turbine inlets. With a closed bottom section the overall air flow through the plant and, hence, the power output are reduced; heat is stored in the ground. With the strategy of Pretorius (2006) the daily power fluctuations can be controlled well (Fig. 7.5)[2]. The operating conditions for the PCUs of the peak and base load plants presented here are summarized in the Tables G.13 and G.14 on page 113.

---

[2] Pretorius (2006) also presents strategies to control the seasonal power fluctuations. They are, however, not discussed here.

Table 7.5 Results for the plant with a 1000 m high chimney operating in peak or base mode compared to the reference plant.

Plant operating mode	Reference	Base	Peak
Number of turbines, [-]	27	25	29
Turbine diameter, [m]	38.7	41.8	38.5
Turbine speed, [rpm]	21.0	13.7	21.6
Turbine tip speed, [m/s]	42.6	30.0	43.6
Turbine through flow velocity, [m/s]	12.4	8.7	12.2
Diffuser area ratio, [-]	1.30	1.20	1.22
Efficiency of PCU (tt), [%]	78.0	79.9	79.3
Annual power output, [GWh]	328.0	332.0	341.8
Cost of collector, [M€]	193.4	309.4	309.4
Cost of chimney, [M€]	159.1	159.1	159.1
Cost of PCU, [M€]	96.1	88.8	108.2
Cost of PCU, [as % of $C_c + C_{col}$]	27.3	19.0	23.1
Cost of electricity, [€/kWh]	0.139	0.169	0.170

7.4.2 Modifications to the Models

Allowing for the cost of the secondary roof, the area specific cost of the collector is assumed to be 1.6 times higher than the one of the reference plant. This value was chosen according to the following rationale: It is assumed that with a secondary roof the amount of glass needed to build the whole collector will increase by a factor 2, the amount of steel by a factor 1.5 and the amount of concrete will remain the same. Using these assumptions and the values in Table 4-1 of Bernardes (2004) with a secondary roof the area specific cost of the collector will increase by 61.2 %. The other models and parameters are the same as in the previous sections.

7.4.3 Results

The peak load and the base load plant deliver almost the same annual power output as the reference plant, which does not have a secondary roof and is therefore cheaper (Tab. 7.5). As a consequence the cost of electricity for the peak and base load plants is 21.5 and 21.9 % higher. They are, however, not optimized; a secondary roof, which would only cover the inner part of the collector, could be a more cost effective solution, for example.

The PCU cost is significantly lower for the base load plant. The cost of the drive train in particular is proportional to the peak power output of the plant, which is much lower for base load operation (Tab. 7.7, p. 88). Note that the cost of the closing mechanism for the bottom section of the collector has been disregarded in this study.

7.5 Collector with Double Glazing and Anti-Reflective Coating

Pretorius (2006) presents several possible modifications to the reference plant and investigates their individual impact on the power output. The most promising options are double-glazing of the collector and anti-reflective coating of the collector roof glass. According to Pretorius (2006) double glazing of the whole collector increases the annual power output by more than 30 %. Applying an anti-reflective coating increases the annual power output by 13.9 %.

In this section a new plant configuration is introduced, where the inner half of the collector is double-glazed. Then, the effect of applying anti-reflective coating to this collector is investigated. For double glazing Pretorius (2006) did a parametric study on the spacing of the two glass layers. He used a spacing of 0.006 m, 0.01 m and 0.03 m respectively and found that they give annual power outputs of 444.6 GWh, 463.6 GWh and 466.8 GWh. Since the performance is not enhanced significantly by increasing the gap beyond 0.01 m this value is chosen in this section. It is assumed that the anti-reflective coating reduces the reflectance of each glass layer to a quarter of its original value (Pretorius, 2006). The PCU operating conditions are summarized in the Tables G.15 and G.16 on page 114.

7.5.1 Modifications to the Models

Similar to Section 7.4.2 it is assumed that for double glazing the amount of glass needed per area will increase by a factor 2, the amount of steel by a factor 1.2 and the amount of concrete will remain the same. Using these assumptions and the values in Table 4-1 of Bernardes (2004) for the double glazed sector of the collector the area specific cost will increase by 45.4 %. This value has been implemented in the cost model.

According to Wittwer (2007) low iron glass with anti-reflective coating costs between 25 and 30 €/m^2, but in the long term, mainly due to economies of scale, the cost of the coating could come down to a price below 2 €/m^2. In the current study a coating cost of 2 €/m^2 is assumed.

7.5.2 Results

Implementation of double glazing and anti-reflective coating holds a potential to significantly reduce the cost of electricity of the solar chimney power plant (Tab. 7.6). With the models chosen in this study the cost of electricity is reduced by 17.8 %. The annual power output increases by 51.7 % while the initial investment cost only increases by 26.0 %. Note, however, that the cost values assumed for double glazing and particularly for anti-reflective coating are optimistic. The presented results are understood as the achievable limit on the low side.

Other parameters of the PCU are also listed in Table 7.7 (p. 88). The optimum number of turbines and the turbine speed increase slightly with double glazing

Table 7.6 Results for the plant with a 1000 m high chimney. Reference plant results are compared to a plant with a double glazed inner half of the collector (DG) and a plant with a double glazed inner half of the collector and all the glass coated with an anti-reflective layer (DG & AR).

	Reference	**DG**	**DG & AR**
Number of turbines, [-]	27	29	30
Turbine diameter, [m]	38.7	37.5	37.4
Turbine speed, [rpm]	21	23	24
Turbine tip speed, [m/s]	42.6	44.7	46.3
Turbine through flow velocity, [m/s]	12.4	12.7	12.8
Diffuser area ratio, [-]	1.30	1.29	1.25
Efficiency of PCU (tt), [%]	78.0	78.6	79.1
Annual power output, [GWh]	328.0	415.5	497.8
Cost of collector, [M€]	193.4	237.3	296.2
Cost of chimney, [M€]	159.1	159.1	159.1
Cost of PCU, [M€]	96.1	102.2	110.2
Cost of PCU, [as % of $C_c + C_{col}$]	27.3	25.8	24.2
Cost of electricity, [€/kWh]	0.139	0.121	0.114

and anti-reflective coating, but the diameter of the individual turbine is reduced.

7.6 Summary and Conclusion

Figure 7.6 gives a good overview over the main findings of this chapter. A large plant with e.g. a 1500 m tall chimney provides a low cost of electricity and a high annual power output. But the financial (and technological) risk is also high. Moving towards smaller plants the risk is reduced. But the annual power output is also reduced, and the cost of electricity increases. Measures like double glazing and anti-reflective coating could counteract this trend.

While the size and performance of the different plants vary a lot, the optimal PCUs all look very similar (Tab. 7.7). The optimal number of turbines varies, but their individual size, the number of blades and even the efficiency of the PCU remain close to constant. For all plants discussed here, even for the smaller plant, PCUs with multiple horizontal axis turbines provide the lowest cost of electricity. The cost of the PCU, however, varies significantly. As mentioned in Section 1.4.2, Bernardes (2004) assumes a specific initial cost of the PCU of 767 € per kW rated power. In the present chapter the specific initial cost of the PCU varies from 437 to 1644 €/kW.

Further, the results presented here show that, with a modified collector including a secondary roof, peak and base load operation is possible at a cost of electricity only slightly over 20 % higher than for a configuration without a sec-

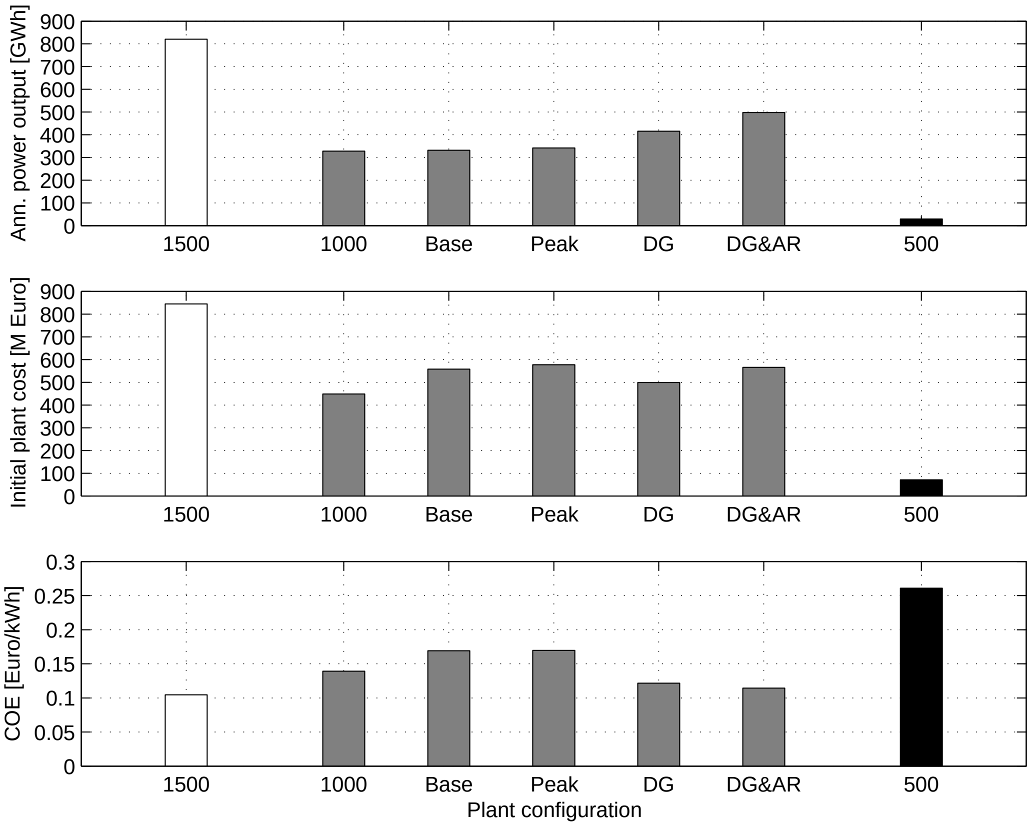

Figure 7.6 Annual power output (top), initial plant cost (middle) and cost of electricity (bottom) for various plant configurations. *1500:* reference plant with 1500 m high chimney; *1000:* reference plant with 1000 m high chimney; *Base:* base load plant; *Peak:* peak load plant; *DG:* plant with double glazing; *DG&AR:* plant with double glazing and anti-reflective coating; *500:* small plant with 500 m high chimney.

ondary roof. Hence, implementing a peak load solar chimney power plant could be an interesting option.

Table 7.7 Optimum parameters for the PCUs of the various plant configurations.

Configuration	**1500**	**1000**					**500**
		Ref	Base	Peak	DG	DG&AR	
Chimney height, m	1500	1000	1000	1000	1000	1000	500
Chimney diameter, m	190	210	210	210	210	210	100
Collector diameter, m	7000	5000	5000	5000	5000	5000	2000
Number of turbines	36	27	25	29	29	30	10
Turbine rotor, M€	16.61	15.22	18.35	16.74	15.30	16.03	3.70
Inlet guide vanes, M€	14.67	14.91	16.56	15.62	14.66	15.05	3.69
Central structure, M€	0.63	0.77	0.77	0.77	0.77	0.77	0.17
Ducts, M€	11.79	6.00	5.97	7.54	6.87	7.68	0.54
Supports, M€	0.74	0.70	0.76	0.74	0.70	0.73	0.16
Generators, M€	46.27	27.19	20.99	31.57	29.44	32.60	2.60
Power electronics, M€	8.75	3.65	1.84	4.35	4.29	4.91	0.29
Controls, M€	0.30	0.22	0.21	0.24	0.24	0.25	0.08
Transportation, M€	13.57	10.63	10.57	11.50	11.26	11.68	3.54
Foundations, M€	0.61	0.57	0.62	0.60	0.57	0.59	0.14
Roads & civil works, M€	1.01	0.83	0.83	0.89	0.87	0.90	0.26
Assembly & inst., M€	8.15	6.76	7.01	7.29	7.04	7.29	2.02
El. Int./connections, M€	20.86	8.70	4.38	10.39	10.23	11.72	0.69
Balance of station, M€	44.22	27.48	23.40	30.67	29.97	32.18	6.66
Initial capital cost, M€	144.0	96.1	88.8	108.2	102.2	110.2	17.9
Turbine diameter, m	34.55	38.75	41.83	38.52	37.46	37.43	30.86
Blade length, m	10.37	11.62	12.55	11.56	11.24	11.23	9.26
Turbine speed, rpm	29.60	21.00	13.70	21.60	22.80	23.60	17.40
Maximum tip speed, m/s	53.55	42.61	30.01	43.57	44.72	46.25	28.12
Turbine load coefficient	0.28	0.24	0.30	0.26	0.25	0.25	0.25
Turbine flow coefficient	0.29	0.29	0.29	0.28	0.28	0.28	0.32
Degree of reaction (at mid)	0.77	0.77	0.77	0.77	0.77	0.77	0.77
Turbine efficiency (tt)	0.90	0.89	0.90	0.90	0.89	0.90	0.89
IGVs/turbine	32	32	32	32	32	32	32
Rotor blades/turbine	16	15	16	15	15	15	15
Rotor blade mass, ton	1.37	1.81	2.17	1.78	1.67	1.66	1.05
Generator length, m	1.62	1.49	1.40	1.53	1.49	1.53	0.95
Generator diameter, m	6.46	5.96	5.61	6.12	5.97	6.11	3.79
Generator mass, ton	86.21	70.93	61.33	75.47	71.39	75.38	24.01
Torque, MNm	2.95	2.31	1.93	2.50	2.33	2.50	0.60
Power/unit, MW	9.15	5.09	2.77	5.66	5.57	6.17	1.09
Specif. PCU cost, €/kW	437	700	1284	660	633	595	1644
Diffuser area ratio, -	1.00	1.30	1.20	1.22	1.29	1.25	1.25
Efficiency of PCU (tt)	0.80	0.78	0.80	0.79	0.79	0.79	0.78
Ann. power output, GWh	820.8	328.0	332.0	341.8	415.5	497.8	28.96
COE, €/kWh	0.105	0.139	0.169	0.170	0.121	0.114	0.261

Chapter

8

Conclusion

The main aim of this dissertation was to find the solar chimney power conversion unit providing the lowest cost of electricity. In the first chapter a brief introduction to the solar chimney power plant concept was given; its history as well as the fields of research associated with the concept were presented. A comparison to other power schemes was provided, various possible layouts for the power conversion unit were introduced, a dissertation outline was given and the potential impact of this dissertation was discussed. Operating conditions for the power conversion unit resulting from simulations for one year were also analyzed, and it was found that a variable speed turbine stage can cover all operating conditions at close to constant efficiency, as they can be fitted with the ellipse law of Stodola.

In the second chapter, turbine layouts and mathematical turbine models were identified from the literature. The models were assessed and modified. The turbine layouts under consideration were single rotor and counter rotating turbines, both with or without inlet guide vanes. It was found that small modifications of the modelling approach can have a significant impact on the performance prediction and may lead to an error in turbine efficiency estimation. It was also shown that ignoring constraints on the degree of reaction of the turbine may falsely promote one layout over another. Further, it was found that the single rotor layout without guide vanes performs very poorly in terms of total-to-static efficiency. The other three layouts provide higher total-to-static efficiencies which are all similar to each other. The counter rotating layouts provide the highest peak efficiencies, but at relatively low speeds, which leads to an undesirable higher torque for the same power output.

Experiments with a multiple turbine rig presented in the third chapter show that a turbine designed with a comparably simple method gives fairly high efficiencies. The validity of the Soderberg loss model in context with solar chimney turbines is also confirmed with this experimental data and with an in depth analysis of experimental data from a single turbine rig.

A first evaluation of a commercial CFD package as a tool in context with solar chimney turbines was made. Both solar chimney turbine rigs of Stellenbosch University were modelled in 3D. The level of agreement between numerical and experimental results was found to be encouraging for future use of CFD to model full scale solar chimney power conversion units, and, as with the experimental data, the validity of the Soderberg loss model in context with solar chimney turbines was confirmed.

For each component of the power conversion unit a performance model has been introduced. A detailed cost model for the solar chimney power conversion unit has also been proposed. Applying this cost model together with the performance models on a plant configuration with a chimney height of 1500 m, a chimney diameter of 160 m and a collector diameter of 7000 m the following has been demonstrated:

1. The power conversion unit providing the minimal cost of electricity consists of 32 horizontal axis turbines using a single rotor layout including inlet guide vanes.

2. With the given cost assumptions, the lowest cost of electricity for this plant configuration is 0.107 €/kWh.

3. The cost of electricity is highly sensitive to the diffuser area ratio. The lowest COE is found at a diffuser area ratio of 1.0, i.e without nozzle or diffuser after the turbines. Increasing the diffuser area ratio to 2.0, for example, the COE increases by 24.0 %.

4. The electrical interfaces/connections and the generators are the main contributors to the cost of the optimal power conversion unit. Together they are responsible for more than half of the PCU cost. Other significant cost contributors are the power electronics, transportation, the turbine rotors, assembly and installation, the inlet guide vanes and the ducts. Roads and civil works, the central structure, foundations, the supports, as well as the controls each contribute less than one percent to the PCU cost.

5. The main drawback for the vertical axis turbine configurations is the costly and bulky generator. For the single vertical axis turbine configuration, for example, the generator would be responsible for more than 60 % of the PCU cost and would weigh 3390 tons.

With the same cost and performance models several other plant geometries and configurations have also been studied. The most important results of this investigation are the following:

1. When changing the size of the plant the design of the optimal power conversion unit does not vary much; mainly the optimal number of turbines changes. Both, the absolute cost and the power specific cost of the PCU

vary significantly, however. Hence, cost models assuming constant values will not give accurate results for a wide range of plant geometries.

2. The assumption made by many other researchers that the total-to-total efficiency of the PCU is 80 % has been confirmed, as values between 78 and 80 % were found.

3. The optimal chimney diameter is larger than the one mentioned in earlier sources, but not as large as suggested by Pretorius (2006).

4. A peak or base load plant using a secondary collector roof gives an only slightly over 20 % higher COE than a configuration without a secondary roof. Hence, implementing a peak load solar chimney power plant could be an interesting option in certain regions.

5. Double glazing the collector roof and treating it with an anti-reflective coating holds a potential to reduce the cost of electricity and to increase the annual power output of a given SCPP configuration significantly. This could make plants with smaller chimneys economically viable.

Future work

The models presented here have to be integrated with a plant performance and cost model to enable a more accurate optimization. The structural aspects of SCPCUs also need to be investigated further. This will give a good basis to do preliminary design studies. But to substantially increase the knowledge on solar chimney power plant technology, the construction of a small plant similar to the one discussed in Section 7.3 has to be envisaged.

Appendix

A

Calibration Data

Information on the calibration of the Venturi meter and the torque transducer used on the multiple turbine rig is given in this appendix. The Venturi meter of the wind tunnel, which was used for the volume flow evaluation in the experiments on the multiple turbine rig, was calibrated using a pitot tube in the middle of the test section. With the pitot tube the flow velocity in the test section was measured. This value was multiplied with the area of the test section to give the volume flow[1]. The curve fitted through the measured data as shown in Figure A.1 follows the relationship

$$y = \sqrt{\frac{x - 1.3334}{0.0567}} + 0.03 \qquad \text{(A.1)}$$

The calibration curve of the pressure transducer used with the Venturi meter was $y = 223.62x - 298.59$.

The torque transducer was calibrated in the rig. A certain torque was applied to the shaft on the turbine side, by attaching a balanced steel bar horizontally

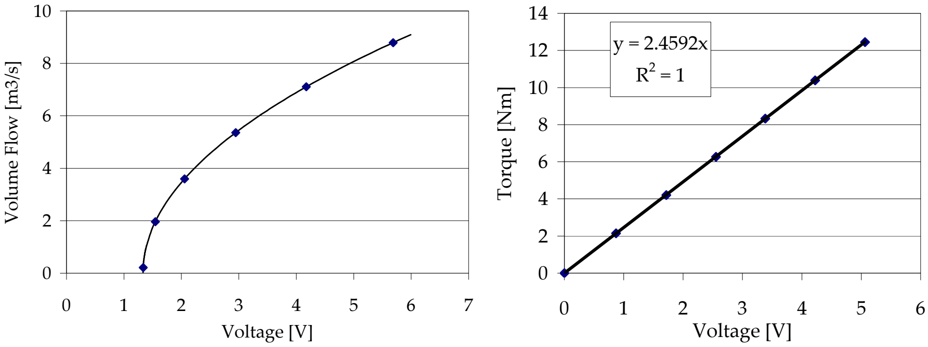

Figure A.1 Calibration curves for the Venturi meter of the wind tunnel (left) and for the torque transducer (right).

---

[1] The boundary layers in the test section may be neglected as they are very thin, which was verified before the tests

on the shaft and adding weights at a defined distance (210 mm) from the axis of rotation. The shaft on the generator side was locked in position. The resulting calibration curve is shown in Figure A.1.

Appendix

B

Experimental Error Estimation

An error estimation for the total-to-total turbine efficiency measurement is presented here.

The turbine total-to-total efficiency is evaluated from Equation 3.2, which can be written as

$$\eta_{tt} = \frac{T_q \omega}{Q \Delta p_t} \tag{B.1}$$

where Δp_t is the difference in total pressure across the turbine stage.

The nominal values and the estimated error of the components of this equation are listed in Table B.1.

The estimated error for the torque and the volume flow rate are the maximum standard deviations of the measurements. The turbine speed error is taken from the specifications of the tachometer manufacturer. And the total pressure difference error is the sum of the maximum standard deviations of the two total pressure readings.

Using these values and combining the errors in quadrature the propagated

Table B.1 Nominal values and estimated error of test results.

	Nominal value	Error
Torque, Nm	5.51	0.02
Turbine speed, rad/s	123.1	0.1
Volume flow rate, m^3/s	3.89	0.01
Total pressure difference, Pa	241.8	1.0

error is

$$\frac{\delta\eta_{tt}}{\eta_{tt}} = \sqrt{\left(\frac{\delta T_q}{T_q}\right)^2 + \left(\frac{\delta\omega}{\omega}\right)^2 + \left(\frac{\delta Q}{Q}\right)^2 + \left(\frac{\delta(\Delta p_t)}{\Delta p_t}\right)^2} \tag{B.2}$$

$$= \sqrt{\left(\frac{0.02}{5.51}\right)^2 + \left(\frac{0.1}{123.1}\right)^2 + \left(\frac{0.01}{3.89}\right)^2 + \left(\frac{1.0}{241.8}\right)^2} \tag{B.3}$$

$$= 0.0061$$

As the total to total efficiency in this case is 86.5 % the absolute estimated error is

$$\delta\eta_{tt} = 0.0061 \times 86.5\,\% = 0.53\,\% \tag{B.4}$$

Appendix C

Tabulated Experimental Data

Table C.1 Turbine characteristic data for the multiple turbine rig as presented in Figure 3.8.

Φ	Ψ	η_{tt}	η_{ts}
-	-	%	%
0.22	0.04	80.3	54.9
0.23	0.06	85.2	61.3
0.24	0.06	86.3	63.2
0.25	0.07	86.9	64.2
0.26	0.08	86.7	64.4
0.27	0.09	86.8	65.3
0.28	0.10	85.7	65.2
0.30	0.11	82.5	63.1

Table C.2 Velocity profile data for the multiple turbine rig as presented in Figure 3.10 (Traverse before rotor).

r mm	C_{r2} m/s	C_{t2} m/s	C_{x2} m/s	p_{s2} Pa	p_{t2} Pa
0.349	0.40	-3.64	12.72	-121.7	-18.7
0.344	0.20	-3.55	12.86	-118.2	-13.6
0.339	-0.24	-3.69	12.39	-111.0	-12.5
0.334	-0.46	-3.88	12.39	-107.7	-8.4
0.329	-0.54	-4.09	12.25	-104.5	-6.3
0.324	-0.60	-4.35	12.20	-102.6	-4.0
0.319	-0.57	-4.61	12.05	-100.8	-2.8
0.314	-0.51	-4.85	11.95	-99.3	-1.6
0.309	-0.45	-4.89	11.84	-97.9	-1.6
0.304	-0.42	-5.00	11.74	-97.5	-1.9
0.299	-0.38	-5.08	11.60	-97.0	-3.0
0.294	-0.37	-5.16	11.50	-96.5	-3.3
0.289	-0.36	-5.38	11.34	-95.9	-3.6
0.284	-0.38	-5.56	11.26	-95.9	-3.4
0.274	-0.32	-5.79	11.18	-96.6	-3.8
0.264	-0.34	-6.01	11.08	-97.1	-4.0
0.254	-0.37	-6.20	10.99	-97.8	-4.5
0.244	-0.35	-6.39	10.88	-99.6	-6.2
0.234	-0.23	-6.70	10.86	-101.3	-5.9
0.224	-0.13	-6.99	10.85	-103.7	-6.1
0.214	-0.03	-7.23	10.80	-105.6	-6.5
0.204	0.05	-7.53	10.67	-108.2	-8.2
0.194	0.23	-7.67	10.64	-110.9	-10.0
0.184	0.36	-7.88	10.61	-113.9	-11.4
0.174	0.48	-7.90	10.46	-117.6	-16.7
0.164	0.73	-7.82	10.12	-119.2	-22.8
0.154	0.65	-7.19	9.20	-119.1	-38.7

Table C.3 Velocity profile data for the multiple turbine rig as presented in Figure 3.10 (Traverse after rotor).

r mm	C_{r3} m/s	C_{t3} m/s	C_{x3} m/s	p_{s3} Pa	p_{t3} Pa
0.351	0.35	-0.38	11.37	-279.1	-203.4
0.346	0.18	-0.85	10.89	-281.5	-211.7
0.341	-0.11	-0.36	10.67	-283.2	-216.6
0.336	0.02	0.22	10.75	-281.5	-214.0
0.331	-0.09	0.07	10.55	-281.6	-216.5
0.326	-0.08	-0.26	10.45	-280.9	-217.2
0.321	0.06	-0.27	10.36	-281.8	-219.0
0.316	0.02	-0.47	10.42	-280.4	-216.9
0.311	-0.12	-0.43	10.61	-282.6	-216.7
0.306	-0.08	-0.30	10.63	-282.5	-216.5
0.301	0.05	-0.16	10.62	-282.3	-216.4
0.296	-0.06	-0.13	10.66	-281.7	-215.3
0.291	-0.18	-0.17	10.70	-279.8	-213.0
0.286	-0.46	-0.26	10.96	-280.1	-209.7
0.276	-0.31	-0.22	11.34	-280.2	-205.0
0.266	-0.46	-0.32	11.31	-279.3	-204.4
0.256	-0.67	-0.34	11.26	-279.3	-204.9
0.246	-0.64	-0.45	11.00	-278.4	-207.4
0.236	-0.62	-0.50	11.14	-278.8	-206.0
0.226	-0.88	-0.56	11.56	-277.7	-199.1
0.216	-0.87	-0.45	11.75	-276.3	-195.1
0.206	-0.78	-0.47	11.61	-274.9	-195.7
0.196	-1.21	-0.56	11.46	-273.9	-196.1
0.186	-1.33	-0.81	11.66	-271.8	-190.9
0.176	-1.30	-0.98	11.85	-267.7	-184.1
0.166	-1.11	-0.38	10.79	-257.7	-188.9
0.156	-0.86	-0.87	8.44	-251.2	-208.8

Appendix

D

Sample Calculations

D.1 Soderberg Model Applied to Experimental Data

In this section the total-to-total turbine efficiency is evaluated by applying the Soderberg model to experimental results from the horizontal axis rig. The velocity data is extracted at the area halving radius $r_{rms} = 274\,\mathrm{mm}$. The axial chord of the blades, b, is measured at the mean area radius. The blade aspect ratio for the IGVs is then $R_{asp,IGV} = l_b/b = 240/85 = 2.82$, where l_b is the blade length. For the rotor it is $R_{asp,r} = 216/30 = 7.20$. The flow deflection in the IGV row is $\epsilon_s = 31.4$ degrees, in the rotor row it is $\epsilon_r = 2.9$ degrees. The loss coefficients of the two blade rows can now be evaluated from Equation 2.29, which is reiterated here for convenience:

$$\zeta = 0.025\left(1+\left(\frac{\epsilon}{90^\circ}\right)^2\right)\left(1+\frac{3.2}{R_{asp}}\right)$$

It gives an IGV loss coefficient of $\zeta_{IGV} = 0.060$ and a rotor loss coefficient of $\zeta_r = 0.036$.

The dimensionless absolute flow speed at the IGV exit is $c_2 = 0.2871$, the dimensionless relative flow speed at the rotor exit is $w_3 = 0.8115$ and the load coefficient is $\Psi = 0.081$. Equation 2.31, which is reiterated here, gives the total-to-total efficiency:

$$\begin{aligned}\eta_{tt,SB} &= \frac{1}{1+\frac{\zeta_{IGV}{c_1}^2+\zeta_a {w_{2a}}^2+\zeta_b {w_3}^2}{2\Psi}} \\ &= 84.8\,\% \end{aligned} \tag{D.1}$$

D.2 Profile Loss Coefficients (Chapter 3)

D.2.1 Rotor of the Multiple Turbine Rig

The input data for the calculation of the rotor profile loss coefficient at the mean area radius can be found in Table D.1.

Table D.1 Input data for the calculation of the rotor profile loss coefficient for the horizontal axis test rig.

Section	2	3
Radius, m	0.274	0.256
Density, kg/m^3	1.17	1.17
Static pressure, Pa	-96.6	-279.2
Relative Velocity, m/s	29.28	33.12

The profile loss coefficients are evaluated along streamlines from Equation 3.6, which is repeated here for convenience:

$$\zeta_p = \frac{p_{t1,rel} - p_{t2,rel}}{\frac{1}{2}\rho W^2}$$

where $p_{t1,rel}$ is the relative total pressure at the inlet of the blade row, $p_{t2,rel}$ is the relative total pressure at the exit of the blade row, ρ is the density and W is the relative flow speed at the exit of the blade row.

The relative total pressure is taken as

$$p_{t,rel} = p_s + \frac{1}{2}\rho W^2 \tag{D.2}$$

i.e. as the sum of the static pressure and the relative dynamic head, with W being the flow speed relative to the particular blade row.
Hence, for the rotor row the relative total pressures at the mean area radius is

$$p_{t1,rel} = -96.6 + 0.5 \times 1.168 \times 29.28^2 = 404.2$$
$$p_{t2,rel} = -279.2 + 0.5 \times 1.168 \times 33.12^2 = 361.4$$

and the profile loss coefficient is

$$\zeta_p = \frac{404.2 - 361.4}{0.5 \times 1.168 \times 33.12^2} = 0.067$$

D.3 PCU Performance Model (Chapter 5)

The input data for the PCU performance model calculation can be found in Table D.2. Figure D.1 shows a schematic drawing of the solar chimney power conversion unit indicating the various stations in the flow passage; the station $in1$ refers to the collector exit, $in3$ to the turbine inlet (after the bellmouth), $ex1$ to the turbine exit, $ex2$ to the exit of the diffuser/nozzle directly after the turbine, $ex3$ to the exit of the mixing section, $ex4$ to the exit of the horizontal-to-vertical transition section and $ex5$ to the exit of the diffuser section in the chimney. The station $in2$ refers to the exit of the horizontal-to-vertical transition section in the case where this section is upstream of the turbine, i.e. for all configurations with vertical axis turbines as shown in the figures 1.1 and 1.2.

Table D.2 Input to the PCU performance model sample calculation.

Chimney diameter	d_c	[m]	160
Number of turbines	Z_t	[-]	32
Diffuser area ratio	R_d	[-]	1.0
IGV aspect ratio	$R_{asp,IGV}$	[-]	4.0
Rotor blade aspect ratio	$R_{asp,r}$	[-]	3.0
Hub-to-tip radius ratio	R_{HT}	[-]	0.4
Inlet total pressure	p_{t0}	[Pa]	89 953
Inlet total temperature	T_{t0}	[K]	336
Exit total pressure	$p_{t,ex5}$	[Pa]	88 891
Mass flow rate	$\dot{m}$	[ton/s]	333.9
Specific gas constant	R	[J/kg]	287
Specific heat at constant pressure	c_p	[J/(kg K)]	1008
Ratio of specific heats	γ	[-]	1.4
Diffuser effectiveness	η_d	[-]	0.7
Drive train efficiency	η_{DT}	[-]	0.91
Hor.-to-vert. transition loss coeff.	ζ_{hv}	[-]	0.05
Mixing loss coefficient	ζ_m	[-]	0.10
Bell mouth loss coefficient	ζ_{BM}	[-]	0.09

D.3.1 Pressure Losses in the PCU Flow Passage

In this section it is shown, how the pressure drops over the various components of the PCU flow passage, excluding the turbine, are evaluated to get the boundary conditions for the turbine model.

The density of the air is assumed to be constant. It is assessed at the inlet of the PCU as $\rho = p_{t0}/(R\,T_{t0}) = 0.922\,\mathrm{kg/m^3}$. The chimney area, $A_c = \pi {D_c}^2/4 = 20\,106\,\mathrm{m^2}$, and the flow velocity at the PCU exit, $C_{ex5} = \dot{m}/(\rho\,A_c) = 18.0\,\mathrm{m/s}$, are

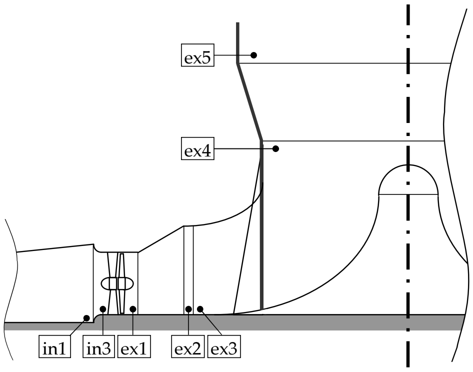

Figure D.1 Schematic drawing of the solar chimney power conversion unit indicating the various stations in the flow passage.

evaluated. The static pressure at the PCU exit is then $p_{ex5} = p_{t,ex5} - 0.5\rho {C_{ex5}}^2$. Note that the swirl is assumed to be negligible. The flow velocity at the exit of the horizontal-to-vertical transition section is then $C_{ex4} = C_{ex5}R_{dc} = 18.0$ m/s. R_{dc} is the chimney diffuser area ratio A_{ex5}/A_{ex4}, which is 1.0 in the present case, as the overall diffuser area ratio R_d is also 1.0. The flow velocity is assumed to remain constant over the horizontal-to-vertical transition section and the mixing section: $C_{ex4} = C_{ex3} = C_{ex2}$. With $R_{dc} = 1.0$ the ideal pressure recovery of the diffuser in the chimney is

$$C_{p,id} = 1 - {R_{dc}}^{-2} = 0 \tag{D.3}$$

From the rearranged Equation 5.4 the coefficient of static pressure recovery becomes

$$C_p = \eta_d C_{p,id} = 0 \tag{D.4}$$

Rearranging Equation 5.2 the static pressure at the inlet of the chimney diffuser is

$$p_{ex4} = p_{ex5} - 0.5C_p\rho {C_{ex4}}^2 = 88\,891\,\text{Pa} \tag{D.5}$$

Adding the dynamic head the total pressure is evaluated as $p_{t,ex4} = p_{ex4} + 0.5\rho {C_{ex4}}^2 = 89\,041$ Pa. To evaluate the total pressure at the inlet of the horizontal-to-vertical transition section the definition of the loss coefficient is rearranged, giving

$$p_{t,ex3} = p_{t,ex4} + \zeta_{hv} 0.5\rho {C_{ex4}}^2 = 89\,048\,\text{Pa} \tag{D.6}$$

Similarly the total pressure at the inlet of the mixing section is found as

$$p_{t,ex2} = p_{t,ex3} + \zeta_m 0.5\rho {C_{ex3}}^2 = 89\,063\,\text{Pa} \tag{D.7}$$

Subtracting the dynamic head the static pressure is evaluated: $p_{ex2} = p_{t,ex2} - 0.5\rho {C_{ex2}}^2 = 88\,914$ Pa. The turbine exit diffuser area ratio $R_d = A_{ex1}/A_{ex2}$ is also 1.0 in the present case. The velocity at the turbine exit is $C_{ex1} =$

$C_{ex2}R_d = 18.0$ m/s. If the turbine exit diffuser area ratio R_d is bigger than 1.0, the ideal pressure recovery coefficient and the coefficient of static pressure recovery are evaluated as in Equations D.3 and D.4 and the static pressure at the turbine exit is then

$$p_{ex1} = p_{ex2} - 0.5 C_p \rho {C_{ex1}}^2 = 88\,914\,\mathrm{Pa} \qquad \text{(D.8)}$$

If it is smaller than or equal to 1, the total pressure is assumed to remain constant, $p_{t,ex1} = p_{t,ex2}$, and to get the static pressure, p_{ex1}, the dynamic head is subtracted.

Assuming that the flow velocity is equal at the inlet and at the exit of the turbine ($C_{in3} = C_{ex1}$) and taking into account the loss over the bell mouth the total pressure at the turbine inlet is

$$p_{t,in3} = p_{t,in1} - \zeta_{BM} \times 0.5 \rho {C_{in3}}^2 = 89\,944\,\mathrm{Pa} \qquad \text{(D.9)}$$

Appendix

E

CFD Sensitivity Analysis

E.1 Grid Sensitivity

To show the grid sensitivity of the CFD solution the results of three grades of grid density are compared for each turbine. To produce the coarser grids every second grid point is skipped in all three dimensions of the grid, which is equivalent to going to another multigrid level in each dimension[1]. The total number of grid points for the various grids are shown in Table E.1. The Spalart-Allmaras turbulence model has been used in this investigation.

Table E.1 Number of grid points for various computational grids

Grid Density	**Number of Grid Points** Multiple Turbine	 Single Turbine
High	1 273 152	961 875
Medium	171 622	130 819
Low	24 765	19 170

Even though the difference in grid density is very large, the results of simulations with these grids show only small variations (Fig. E.1). Particularly the results of the two finer grids are very similar and only differ significantly close to the walls, where the coarser of the two grids induces a slight thickening of the boundary layer. Only these finer grids are able to capture the velocity peaks.

---

[1] For a more detailed explanation on multigrid levels refer to the documentation provided by Numeca.

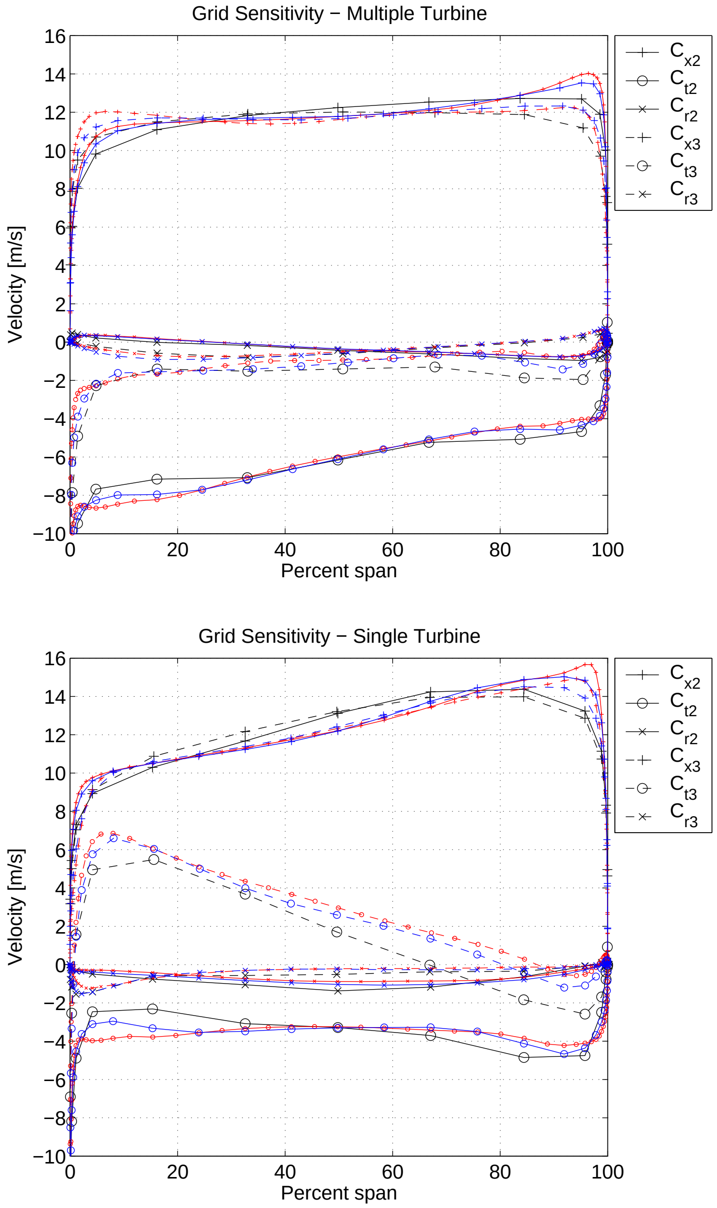

Figure E.1 Velocity components from CFD simulations on the multiple and single turbine model using various grades of grid refinement (black/big markers: coarse grid; blue/smaller markers: finer grid; red/smallest markers: finest grid).

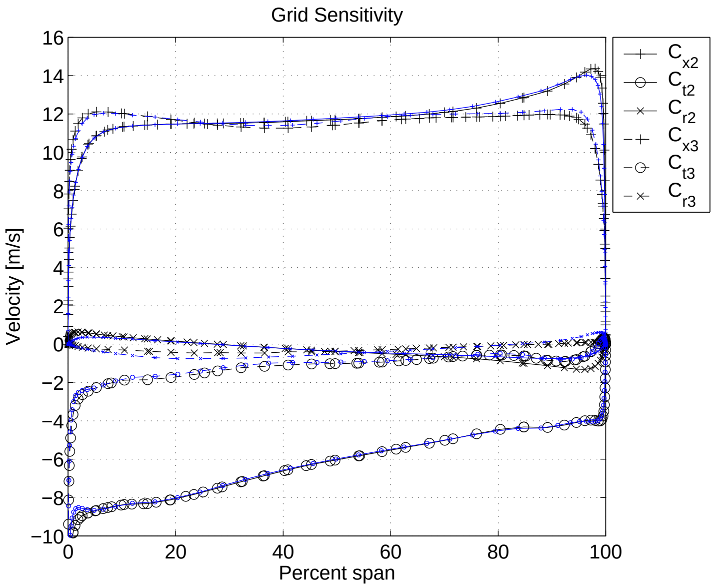

Figure E.2 Velocity components from CFD simulations on the multiple turbine model using different meshing approaches (black/big markers: mesh provided by Hildebrandt (2007); blue/smaller markers: mesh generated by author).

A comparison of the results from the finest grid in the above comparison, which has been provided by Hildebrandt (2007), and a slightly finer grid (1.7 million grid points) generated by the author is presented in Figure E.2; no significant differences are found in the results.

E.2 Sensitivity to Modelling Approaches

The sensitivity of the CFD solution to various modelling approaches is explored here. The investigated cases are listed in Table E.2 and the results are shown in Figure E.3. The laminar case and the case where the transition model of Abu-Ghannam and Shaw was used were run with the perfect gas fluid model to achieve better convergence. Even though the modelling approaches vary significantly the results obtained are very similar. Only close to the walls the laminar solution and the solution from the transition model predict thicker boundary layers than the turbulent models as it would be expected. The solution from the transition model also predicts a significantly lower flow deflection in the IGV row than the other models.

Table E.2 List of modelling approaches.

Case	Fluid Model	Flow Model	Transition Model
1	Air (perfect gas)	laminar	-
2	Air (incompressible)	SA	-
3	Air (incompressible)	kωSST	-
4	Air (perfect gas)	SA	AGS

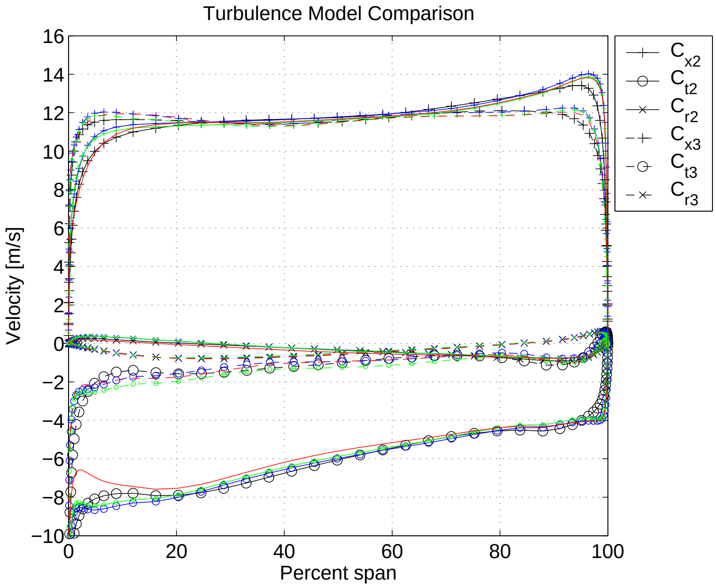

Figure E.3 Velocity components from CFD simulations on the multiple turbine model using various flow modelling approaches (black/big markers: Case 1; blue/smaller markers: Case 2; green/smallest markers: Case 3; red/no markers: Case 4).

Appendix F

CFD Analysis of Horizontal-to-Vertical Transition Section

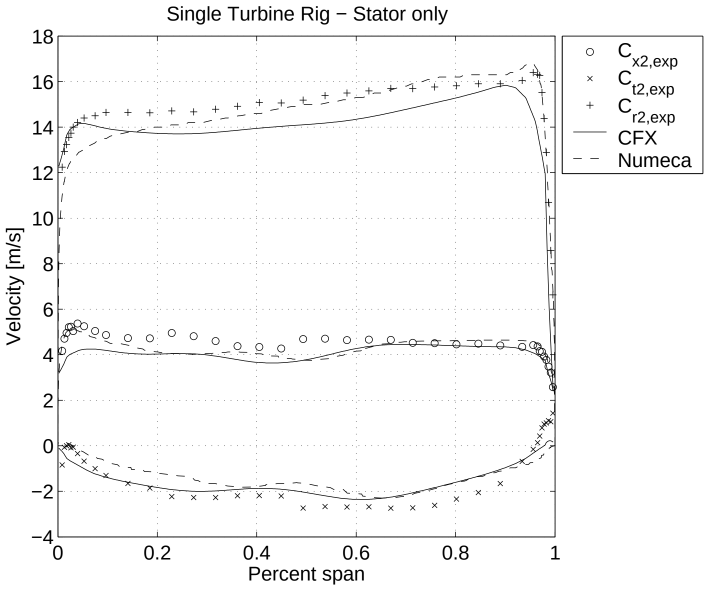

Figure F.1 Velocity components from experiments and CFD simulations on the single turbine model without the rotor (markers: experimental data (Kirstein, 2004); solid line: CFD results (Kirstein, 2004); dashed line: present CFD investigation).

Kirstein (2004) presents an extensive investigation on the horizontal-to-vertical transition section of a single turbine model. He worked with the single turbine rig of Gannon (2002), but removed the rotor. For his CFD investigation he used CFX.

Here his data for one case is compared to a simulation with Numeca FINE/Turbo. The computational domain is similar to the one shown on the left in Figure 4.1, only that the rotor has been removed. The hub is again extended to the end of the domain. In the experiment and in the numerical investigation of Kirstein (2004) the hub ended at the lower probe traverse station shown in Figure 3.2. The Spalart-Allmaras turbulence model has been used in this investigation and the volume flow has been adjusted to match the value from the experimental data.

The velocity profiles of the numerical investigation presented here agree well with the experimental data of Kirstein (2004). Particularly the tangential component is predicted very accurately. The biggest discrepancy is in the radial component, which is probably a result of the hub not being cut off for the simulation.

Appendix G

Operating Conditions for the PCU

Table G.1 Operating conditions for Chapter 6.

Mass flow class	1	2	3	4	5	peak
Mass flow, $\dot{m}$, ton/s	158.31	196.64	235.26	277.27	315.63	333.88
Inlet total pressure, p_{t0}, Pa	89 990	89 984	89 978	89 969	89 958	89 953
Inlet total temperature, T_{t0}, °C	21	31	35	40	54	63
Exit total pressure, p_{t4}, Pa	89 785	89 647	89 497	89 293	89 036	88 891
Hours per year	2 163	2 531	1 171	1 507	1 411	1

Table G.2 PCU operating conditions for the plant with a chimney of 1000 m height and 120 m diameter.

Mass flow class	1	2	3	4	5	peak
Mass flow, $\dot{m}$, ton/s	78.66	93.78	111.16	127.95	144.09	152.42
Inlet total pressure, p_{t0}, Pa	89 996	89 994	89 992	89 989	89 985	89 983
Inlet total temperature, T_{t0}, °C	22	31	34	39	52	59
Exit total pressure, p_{t4}, Pa	89 844	89 769	89 678	89 569	89 426	89 339
Hours per year	2 578	2 361	1 094	1 483	1 267	1

Table G.3 PCU operating conditions for the plant with a chimney of 1000 m height and 150 m diameter.

Mass flow class	**1**	**2**	**3**	**4**	**5**	**peak**
Mass flow, $\dot{m}$, ton/s	105.37	126.60	152.98	178.00	200.99	213.10
Inlet total pressure, p_{t0}, Pa	89 993	89 989	89 984	89 979	89 972	89 968
Inlet total temperature, T_{t0}, °C	21	30	32	36	48	55
Exit total pressure, p_{t4}, Pa	89 869	89 802	89 713	89 608	89 475	89 393
Hours per year	2 775	2 199	1 076	1 436	1 297	1

Table G.4 PCU operating conditions for the plant with a chimney of 1000 m height and 180 m diameter.

Mass flow class	**1**	**2**	**3**	**4**	**5**	**peak**
Mass flow, $\dot{m}$, ton/s	109.93	139.72	174.48	217.24	251.79	271.22
Inlet total pressure, p_{t0}, Pa	89 992	89 987	89 980	89 968	89 956	89 949
Inlet total temperature, T_{t0}, °C	16	25	30	33	44	53
Exit total pressure, p_{t4}, Pa	89 901	89 863	89 782	89 661	89 522	89 427
Hours per year	722	3 521	1 390	1 526	1 624	1

Table G.5 PCU operating conditions for the plant with a chimney of 1000 m height and 210 m diameter.

Mass flow class	**1**	**2**	**3**	**4**	**5**	**peak**
Mass flow, $\dot{m}$, ton/s	122.47	167.03	208.85	257.87	298.67	321.50
Inlet total pressure, p_{t0}, Pa	89 990	89 982	89 971	89 956	89 939	89 928
Inlet total temperature, T_{t0}, °C	18	26	29	32	43	51
Exit total pressure, p_{t4}, Pa	89 894	89 865	89 785	89 670	89 536	89 445
Hours per year	1 439	3 095	1 153	1 490	1 606	1

Table G.6 PCU operating conditions for the plant with a chimney of 1000 m height and 240 m diameter.

Mass flow class	**1**	**2**	**3**	**4**	**5**	**peak**
Mass flow, $\dot{m}$, ton/s	147.22	191.07	241.68	293.16	337.07	361.53
Inlet total pressure, p_{t0}, Pa	89 986	89 976	89 961	89 943	89 922	89 909
Inlet total temperature, T_{t0}, °C	19	27	29	31	42	49
Exit total pressure, p_{t4}, Pa	89 893	89 859	89 775	89 667	89 539	89 453
Hours per year	2 319	2 537	977	1 426	1 524	1

Table G.7 PCU operating conditions for the plant with a chimney of 1500 m height and 160 m diameter.

Mass flow class	**1**	**2**	**3**	**4**	**5**	**peak**
Mass flow, $\dot{m}$, ton/s	162.03	194.05	231.56	267.73	302.08	319.98
Inlet total pressure, p_{t0}, Pa	89 992	89 989	89 984	89 978	89 971	89 967
Inlet total temperature, T_{t0}, °C	22	31	33	38	51	59
Exit total pressure, p_{t4}, Pa	89 778	89 668	89 531	89 366	89 155	89 024
Hours per year	2 627	2 321	1 086	1 479	1 270	1

Table G.8 PCU operating conditions for the plant with a chimney of 1500 m height and 190 m diameter.

Mass flow class	**1**	**2**	**3**	**4**	**5**	**peak**
Mass flow, $\dot{m}$, ton/s	201.02	242.62	294.42	343.70	388.68	412.54
Inlet total pressure, p_{t0}, Pa	89 988	89 982	89 974	89 964	89 952	89 945
Inlet total temperature, T_{t0}, °C	21	30	32	36	48	56
Exit total pressure, p_{t4}, Pa	89 807	89 707	89 571	89 409	89 207	89 081
Hours per year	2 771	2 198	1 075	1 438	1 301	1

Table G.9 PCU operating conditions for the plant with a chimney of 1500 m height and 220 m diameter.

Mass flow class	**1**	**2**	**3**	**4**	**5**	**peak**
Mass flow, $\dot{m}$, ton/s	236.47	287.99	353.74	415.49	471.28	500.87
Inlet total pressure, p_{t0}, Pa	89 983	89 975	89 962	89 947	89 930	89 920
Inlet total temperature, T_{t0}, °C	21	29	31	35	46	54
Exit total pressure, p_{t4}, Pa	89 827	89 732	89 598	89 438	89 242	89 119
Hours per year	2 906	2 118	997	1 441	1 321	1

Table G.10 PCU operating conditions for the plant with a chimney of 1500 m height and 250 m diameter.

Mass flow class	**1**	**2**	**3**	**4**	**5**	**peak**
Mass flow, $\dot{m}$, ton/s	266.44	326.51	405.18	479.12	544.76	579.70
Inlet total pressure, p_{t0}, Pa	89 979	89 968	89 950	89 930	89 907	89 893
Inlet total temperature, T_{t0}, °C	21	29	30	34	45	52
Exit total pressure, p_{t4}, Pa	89 841	89 750	89 617	89 456	89 263	89 141
Hours per year	2 990	2 045	966	1 439	1 343	1

Table G.11 PCU operating conditions for the plant with a chimney of 1500 m height and 280 m diameter.

Mass flow class	**1**	**2**	**3**	**4**	**5**	**peak**
Mass flow, $\dot{m}$, ton/s	256.05	326.75	414.84	515.88	599.48	646.58
Inlet total pressure, p_{t0}, Pa	89 981	89 968	89 948	89 919	89 888	89 868
Inlet total temperature, T_{t0}, °C	17	25	29	32	43	51
Exit total pressure, p_{t4}, Pa	89 873	89 805	89 680	89 501	89 295	89 154
Hours per year	1 305	3 246	1 132	1 476	1 624	1

Table G.12 PCU operating conditions for a smaller plant.

Mass flow class	**1**	**2**	**3**	**4**	**5**	**peak**
Mass flow, $\dot{m}$, ton/s	24.20	30.63	36.52	44.36	51.32	54.48
Inlet total pressure, p_{t0}, Pa	89 998	89 997	89 996	89 994	89 992	89 990
Inlet total temperature, T_{t0}, °C	21	28	32	33	42	48
Exit total pressure, p_{t4}, Pa	89 925	89 903	89 852	89 852	89 794	89 762
Hours per year	2 988	2 215	1 278	1 010	1 292	1

Table G.13 PCU operating conditions for the peak load plant.

Mass flow class	**1**	**2**	**3**	**4**	**5**	**peak**
Mass flow, $\dot{m}$, ton/s	90.26	141.42	209.57	252.08	300.63	331.17
Inlet total pressure, p_{t0}, Pa	89 973	89 931	89 962	89 943	89 917	89 897
Inlet total temperature, T_{t0}, °C	24	38	24	32	43	54
Exit total pressure, p_{t4}, Pa	89 832	89 591	89 763	89 644	89 474	89 352
Hours per year	3 553	1 571	785	1 795	1 079	1

Table G.14 PCU operating conditions for the base load plant.

Mass flow class	**1**	**2**	**3**	**4**	**5**	**peak**
Mass flow, $\dot{m}$, ton/s	128.27	151.97	182.80	209.83	234.42	253.03
Inlet total pressure, p_{t0}, Pa	89 949	89 931	89 949	89 953	89 947	89 942
Inlet total temperature, T_{t0}, °C	27	35	28	31	36	39
Exit total pressure, p_{t4}, Pa	89 678	89 592	89 714	89 715	89 667	89 629
Hours per year	958	1 789	2 580	2 413	1 043	1

Table G.15 PCU operating conditions for the plant with double glazing.

Mass flow class	**1**	**2**	**3**	**4**	**5**	**peak**
Mass flow, $\dot{m}$, ton/s	140.72	175.43	216.91	265.66	306.56	328.27
Inlet total pressure, p_{t0}, Pa	89 987	89 980	89 969	89 953	89 936	89 925
Inlet total temperature, T_{t0}, °C	16	24	30	32	44	53
Exit total pressure, p_{t4}, Pa	89 866	89 835	89 746	89 618	89 470	89 377
Hours per year	592	3 810	1 271	1 476	1 634	1

Table G.16 PCU operating conditions for the plant with double glazing and anti-reflective coating.

Mass flow class	**1**	**2**	**3**	**4**	**5**	**peak**
Mass flow, $\dot{m}$, ton/s	176.62	208.83	249.39	287.70	322.13	340.00
Inlet total pressure, p_{t0}, Pa	89 980	89 971	89 959	89 945	89 929	89 920
Inlet total temperature, T_{t0}, °C	23	30	32	35	47	55
Exit total pressure, p_{t4}, Pa	89 831	89 761	89 660	89 543	89 404	89 322
Hours per year	3 489	1 514	910	1 462	1 408	1

List of References

Alberti, L. (2006). *Flow Around Cylindrical Towers: The Stabilizing Role of Vertical Ribs*. Master's thesis, University of Stellenbosch. (Cited on page 3.)

Beitz, W. and Grote, K.-H. (2001). *Dubbel - Taschenbuch für den Maschinenbau*. 20th edn. Springer-Verlag, Berlin. (Cited on page 65.)

Bernardes, M.A.D.S. (2004). *Technische, ökonomische und ökologische Analyse von Aufwindkraftwerken (Technical, Economical and Ecological Analysis of Solar Chimney Power Plants)*. Ph.D. thesis, Universität Stuttgart. (in German). (Cited on pages 3, 4, 5, 6, 15, 17, 18, 68, 75, 76, 84, 85, and 86.)

Beyers, J., Kröger, D. and Harms, T. (2002). Turbulent convective heat transfer for accelerating radial flows with special emphasis on buoyancy. In: *HEFAT2002, 1st International Conference on Heat Transfer, Fluid Dynamics and Thermodynamics*. (Cited on page 3.)

Bilgen, E. and Rheault, J. (2005). Solar chimney power plants for high latitudes. *Solar Energy*, vol. 79, pp. 449–458. (Cited on page 7.)

Bonnelle, D. (2003). *Vent Artificiel - "Tall is Beautiful"*. Editions du Cosmogone. (Cited on page 4.)

Burton, T., Sharpe, D., Jenkins, N. and Bossanyi, E. (2001). *Wind Energy Handbook*. John Wiley & Sons Ltd. (Cited on pages 10 and 29.)

Bywaters, G., John, V., Lynch, J., Mattila, P., Norton, G., Stowell, J., Salata, M., Labath, O., Chertok, A. and Hablanian, D. (2004). Northern Power Systems WindPACT drive train alternative design study report. Tech. Rep. NREL/SR-500-35524, National Renewable Energy Laboratory, Colorado. Revised October 2004. (Cited on pages 11, 15, 20, and 59.)

Cabanyes, I. (1903). Proyecto de motor solar. *La Energia Electrica*, vol. 8, no. 4. (Cited on page 2.)

Cahill, J. (1997). *Identification and Evaluation of Loss and Deviation Models for use in Transonic Compressor Stage Performance Prediction*. Master's thesis, Virginia Polytechnic Institute and State University. (Cited on page 42.)

Cai, R., Wu, W. and Fang, G. (1990). Basic analysis of counter-rotating turbines. In: *Proceedings of the 35th International Gas Turbine and Aeroengine Congress and Exposition in Brussels, Belgium*. ASME. (Cited on page 20.)

Calder, R. (1970). *Leonardo & the age of the eye*. William Heinemann Ltd., London. P. 106. (Cited on page 2.)

Coetzer, E.F. (2006). Designing and building of a horizontal-axis model turbine for a solar chimney. Undergraduate project, University of Stellenbosch. (Cited on pages 35 and 38.)

Denantes, F. and Bilgen, E. (2006). Counter-rotating turbines for solar chimney power plants. *Renewable Energy*, vol. 31, pp. 1873–1891. (Cited on pages 9, 19, 20, 23, 24, 26, and 27.)

Dixon, S. (1998). *Fluid Mechanics and Thermodynamics of Turbomachinery*. Butterworth-Heinemann. (Cited on page 14.)

Fluri, T.P., Pretorius, J.P., Van Dyk, C., Von Backström, T.W., Kröger, D.G. and Van Zijl, G.P.A.G. (2006). Cost analysis of solar chimney power plants. In: *Proceedings of EuroSun*. ISES, Glasgow. (Cited on pages 5, 6, and 63.)

Fluri, T.P. and Von Backström, T.W. (2007). Comparison of modelling approaches and layouts for solar chimney turbines. *Solar Energy*, , no. available online, doi:10.1016/j.solener.2007.07.006. (Cited on page 19.)

Friedel, H. (2005). *Projektentwicklungsstudie: Kraftwerke in Südafrika auf der Basis regenerativer Energien - Machbarkeit und Aussichten (Project Development Study: Power Stations in South Africa on the Basis of Renewable Energies—Feasibility and Outlook)*. Master's thesis, Bergische Universität Wuppertal, Germany. (in German). (Cited on page 7.)

Gannon, A.J. (2002). *Solar Chimney Turbine Performance*. Ph.D. thesis, University of Stellenbosch. (Cited on pages xiii, 9, 10, 11, 15, 28, 33, 34, 35, 36, 37, 39, 40, 42, 43, 44, 48, 49, 55, 56, 63, 64, and 108.)

Gannon, A.J. and Von Backström, T.W. (2000). Solar chimney cycle analysis with system loss and solar collector performance. *Journal of Solar Energy Engineering*, vol. 122, pp. 133–137. (Cited on pages 3 and 4.)

Gannon, A.J. and Von Backström, T.W. (2002). Solar chimney turbine layout and design method. In: *Proceedings of Solar 2002 in Reno, Nevada*. ASME. (Cited on pages 19, 26, and 46.)

Gannon, A.J. and Von Backström, T.W. (2003). Solar chimney turbine performance. *Journal of Solar Energy Engineering*, vol. 125, pp. 101–106. (Cited on page 33.)

Gasch, R., Twele, J. and Schubert, M. (2002). *Wind Power Plants - Fundamentals, Design, Construction and Operation*. Solarpraxis AG. (Cited on page 15.)

Goldack, A. (2004). *Tragverhalten und Aussteifung hoher Stahlbetonröhren für Aufwindkraftwerke (Structural Behavior and Stiffening of High Reinforced Concrete Tubes for Solar Tower Power Plants)*. Ph.D. thesis, Universität Stuttgart. (in German). (Cited on pages 3 and 57.)

Griffin, D.A. (2001). WindPACT Turbine design scaling studies - Technical area 1: Composite blades for 80- to 120-meter rotor. Tech. Rep. NREL/SR-500-29492, National Renewable Energy Laboratory, Colorado. (Cited on pages 63 and 64.)

Haaf, W., Friedrich, K., Mayr, G. and Schlaich, J. (1983). Solar chimneys; Part I: Principle and construction of the pilot plant in Manzanares. *Int. J. Solar Energy*, vol. 2, pp. 3–20. (Cited on page 4.)

Haaf, W., Mayr, G. and Schlaich, J. (1986). Atmosphärenthermisches Aufwindkraftwerk. Tech. Rep. BMFT FB T 81-113, Schlaich + Partner, Stuttgart. (in German). (Cited on page 5.)

Harris, R.L. (2004). *A Numerical Analysis of the Flow Field Surrounding a Solar Chimney Power Plant*. Master's thesis, University of Stellenbosch. (Cited on page 6.)

Harte, W. (2007). Bergische Universität Wuppertal, Germany. (private communication). (Cited on page 57.)

Hedderwick, R.A. (2001). *Performance Evaluation of a Solar Chimney Power Plant*. Master's thesis, University of Stellenbosch. (Cited on pages 3 and 5.)

Hildebrandt, T. (2007). NUMECA - Ingenieurbüro, Altdorf b. Nürnberg, Germany. (private communication). (Cited on page 106.)

Hill, P. and Peterson, C. (1992). *Mechanics and Thermodynamics of Propulsion*. Addison-Wesley Publishing Company. (Cited on page 21.)

Horlock, J.H. (1966). *Axial Flow Turbines - Fluid Mechanics and Thermodynamics*. Butterworths, London. (Cited on page 26.)

Idelchik, I.E. (1986). *Handbook of Hydraulic Resistance*. Hemisphere Publishing Corporation. (Cited on pages 54, 55, 56, and 58.)

Japikse, D. and Baines, N.C. (1994). *Introduction to Turbomachinery*. Concepts ETI, Inc, Norwich. (Cited on pages 55 and 72.)

Kamper, M. (2004 November). Department of Electrical and Electronic Engineering, University of Stellenbosch. (private communication). (Cited on page 73.)

Kirstein, C.F. (2004). *Flow Through a Solar Chimney Power Plant Collector-to-Chimney Transition Section*. Master's thesis, University of Stellenbosch. (Cited on pages 35, 37, 38, 49, 108, and 109.)

Kirstein, C.F. and Von Backström, T.W. (2006 August). Flow through a solar chimney power plant collector-to-chimney transition section. *Journal of Solar Energy Engineering*, vol. 128, no. 3, pp. 312–317. (Cited on pages 46 and 56.)

Kolb, S. and Helmrich, T. (1996). *Strömungstechnische Auslegung eines Aufwindkraftwerks mit 200 MW Leistung (Aerodynamic Design of a 200 MW Solar Chimney Power Plant)*. Diploma Thesis, Institut für Strömungsmechanik und hydraulische Strömungsmaschinen, Universität Stuttgart. (in German). (Cited on page 54.)

Kröger, D. and Buys, J. (1999). Radial flow boundary layer development analysis. *South African Institution of Mechanical Engineering, R & D Journal*, vol. 15, pp. 95–102. (Cited on page 3.)

Kröger, D.G. and Burger, M. (2004 June). Experimental convection heat transfer coefficient on a horizontal surface exposed to the natural environment. In: *Proceedings of EuroSun2004 - Internationales Sonnenforum*, vol. 1, pp. 422–430. ISES, Freiburg, Germany. (Cited on page 4.)

Kupferschmied, P. (1998). *Zur Methodik zeitaufgelöster Messungen mit Strömungssonden in Verdichtern und Turbinen (On the Methodology of Time-Resolved Measurements with Aerodynamic Probes in Compressors and Turbines)*. Ph.D. thesis, ETH Zürich. Diss. ETH Nr. 12474. (in German). (Cited on page 37.)

Lewis, R.I. (1996). *Turbomachinery Performance Analysis*. Arnold. (Cited on pages 34 and 36.)

Louis, J.F. (1985). Axial flow contra-rotating turbines. In: *Proceedings of the 30th International Gas Turbine Conference and Exhibit in Houston, Texas*. ASME. (Cited on page 20.)

Malcolm, D.J. and Hansen, A.C. (2002). WindPACT Turbine rotor design study. Tech. Rep. NREL/SR-500-32495, National Renewable Energy Laboratory, Colorado. (Cited on pages 64, 65, 66, and 67.)

Mills, D. (2004). Advances in solar thermal electricity technology. *Solar Energy*, vol. 76, pp. 19–31. (Cited on page 7.)

Müller, M. (2002). *Dreidimensionale Simulation der Strömungskontur eines Aufwindkraftwerks (Three Dimensional Simulation of the Flow in a Solar Chimney Power Plant)*. Student Research Project, Institut für Strömungsmechanik und hydraulische Strömungsmaschinen, Universität Stuttgart. (in German). (Cited on pages 54 and 56.)

Ozgur, C. and Nathan, G. (1971). A study of contrarotating turbines based on design efficiency. *Journal of Basic Engineering*, vol. 93, pp. 395–404. (Cited on page 20.)

Pastohr, H. (2004). *Thermodynamische Modellierung eines Aufwindkraftwerks (Thermodynamic Modelling of a Solar Chimney Power Plant)*. Ph.D. thesis, Bauhaus-Universität Weimar, Germany. (in German). (Cited on page 6.)

Pastohr, H., Kornadt, O. and Gürlebeck, K. (2003). Numerical and analytical calculations of the temperature and flow field in the upwind power plant. *International Journal of Energy Research*, vol. 28, pp. 495–510. (Cited on pages 5 and 10.)

Pasumarthi, N. and Sherif, S.A. (1998a). Experimental and theoretical performance of a demonstration solar chimney model - Part I: Mathematical model development. *International Journal of Energy Research*, vol. 22, pp. 277–288. (Cited on page 4.)

Pasumarthi, N. and Sherif, S.A. (1998b). Experimental and theoretical performance of a demonstration solar chimney model - Part II: Experimental and theoretical results and economic analysis. *International Journal of Energy Research*, vol. 22, pp. 443–461. (Cited on page 4.)

Poore, R. and Lettenmaier, T. (2003). WindPACT Advanced wind turbine drive train designs study. Tech. Rep. NREL/SR-500-33196, National Renewable Energy Laboratory, Colorado. (Cited on pages 15, 20, 59, 65, and 66.)

Praisner, T. and Clark, J. (2007). Predicting transition in turbomachinery—Part I: A review and new model development. *Journal of Turbomachinery*, vol. 129, pp. 1–13. (Cited on pages 45 and 51.)

Praisner, T., Grover, E., Rice, M. and Clark, J. (2007). Predicting transition in turbomachinery—Part II: Model validation and benchmarking. *Journal of Turbomachinery*, vol. 129, pp. 14–22. (Cited on page 45.)

Pretorius, J.P. (2006). *Optimization and Control of a Large-scale Solar Chimney Power Plant*. Ph.D. thesis, University of Stellenbosch. (Cited on pages 1, 5, 6, 56, 74, 75, 77, 78, 80, 81, 83, 85, and 91.)

Pretorius, J.P. and Kröger, D.G. (2005). Thermal-flow analysis of a solar chimney power plant. In: *4^{th} International Conference on Heat Transfer, Fluid Mechanics and Thermodynamics*. Cairo. (Cited on page 13.)

Pretorius, J.P. and Kröger, D.G. (2006a). Critical evaluation of solar chimney power plant performance. *Solar Energy*, vol. 80, pp. 535–544. (Cited on pages 3, 4, 5, and 57.)

Pretorius, J.P. and Kröger, D.G. (2006b). Solar chimney power plant performance. *Journal of Solar Energy Engineering*, vol. 128, no. 3, pp. 302–311. (Cited on pages 5, 14, and 60.)

Pretorius, J.P., Kröger, D.G., Buys, J.D. and Von Backström, T.W. (2004). Solar tower power plant performance characteristics. In: *EuroSun2004 - Internationales Sonnenforum, Proceedings*, vol. 1, pp. 870–879. International Solar Energy Society. (Cited on page 5.)

Pullan, G. (2006). Secondary flows and loss caused by blade row interaction in a turbine stage. *Journal of Turbomachinery*, vol. 128, pp. 484–491. (Cited on pages 45 and 51.)

Ridley, N. (1956 May). Improvements in or relating to apparatus for generating power from solar heat. Patent Nr. GB748700. (Cited on page 2.)

Riggs, J.L., Bedworth, D.D. and Randhawa, S.U. (1996). *Engineering Economics*. 4th edn. McGraw-Hill. (Cited on page 17.)

Rosic, B., Denton, J. and Pullan, G. (2006). The importance of shroud leakage modeling in multistage turbine flow calculations. *Journal of Turbomachinery*, vol. 128, pp. 699–707. (Cited on page 45.)

Rousseau, J.-P. (2005). *Dynamic Evaluation of the Solar Chimney*. Master's thesis, University of Stellenbosch. (Cited on page 3.)

Schlaich, J. (1995). *The Solar Chimney - Electricity from the Sun*. Edition Axel Menges. (Cited on pages 2, 3, 7, 8, 16, 18, 67, and 75.)

Schlaich, J., Schiel, W., Friedrich, K., Schwarz, G., Wehowsky, P., Meinecke, W. and Kiera, M. (1995). The solar chimney - Transferability of results from the Manzanares solar chimney plant to larger scale-plants. Tech. Rep., Schlaich Bergermann und Partner, Civil Engineers, Stuttgart, Germany. (Cited on pages 5 and 33.)

Schwarz, G. and Knauss, H. (1981). Strömungstechnische Auslegung des Aufwindkraftwerks Manzanares (Aerodynamic design of the solar chimney power plant in Manzanares). Tech. Rep., Institut für Aerodynamik, Unversität Stuttgart. (in German). (Cited on pages 9, 19, and 20.)

Sezer-Uzol, N. and Long, L. (2006). 3-D time-accurate CFD simulations of wind turbine rotor flow fields. *AIAA*. (Cited on page 45.)

Sims, R., Rogner, H.-H. and Gregory, K. (2003). Carbon emission and mitigation cost comparisons between fossil fuel, nuclear and renewable energy resources for electricity generation. *Energy Policy*, vol. 31, pp. 1315–1326. (Cited on page 18.)

Smith, K. (2001). WindPACT Turbine design scaling studies - Technical area 2: Turbine, rotor, and blade logistics. Tech. Rep. NREL/SR-500-29439, National Renewable Energy Laboratory, Colorado. (Cited on page 64.)

Spera, D.A., Ancona, D.F. and Aspliden, C. (1994). *Wind Turbine Technology*. ASME, New York. (Cited on page 9.)

Stodola, A. (1945). *Steam and Gas Turbines*. P. Smith. (Cited on pages 14 and 15.)

Thakker, A. and Hourigan, F. (2005). Computational fluid dynamics analysis of a 0.6 m, 0.6 hub-to-tip ratio impulse turbine with fixed guide vanes. *Renewable Energy*, vol. 30. (Cited on page 45.)

Thiart, G. (2002 April 8-10). Preliminary CFD analysis of a solar chimney. In: *HEFAT2002, 1st International Conference on Heat Transfer, Fluid Mechanics and Thermodynamics*, pp. 449–452. Kruger Park, South Africa. (Cited on page 6.)

Trieb, F., Langniss, O. and Klaiss, H. (1997). Solar electricity generation, a comparative view of technologies, costs and environmental impact. *Journal for Solar Energy Engineering*, vol. 59, no. 1-3, pp. 89–99. (Cited on page 7.)

Van Dyk, C. (2004*a*). *The Realisation of the Solar Chimney Inlet Guide Vanes*. Master's thesis, University of Stellenbosch. (Cited on pages 3 and 57.)

Van Dyk, C. (2006 9-13 July). A technology development methodology developed for application on the solar chimney structure. In: *PICMET 2006 Proceedings*, pp. 1694–1702. Istanbul, Turkey. (Cited on page 7.)

Van Dyk, C. (2008 due in April). *A Radical Innovation Methodology for Development of the Solar Chimney Structure*. Ph.D. thesis, University of Stellenbosch. (Cited on page 1.)

Van Dyk, M. (2004*b*). Solar chimney Northern Cape - Environmental feasibility report. Undergraduate project, University of Stellenbosch. (Cited on page 6.)

Von Backström, T.W. and Fluri, T.P. (2006). Maximum fluid power condition in solar chimney power plants—an analytical approach. *Solar Energy Journal*, vol. 80, pp. 1417–1423. (Cited on page 5.)

Von Backström, T.W. and Gannon, A.J. (2004). Solar chimney turbine characteristics. *Solar Energy*, vol. 76, pp. 235–241. (Cited on pages 15, 19, 20, 24, 26, 28, and 60.)

Voutilainen, V. (2004 November). Private communication with ABB Finland. (Cited on page 65.)

Weinrebe, G. (2006 September). Schlaich, Bergermann und Partner GmbH. (private communication). (Cited on page 5.)

Westdyk, D. (2007). *Evapotranspiration Effects on Air Flowing over Grass in a Small Glass Roofed Tunnel*. Master's thesis, University of Stellenbosch. (Cited on page 6.)

Wilson, D.G. and Korakianitis, T. (1998). *The Design of High-Efficiency Turbomachinery and Gas Turbines*. 3^{rd} edn. Prentice Hall, London. (Cited on pages 8, 24, and 27.)

Wittwer, V. (2007 March). Fraunhofer-Institut für Solare Energiesysteme, Freiburg, Germany. (private communication). (Cited on page 85.)